Λ(1405) photoproduction with the BGO-OD experiment

Dissertation
zur
Erlangung des Doktorgrades (Dr. rer. nat.)
der
Mathematisch-Naturwissenschaftlichen Fakultät
der
Rheinischen Friedrich-Wilhelms-Universität Bonn

von
Georg Scheluchin
aus
Omsk (Russland)

Bonn, August 2019

Abstract

The $\Lambda(1405)$ has been considered for many years a candidate for an unconventional hadronic state. Being difficult to understand within the framework of a three valence quark, constituent quark model, models explicitly including meson-baryon interactions have had improved success in describing the $\Lambda(1405)$. Current understandings assume a molecule of $N\text{-}\bar{K}$, which consequently has influence on the mass distribution, called the line shape. Measurements of this and the differential production cross section over a broad momentum range are crucial constraints to determine the nature of the $\Lambda(1405)$. In this thesis the $\Lambda(1405)$ is studied with the BGO-OD experiment at the Electron Stretcher Accelerator (ELSA) in Bonn via meson photoproduction. BGO-OD is a unique setup combining a central calorimeter with a forward spectrometer. The production mechanism of a molecule like structure could favor extreme forward angles, where the transferred momentum is minimal. This kinematic regime is particularly well covered by BGO-OD.

Cross section measurements require an understanding of the detector geometry and response, and an absolute flux normalization, both of which were improved as part of this thesis work. Simulations of the data acquisition triggering system were accurately determined, and consistency checks measuring the $\gamma p \to \pi^0 p$ reaction showed good agreement in the cross section compared to other experimental data, demonstrating that the current hardware trigger system is well understood. Furthermore, the reactions γp to $\pi^0 p$, ηp, ωp, $\eta' p$ and $K^+ \Sigma^0$ were identified, to check the performance of the kinematic fitting algorithm implemented in this thesis. The results agree well with previous data.

The achieved results on $\Lambda(1405) \to \pi^0 \Sigma^0$ line shape and differential cross section are statistically comparable to the previous experimental data. In addition, first preliminary results were achieved with the forward spectrometer for production angles not accessible by other experiments.

Contents

Introduction

The pursuit of physics has been driven by seeking to understand how the matter around us is composed of fundamental constituents. That is, is matter made up of basic building blocks? Since ancient times it was speculated that a material can be divided into some smallest parts, which were called atoms. At the beginning of the 20th century, atoms were still considered as elementary particles. Our knowledge of fundamental particles has since dramatically improved, driven by technological advancement.

A standard optical microscope can only resolve structures bigger than the wavelength of light. The diameter of the atom is 0.05 nm to 0.10 nm, which is only a fraction of the wavelength of visible light between 400 nm to 800 nm, and hence can not be resolved with optical microscopy. A significant increase of resolution is possible by making use of the quantum mechanical wave nature of particle beams. According to the De-Broglie relation, the wavelength, λ, is given by $\lambda = \frac{h}{p}$, where h is the Planck constant and p the momentum, and with increasing energy smaller structures can be resolved. Using this technique and variants of it, today single atoms can be made visible. Already at the end of the 19th century, experiments with Geissler tubes showed neutral atoms to have a substructure, because negatively charged electrons can be released. At that time the atom was considered a homogeneously distributed positive charge, containing the much smaller negatively charged electron, to make the atom neutral in whole. This was later revised through Rutherford's scattering experiments with α radiation particles scattering off gold foil. He concluded that the atom must have a compact core, called the nucleus, of about 1 fm in diameter where the positive charge is concentrated.

Figure 1.1: Hydrogen optical spectrum of the atom. The light was diffracted with a prism depending on frequency, which is shown in the upper figure. The intensity of the light is plotted against photon energy in the graph below.

While increasingly higher energies are required to investigate the substructure of a compact bound system, lower energies can be used to investigate the internal interaction dynamics. For the atom, such spectroscopy measurements were performed with visible light, even before the electron was discovered. Electrons are bound within the atom by the electromagnetic force, where only discrete energy levels are allowed. A change in energy can only occur if the atom emits or absorbs the exact energy level difference. The energy exchanged in such cases is carried by the photon. In figure 1.1 the visible light spectrum from the hydrogen atom is illustrated. The attempt to understand the atomic
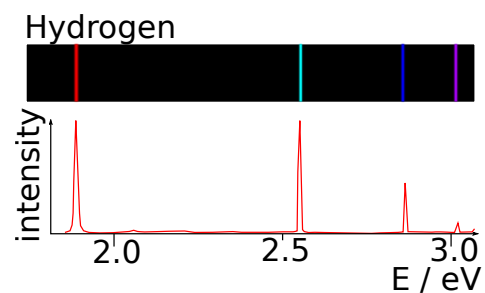
spectrum led to the development of quantum mechanics, which is a cornerstone of physics and also for modern electronics and material science.

With the increase of energy in scattering experiments, it soon became clear that the nucleus is also a composite object. The positively charged nucleon was called the proton and the neutrally charged the neutron. Within the nucleus these nucleons are bound by the nuclear force, which is a residual of the strong force and is comparable to the binding of neutral atoms due to the van der Waals force. Later, high-energy scattering experiments revealed that the nucleon consists of three valence quarks together with gluons and sea quarks. Particles composed of quarks are referred to as hadrons. They are further classified into baryons with three, and mesons with two valence quarks. Sea quarks are virtual quark-antiquark pairs which are created and annihilated constantly in the hadron.
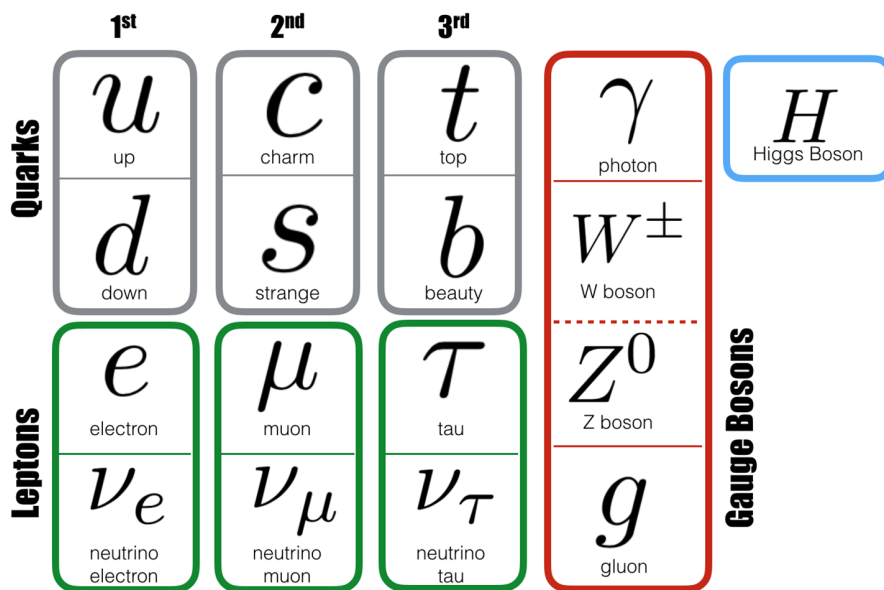
Figure 1.2: Elementary particles of the Standard Model (Figure taken from ref. [1]). They are the known fundamental building blocks of matter.

The discovered elementary particles are summarized in the Standard Model of particle physics, shown in figure 1.2. Elementary particles have no known substructure and in scattering experiments behave as point-like particles. The elementary particles gain their mass from the Higgs field. The Higgs field however is responsible for only a few percent of the mass of the nucleon. It is the gluonic field that generates the vast majority of the nucleon mass.

Based on flavor symmetry, mesons and baryons can be arranged in multiplets. In the sector of the light u(up), d(down) and s(strange)-quarks octets [2], decuplets and singlets shown in figure 1.3 are obtained using the eightfold way organization. Mesons are a type of hadron consisting of a quark and anti-quark, and can also be categorized with the eightfold way. The nonets for pseudoscalar mesons with $J^P = 0^-$ are shown in figure 1.4. In the case of baryons the octet is formed   for $J^P = \frac{1}{2}^+$ and the decuplet for $J^P = \frac{3}{2}^+$, J stands for total angular momentum and P for parity. Note that in the decuplet Σ^* refers to $\Sigma(1385)$ and Ξ^* to $\Xi(1530)$, different from the ground state Σ and Ξ in the octet. The discovery of Δ^{++} was first believed to violate the Pauli principle, which prohibits two or more identical fermions to occupy the same quantum state simultaneously within a quantum system. The
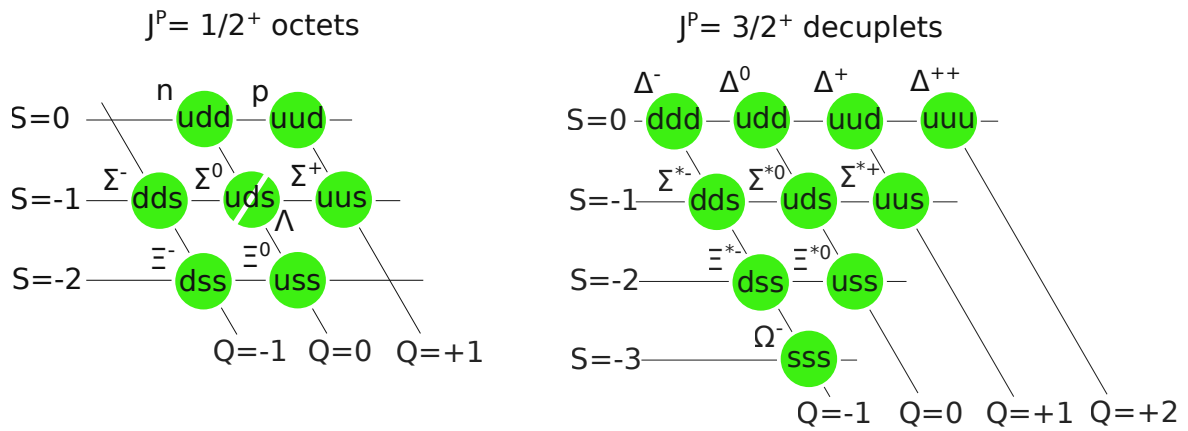
Figure 1.3: Octet and decuplet of the ground state baryons. The quark components of the baryons are listed in the circles, while the name of the particle is next to it. Symbol S shows strangeness and Q the charge of the particle. In the center of the octet the Λ and Σ^0 occupy the same place. [3]

Figure 1.4: Octet plus singlet of the pseudoscalar (0^-) and vector (1^-) meson. The quark components of the mesons are listed in the circles, while the name of the particle is next to it. Symbol S shows strangeness and Q the charge of the particle.[3]
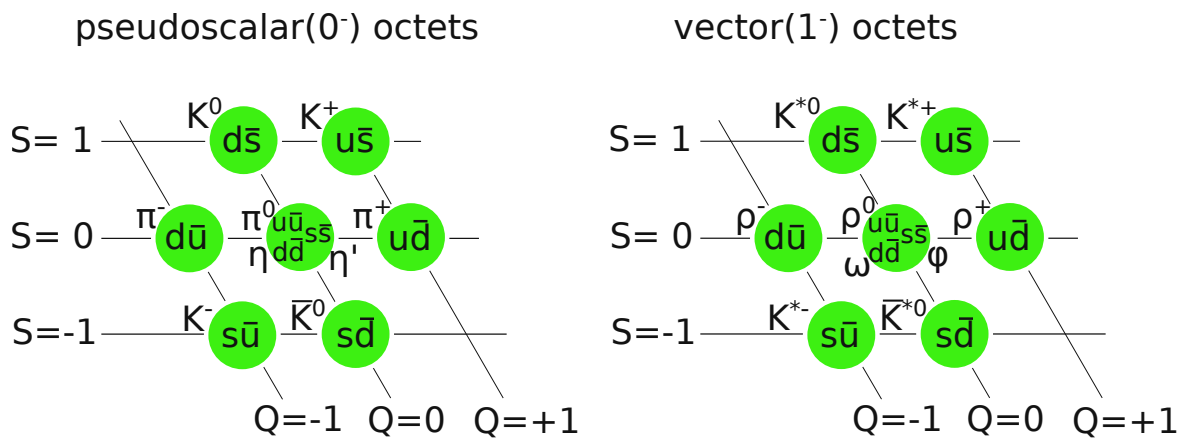
solution for this conundrum was the introduction of the color charge. This new quantum property uses the color mixing analogy. A quark can have a red, green or blue color charge, while the anti-quarks have the complementary colors. A hadron is always color neutral, which is achieved by adding the three color charges together in baryons, or color and anti-color in mesons.
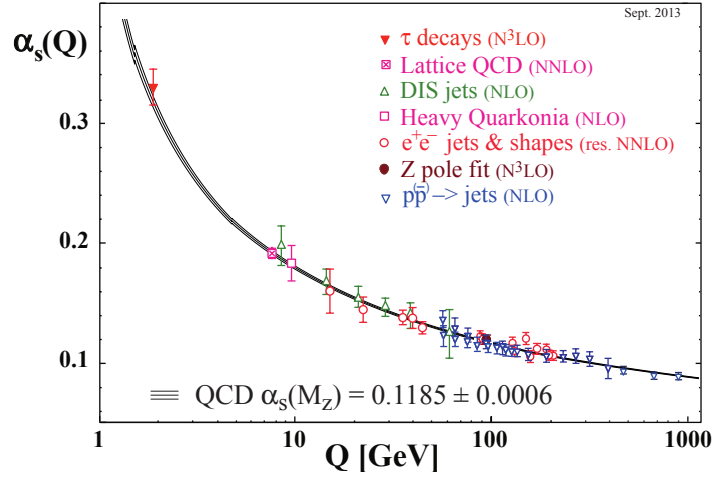

Figure 1.5: Summary of measurements of α_s as a function of the energy scale Q. Different experiment results are plotted in color described in the figure[3].

It is the color charge and the resulting strong color force which binds quarks or quarks and anti-quarks into hadrons. The relative strength of the strong force is given by the strong coupling constant, α_s. Despite the name, α_s was experimentally found to depend on energy as seen in figure 1.5. The energy scale, Q, can be interpreted as the inverse distance with the known relation $\hbar c \approx 200$ MeV fm, which in natural units has the value 1. This means the strong force coupling increases with distances, resulting in a constant force between the quarks over distance. This leads to the interpretation of quarks being "glued" together by the gluons. Increasing the distance between quarks introduces more energy in the gluon field. At a critical distance enough energy is deposited in the gluon field to create a quark anti-quark pair, which results in the creation of hadrons carrying the excess energy-momentum, a process called hadronization. This prevents the investigation of a single free quark and all studies of quarks must be performed in their bound state. This feature is called confinement. A certain exception is the top quark which, due to its very heavy mass, undergoes weak decays prior to hadron formation is possible.

Due to confinement it is impossible to isolate quarks and investigate quarks separately. It is however possible to excite the hadron and use spectroscopy to study internal dynamics. Similar to the atom, hadrons also have resonating energy levels. Due to the high excitation energies, resonances decay most of the time via meson emission, which in return is used to identify the resonance. The process is called meson production. If the excitation is performed with high energetic photons it is then called photoproduction. The extremely short life time of the states correlates with a broad natural line width. This leads to an overlap of states in energy as illustrated in figure 1.6. In this figure, the cross section of the $\gamma p \rightarrow X \rightarrow \pi^0 p$ reaction is plotted against photon energy E. The X state includes all resonances which decay via the π^0 meson emission. The overlap in energy requires sophisticated partial wave analysis, a technique for solving problems with boundary conditions by decomposing each wave into its constituent angular momentum components. In figure 1.6, results with associated Breit-Wigner
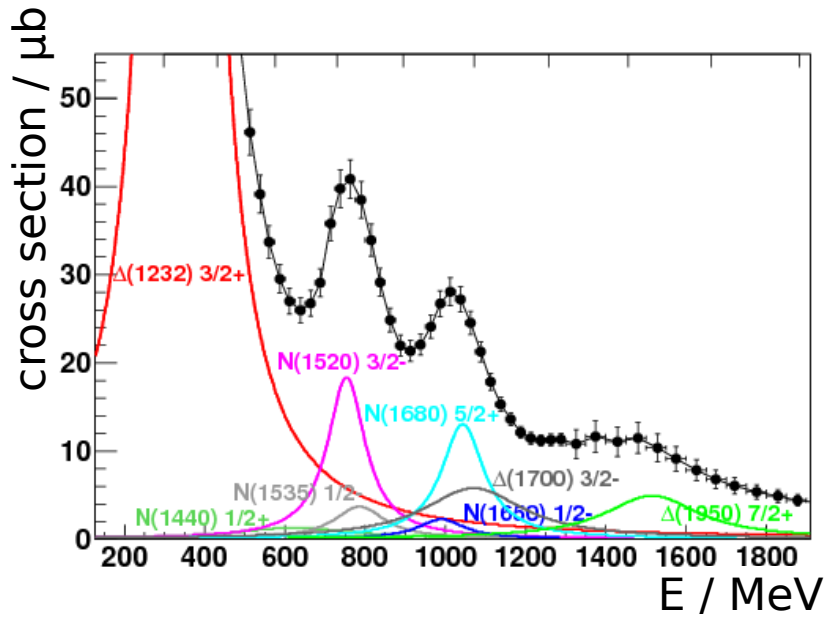
Figure 1.6: Total cross section of π^0 photoproduction off protons against photon energy E [4]. Black points show the experimental results of the Crystal Barrel experiment. Colored lines show the contribution of individual hadron resonances. Both the N and Δ resonance consists of up and down type quarks, but the N state have isospin $1/2$ while the Δ state have $3/2$. The mass of the state is written in brackets followed by the total angular momentum with parity.

resonances are shown using partial wave analysis, which was only possible by also measuring the angular distribution of the decay particles.

Investigations of hadron excitations is a worldwide endeavor since the quark model emerged. For baryon spectroscopy, photoproduction experiments are pursued since over two decades at several major facilities, e.g. the CLAS experiment at JLab[1], the Crystal Ball at MAMI[2], Crystal Barrel/TAPS at ELSA and LEPS[3] at SPring-8[4].
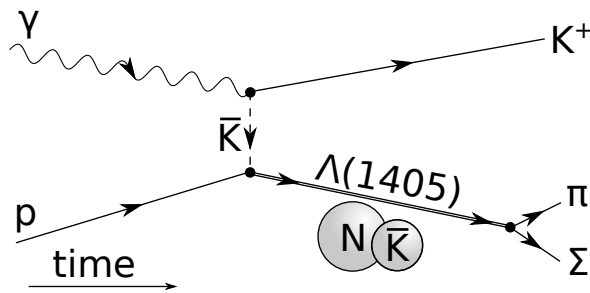
Figure 1.7: Possible photoproduction scheme of the $\Lambda(1405)$ baryonic state. Time propagates from left to right.

The current quark model only includes states with two or three valence quarks. Exotic states with more than three quarks, or no valence quarks, so called glueballs, are still not confirmed. However there is growing evidence. While there were some candidates for such states since 1950, the recent discoveries of the X(3872) state, a candidate for tetraquark or di-meson molecule, with the Belle experiment [5], and the P_c(4380/4450) states, with a possible pentaquark configuration, at LHCb [6] in the (hidden) charm sector have fueled the discussion. The charm quark has a mass of 1.275 GeV and is considered as a heavy quark. The mass of heavy quark bound systems is dominated by their valence quark mass. This allows the use of approximations to calculate the charmonium $c\bar{c}$ bound states, comparable to the positronium $e^- e^+$ states. The predicted states agreed well to the experimentally found states until the discovery of X(3872). One possible explanation for the discrepancy is that X(3872) in reality is a bound object of two D mesons and therefore is not described in the charmonium model. In the much lighter quark sector, with up, down and strange quarks, similar configurations may be found. A candidate for more then 50 years is the Λ(1405) due to the distorted invariant mass distribution, called the line shape, deviating from a Breit-Wigner. The state is created just below the free $\bar{K}N$ production threshold hinting on a possible nucleon-antikaon molecule configuration. This idea is supported by recent Lattice QCD calculations [7]. Photoproduction is ideally suited to investigate such states, as illustrated in figure 1.7. To increase the probability of the creation of a bound state, the momentum transfer to the system should be minimized. This implies very forward-going kaons, while the Λ(1405) decays almost at rest isotropically. The BGO-OD [5] experiment at the ELSA [6] facility is ideally suited for this. It combines a central calorimeter with almost 4π acceptance and a spectrometer for forward-going charged particles. This thesis focuses on the $\gamma p \rightarrow K^+\Lambda$(1405) photoproduction with the BGO-OD experiment. This includes the optimization of the experiment and analysis for determination of absolute cross sections, and the measurement of benchmark channels.

The thesis is structured as follows. The BGO-OD experiment is described in section 2. This includes the hardware setup and the analysis framework. Section 3 discusses the additionally used analysis tools in this thesis, including the kinematic fit which was implemented during this thesis. Section 4 explains how a absolute cross section is determined. The determination of the photon flux in section 4.2 was an important task during this thesis. Section 5 uses well known meson photoproduction reactions to test the performance of the cross section determination at the BGO-OD experiment. At the end in section 6 the focus will shift to Λ(1405), line shape and photoproduction cross section in particular. In section 7 a summary of the results is provided.

---

[5] Name of the experiment. A combination of the used scintillating crystal made of **b**ismuth **g**ermanium **o**xide in the calorimeter and an **o**pen-**d**ipole magnet in the forward spectrometer.

[6] The **El**ectron **S**tretcher **A**ccelerator in Bonn (Germany)

Experiment

Meson photoproduction requires high-energy photons. While only energies in the order of eV are needed to excite an atom, energies in the region of GeV are necessary for nucleon excitation. The Electron Stretcher Accelerator (ELSA) is used to produce photons of such a magnitude. It accelerates electrons to energies of up to 3.2 GeV. The accelerator is described in detail in section 2.1. The electron beam then enters the BGO-OD experimental area where it hits a thin radiator and a real photon beam with a continuous energy spectrum is produced via bremsstrahlung. After that the bremsstrahlung photons hit a target, typically filled with liquid hydrogen, acting as a target of free protons. The decay particles of reactions are then detected with the BGO-OD detector setup, which is situated around the target cell. BGO-OD is described in section 2.2. Detector signals are processed with the analysis framework explained in section 2.3

2.1 Electron Stretcher Accelerator (ELSA)

The Electron Stretcher Accelerator (ELSA)[8] is located beneath the Physikalisches Institut building at the University of Bonn. The facility can be seen in figure 2.1. In the first stage, a thermal gun releases electrons bound in the cathode material. A potential difference then removes and accelerates the electrons away from the cathode. The linear accelerator (LINAC) accelerates these electrons to an energy of approximately 20 MeV before they are inserted into the booster synchrotron. After an acceleration to at least 0.5 GeV, the electrons are guided into the stretcher ring where they can be accelerated up to 3.2 GeV.

The stretcher ring is filled in bunches by the booster synchrotron. Accelerating the electrons to a higher energy begins once the stretcher ring is completely filled. As soon the electrons reach the required energy, a small part of the beam is extracted and is directed to either the Crystal Barrel[9] or the BGO-OD experiment as a quasi-continuous beam. This process continues until the stretcher ring is completely depleted. The filling of the stretcher ring by the booster synchrotron then starts anew.

It is possible to accelerate longitudinally polarized electrons to produce a circular polarized photon beam. In this case the electrons are polarized vertically so that they do not lose their polarization during the acceleration in the circular accelerator. Just before the experimental areas, the spin direction is turned by 90° into the horizontal plane. The source for longitudinally polarized electrons was not operational during this thesis[10].
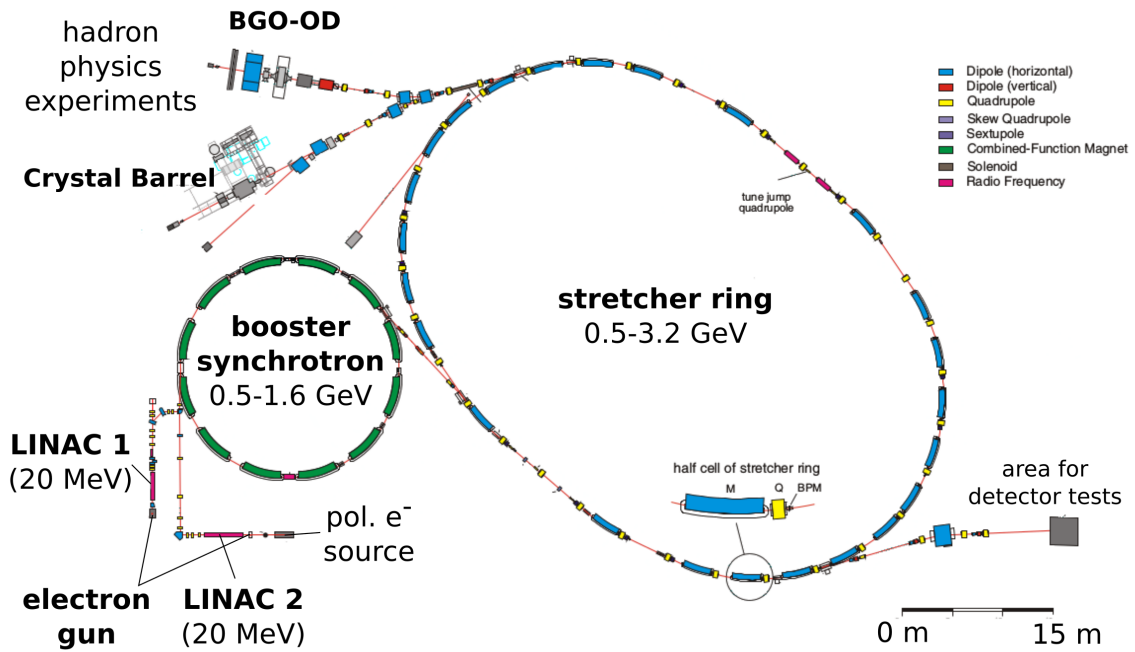
Figure 2.1: Overview of the Electron Stretcher Accelerator [8] in Bonn, showing the main components of the accelerator and the experimental areas.
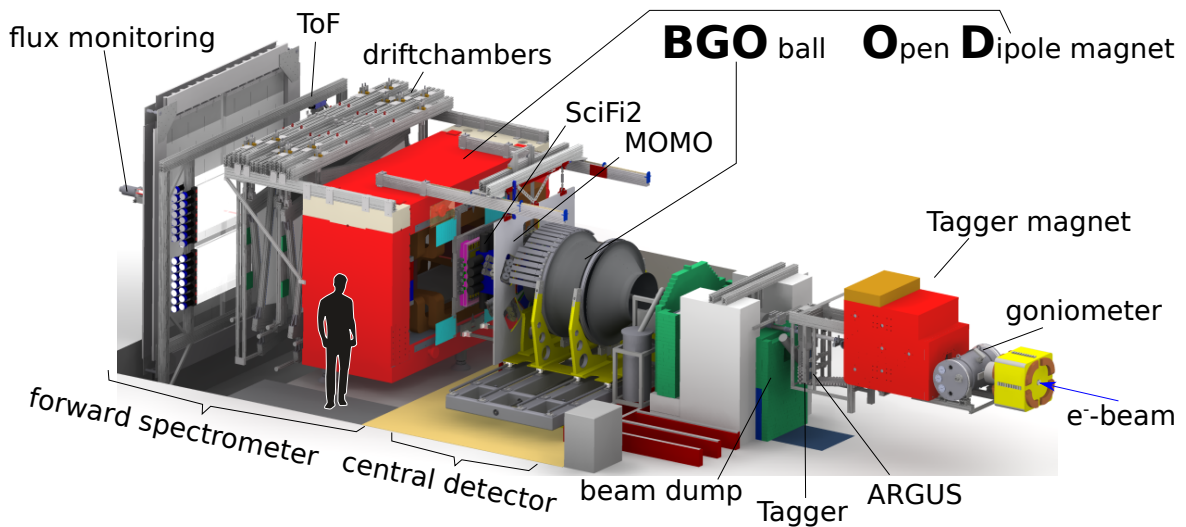

Figure 2.2: Overview of the BGO-OD experiment [11]. The electron beam is provided by the ELSA accelerator and is indicated by an arrow. The central detectors are shown in more detail in figure 2.6 and the forward spectrometer in figure 2.7.

2.2 The BGO-OD experiment

The BGO-OD experiment, located at the ELSA facility, was constructed by an international collaboration and is ideally suited to pursue meson photoproduction. An overview of the experiment is depicted in figure 2.2. The electron beam, which is provided by the ELSA accelerator, hits a radiator inside the goniometer tank. A real photon beam is then produced via bremsstrahlung (section 2.2.1). These photons impinge on a target (section 2.2.2) in the center of the experiment, which may lead to hadronic interactions. The decay particles of such reactions can then be detected by the BGO-ball (section 2.2.3) surrounding the target cell or at forward angles by the forward spectrometer (section 2.2.5). The acceptance between the central and forward detectors is covered by the intermediate detectors (section 2.2.4). At the very end of the experiment the photon flux is monitored (section 2.2.6).

Figure 2.3 illustrates the coordinate system used in this thesis. A particle moving in the beam direction goes in the forward direction and will have a polar angle, θ, of 0° degree. Particles moving opposite the beam direction will have a polar angle, θ, of 180°. By looking in the beam direction parallel to the ground floor, particles which are left to the beam have a ϕ angle of 0° and right to the beam 180°. In beam direction perpendicular to the floor, particles above the beam have $\phi = 90°$ and below the beam line $\phi = 270°$. Angles are sometimes shown in the center of mass frame as θ_{CMS} or ϕ_{CMS}. Without any additional suffix θ and ϕ refer to the laboratory frame.
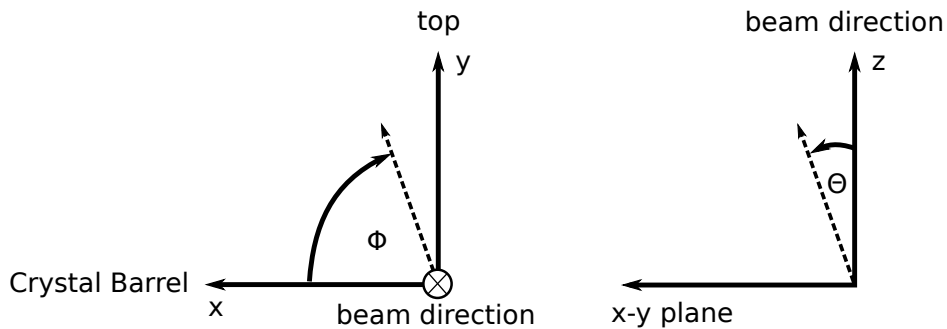
Figure 2.3: Illustration of the coordinate system in the BGO-OD experiment. Dashed line shows an example vector in this system and the definition of the θ and ϕ angles. The Crystal Barrel experiment orientation to the BGO-OD experiment is seen in figure 2.1.

2.2.1 Photon tagging system (Tagger)

Figure 2.4 shows an overview of the tagging system. The bremsstrahlung process takes place inside the goniometer tank. The goniometer can precisely rotate a wheel with different radiators and align each to the electron beam. To produce unpolarized photons, three different copper radiators of varying thicknesses are available: $50\,\mu$m, $150\,\mu$m or $200\,\mu$m. For producing linearly polarized photons, a diamond radiator of thickness $500\,\mu$m is used [12]. The crystalline structure allows the bremsstrahlung process to distribute the recoil momentum over the full crystal lattice. This enhances the production on a plane resulting in a linear polarized beam and is known as coherent bremsstrahlung. The incoherent bremsstrahlung process, where the recoil momentum is transferred to only one atom still takes place. The resulting bremsstrahlung spectrum is then a mixture of the incoherent $1/E_\gamma$ distribution and a peak structure from the coherent process. For circularly polarized photons, a longitudinally polarized electron beam is required. Through helicity transfer the bremsstrahlung photons will be circularly

Figure 2.4: Side view of the photon tagging system (Tagger). The electron beam from ELSA e_0^- moves from the left to right. After the bremsstrahlung process the pho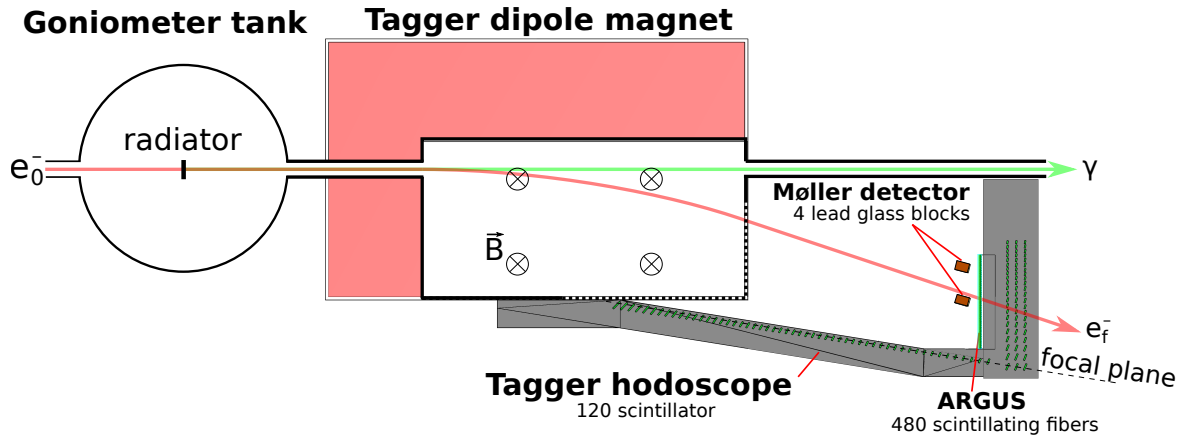tons γ move in straight line, while the electrons e_f^- are deflected by the perpendicular magnetic field $\vec{B}$. The green rectangles inside the gray area represent each individual scintillator of the Tagger hodoscope.

polarized.

The bremsstrahlung photon produced on the radiator and the associated post-bremsstrahlung electron then will enter the Tagger magnet. The magnet creates a magnetic dipole field with around 1 T. Here the electrons are deflected due to the Lorentz force, which depends on their momentum. Electrons that did not undergo bremsstrahlung are directed into the beam dump, where they are stopped. Post-bremsstrahlung electrons are deflected more due to their lower momentum and hit the Tagger hodoscope, which is segmented into 120 channels and has an acceptance from 10 % to 90 % of the beam energy. Taking the Lorentz force into account, the energy of the electrons are determined by the hodoscope segments. The corresponding bremsstrahlung photon has an energy, E_γ, determined from the energy difference of the beam energy, E_0, and detected electron energy, E_f [13].

$$E_\gamma = E_0 - E_f \tag{2.1}$$

The energy resolution of the Tagger is correlated to the photon energy. It ranges from between 0.5 % E_0 for high and 2.2 % E_0 for low photon energies [12]. The energy resolution increases for electrons in the focal plane of the magnet. Only the horizontal part of the Tagger hodoscope is in the focal plane. The vertical part is outside due to the beam dump. As photons are not affected by the magnetic field, they traverse unaffected through the beam pipe to the target. The flux of the photon beam is monitored with the GIM and FluMo detectors at the end of the experiment (see section 2.2.6).

ARGUS

The ARGUS detector was constructed to increase the photon energy resolution which now complements the Tagger hodoscope. ARGUS uses scintillator fibers to detect electrons. Each fiber covers a smaller region than one segment of the Tagger, which leads to a more precise position resolution and thus energy resolution. Measurements showed that the energy resolution of ARGUS is between 0.1 % to 0.4 % of E_0 [14, 15].

Møller detector

Møller scattering is electron-electron scattering with an asymmetry in the spin orientation, as scattering with equal spin is suppressed due to the Pauli principle. It is monitored to determine the polarization of a circularly polarized photon beam. The correlation between bremsstrahlung electron and photon degree of polarization is well known [16]. It is used to determine the photon polarization from the measured electron polarization. To measure the electron polarization via Møller scattering, a polarized electron target is needed. At the BGO-OD experiment the outer shell electrons in a ferromagnetic foil are polarized using a magnetic field. This foil also doubles as a radiator for the bremsstrahlung process, which allows in situ measurements of the polarization during the standard data taking. The Møller detector consists of four small lead glass detectors for electron identification. This detector is positioned outside the plane where the bremsstrahlung electrons traverse and is used to detect Møller scattering pairs. The asymmetry rate then determines the polarization [17].
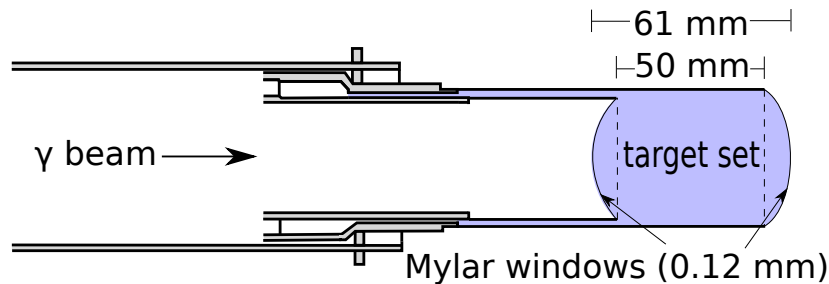
2.2.2 Target

Figure 2.5: Scheme of the target cell. A side view perpendicular to the beam direction is shown. The complete target is in a vacuum. The blue area is filled with the liquid hydrogen or deuterium. The shown dimensions are for the shorter target cell used in the analysis.

At the BGO-OD experiment the target can be liquid hydrogen, deuterium or a solid target. The solid target is not inside the vacuum beam pipe. For this target the photon beam pipe ends after the beam dump. For the liquid hydrogen and deuterium targets, a cryostat system is set up, as both need a temperature of some tens of Kelvin to liquefy. The scheme of the target cell, which holds the liquefied gas, can be seen in figure 2.5. The complete target cell is inside the vacuum beam pipe, so only the liquefied gas and the Mylar[1] windows interact with the photon beam. The shown target cell is 5 cm long, which was replaced by a 10 cm long cell in January 2018. In this thesis only data with the 5 cm cell filled with hydrogen were analyzed. The Mylar windows are 0.12 mm thick and expand outwards due to the pressure difference by around 5.5 mm. This creates an effective target size of 6.1 cm for the 5 cm cell and 11.1 cm for the 10 cm cell.

2.2.3 Central Detectors

The photons travel with the beam pipe until they impinge upon the target cell, which is at the center of the BGO ball. A slice view of the BGO ball is shown in figure 2.6. Surrounding the target is a cylindrical multi-wire proportional chamber (MWPC). This gas detector is used to identify tracks

---

[1] Mylar is a manufacturer for foil made of polyethylene terephthalate

BGO-ball
  480 **Bi**$_4$ **Ge**$_3$ **O**$_{12}$ crystals, 24 cm long ≈ (21X_0)
  32 sectors in φ, φ ∈ [0°,360°] →**φ index**
  15 sectors in θ, θ ∈ [25°,155°] →**θ index**
  from INFN LNF/Roma2/Messina Italy
            (former GRAAL)
Barrel
  5 mm thin NE102 scintillator for ΔE
  measurement
  32 sectors in φ, Δφ = 11.25°
Target
  LH$_2$, LD$_2$ or Nuclear
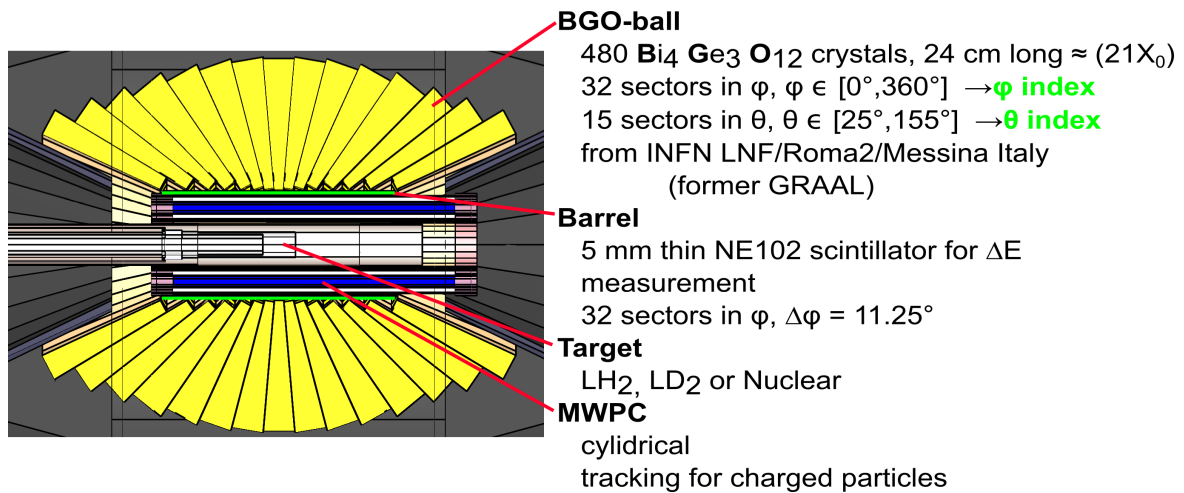**MWPC**
  cylidrical
  tracking for charged particles

Figure 2.6: Slice view of the BGO ball. The Photon beam direction is from left to right. The detector details and positions are indicated in the figure.

of charged particles [18]. The Scintillating Barrel, usually referred to as just the Barrel, surrounds the MWPC and is used for particle identification. The BGO calorimeter surrounding these detectors measures the kinetic energy of particles.

Multi-wire proportional chamber (MWPC)

The MWPC detector refers to two detectors: an inner and outer MWPC, which are used for charged particle tracking [19]. The chambers are constructed in a coaxial cylindrical configuration. The cathodes of this detector are divided into strips with an orientation of 45° for the inner cathodes and −45° for the outer cathodes relative to the wires. This allows position determination with only one chamber. The detector covers all ϕ angles and θ angles between 16° to 155°, which means it has an overlap with the SciRi detector acceptance. In this thesis the MWPC is not used for analysis.

Scintillator Barrel

Surrounding the MWPC are 32 thin plastic scintillator bars of 5 mm thickness arranged in the form of a cylindrical barrel. This detector is used to identify charged particles and measure energy deposition. The energy deposited is only a fraction of the total energy and can be used together with the total deposited energy in the BGO calorimeter for particle identification. Unfortunately the single scintillators are not calibrated yet and this information is not accessible in this thesis. The detector response to a particle however is an indication that the particle was charged and is used to differentiate between charged and neutral particles. The 32 bars divide the ϕ acceptance of the detector into 11.25° segments. One bar covers the θ angles from 25° to 155° [20].

BGO calorimeter

The BGO calorimeter consisting out of 480 bismuth germanium oxide (BGO) crystals is used to measure the kinetic energy and direction of particles. It was originally used in the GRAAL experiment and is optimized for photon detection [21]. The BGO calorimeter has 15 sectors in θ, covering the

angles from 25° to 155°. Each crystal is 24 cm long which correspond to approximately 21 radiation lengths covering $\Delta\phi$ =11.25° for azimuth and $\Delta\theta$ =6° to 10° in polar angle. The advantage of bismuth germanate as a scintillator is the good energy resolution and a small radiation length. The light readout is done via photomultiplier tubes (PMT). With the BGO ball it is possible to measure the kinetic energy of charged particles and photons. High energetic photons create an electromagnetic shower via pair production, Compton scattering and photoelectric effect. The BGO crystal size were optimized with these processes in mind. With the photon energy deposited over multiple crystals the angular resolution of the photon is better than the individual crystal size. More information on the identification of particles in the BGO calorimeter can be found in section 2.3.5.
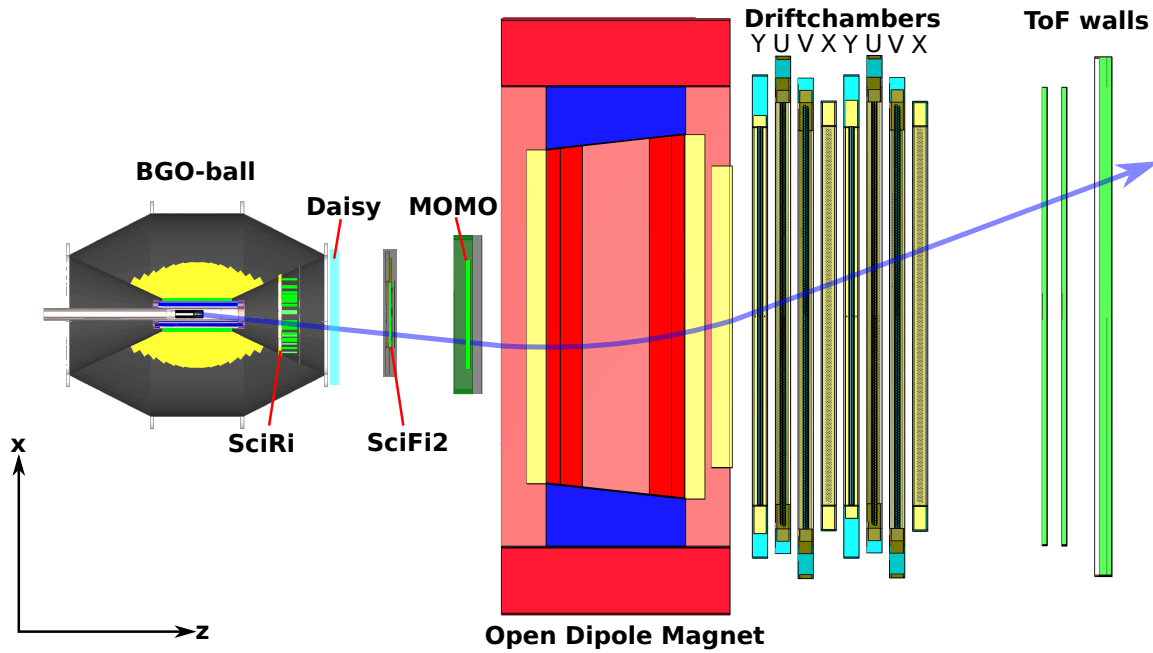

Figure 2.7: Top view of the BGO-OD experiment. The blue line shows the trajectory of a typical charged particle in the magnetic field of the open dipole magnet. The drift chamber 'Y' has the wires horizontally orientated, while the drift chamber 'X' has vertical orientation. Drift chambers 'U' and 'V' are rotated by ±9° relatively to the 'X' chamber. Other detectors are explained in more detail in the text.

2.2.4 Intermediate Detectors

Particles moving in a forward direction with θ lower than 25° are outside of the BGO detector acceptance. In the θ region of 10° to 25°, charged particles are detected by the intermediate detectors, Daisy and SciRi, shown in figure 2.7. Both detectors are placed between MOMO and the BGO calorimeter.

SciRi

The Scintillating Ring (SciRi) was built to plug the θ acceptance hole of 10° to 25°. It consists of 96 plastic scintillators with 32 divisions in ϕ and 3 segments in θ. The read out is done using avalanche
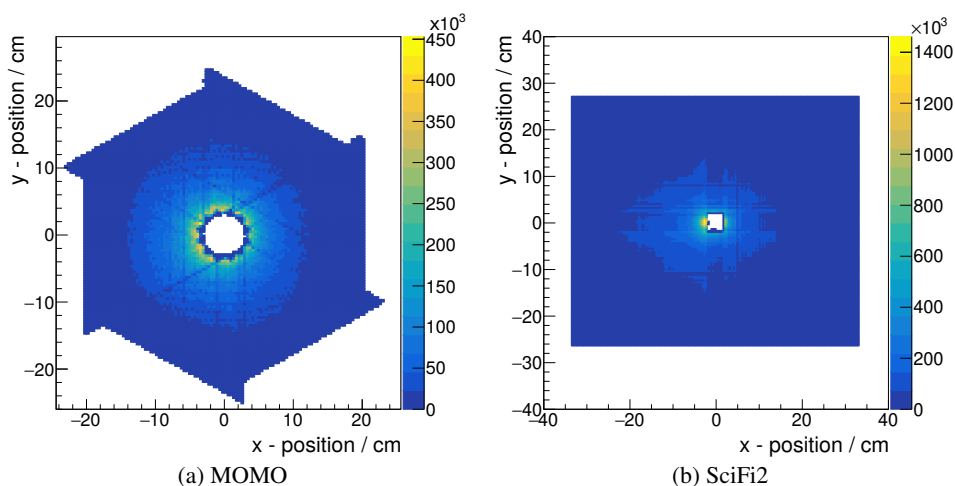
(a) MOMO

(b) SciFi2

Figure 2.8: Particle position distribution measured by MOMO and SciFi2. The colors indicate the intensity.

photo-diodes generously provided by the Crystal Barrel experiment [22].

Daisy

The Daisy detector consists of multi-gap resistive plate chambers (MRPC). This detector is under commission and will cover θ from $8°$ to $25°$ [23]. The advantage of this detector is the high-detection efficiency, accurate θ measurement and a time resolution of approximately 50 ps, which will allow for time-of-flight measurements.

2.2.5 Forward Spectrometer

If the θ angle of a charged particle is smaller than $10°$, the momentum and time of flight are measured with the forward spectrometer. An overview of the spectrometer can be seen in figure 2.7. The open dipole magnet is used to deflect charged particles with its magnetic field. Tracking detectors before and after the magnet measure the particle direction from which the momentum can then be determined. Downstream of the open dipole magnet, three scintillator walls (ToF) are used to measure the time of flight which is used for particle identification [24–27].

MOMO and SciFi2

MOMO and SciFi2 are both scintillating fiber detectors which are used to measure the particle direction upstream of the magnet. The readout of the light is done via PMTs with strong shielding against magnetic fields [24]. In figures 2.8 the distribution of measured particles in the MOMO and SciFi2 are shown. The difference in shape between MOMO and SciFi2 is the result of the scintillating fiber orientation.

Open Dipole Magnet

The open dipole magnet used in the BGO-OD experiment is on permanent loan from DESY. It produces a magnetic field up to 0.4 T and also has a fringe field in the close proximity. This fringe field, unfortunately, negatively impacts PMTs by reducing their overall gain [25].

Drift chambers

The particle trajectory downstream from the magnet is measured with 8 drift chambers. Each chamber consists of 2 layers, each with a series of parallel wires. The orientation of these wires is described in figure 2.7 together with their positions[26].

ToF

Three walls with horizontal plastic scintillator bars are used to measure the time of flight. These bars are read out with a PMT on each end. This allows for the determination of the horizontal hit position of the particle from the time difference between the two PMTs, which are at either end of the scintillator. The vertical position is given by the bar position. The time information from the Tagger is used as a start for the time of flight measurement [27]. The distance between Tagger and target is subtracted from this time.

2.2.6 Flux monitors

The photon flux is monitored at the end of the experiment by the GIM[2] and FluMo[3] detectors [28],[29] as seen in figure 2.9. The photon flux determination is explained in more detail in section 4.2.
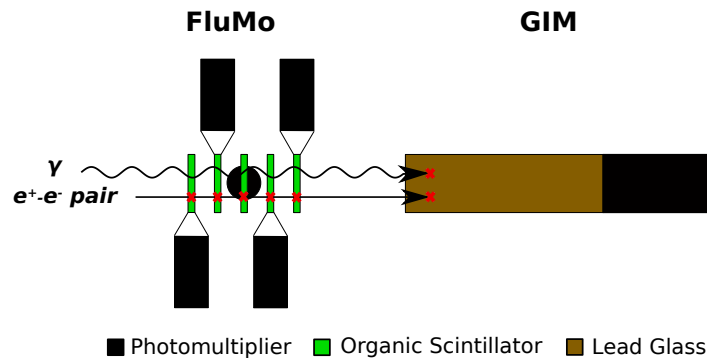

Figure 2.9: Overview of the flux monitors. The color scheme in the figure shows the components of the detectors. The photon beam moves from left to right. The photons will not be detected in the FluMo detector in contrast to the electron positron pairs.

FluMo

The FluMo is used to monitor the photon flux during data taking. It consists of 5 small scintillator detectors. The photon detection is done indirectly through electron-positron production. Everything between the open dipole magnet and the detector is used as conversion material for this process. The electronic signal for electron-positron pairs is twice as high compared to single electron. With this the events can be clearly identified. The probability for the electron-positron event to occur is determined using the GIM detector. Knowing this, the FluMo counts a number of events proportional to the number of photons.

---

[2] **G**amma **I**ntensity **M**onitor
[3] **Flu**x **Mo**nitor

GIM

The GIM detector located behind the FluMo detector is a lead glass detector with photomultiplier readout. This type of detector has almost 100 % detection efficiency. While it is possible to detect photons with this detector accurately, the high photon flux during data taking reduces the efficiency due to dead time effects. Using lower beam currents this detector is used to determine electron-positron conversion ratio for the FluMo detector.

2.3 Particle identification and momentum determination

The identification of particles in the BGO-OD experiment using the aforementioned detectors is shown here in more detail. The flux monitors are needed to monitor the photon beam flux, which is not part of a reaction identification, but is crucial for the cross section determination and thus is explained later in section 4.2.

2.3.1 ExPlORA analysis framework for real and simulated data

Most of the analysis at the BGO-OD experiment begins with the ExPlORA [4] framework. This is thoroughly explained in more detail in the PhD thesis of Oliver Freyermuth [30]. ExPlORA is a C++ extension to the ROOT library. It is used to analyse raw data as well as simulated data.

Simulation data is achieved by two steps. First the kinematics of a reaction are calculated and the first generation particles are created at nominal positions using an event generator. This includes a post-bremsstrahlung electron at the radiator position for the Tagger and the final-state particles of the reaction before the decay.

Afterwards the particle decay and energy deposit is simulated via Monte Carlo methods. For this the complete BGO-OD experiment geometry and magnetic fields are implemented in the ExPlORA framework. Geant4[5] is used to simulate particle passage through material and subsequent reactions [31]. From this the deposited energy in each active material of a detector can be determined. If the energy exceeds a set threshold a detector hit is created and a raw data tree similar to real data is built. From this point on, the analysis follows the same steps as real data described in section 2.3.3.

2.3.2 Particle acceptance overview

For reaction identification the Tagger is crucial to measure the initial photon energy. The target proton is assumed to be at rest. With this the center of mass energy state of the reaction is determined. In figure 2.10 the detectors used to identify the final-state of the reaction are shown. In this thesis the MWPC and MRPC are not used and thus not drawn. The complete detector system is divided into regions depending on the θ acceptance. Particles with θ from 2° to 10° will be detected in the Forward Region, which is covered by the forward spectrometer. Charged particles with θ from 10° to 25° are detected in the Intermediate Region by SciRi. This plastic scintillator detector only records the particle position. The region from 25° to 155° is the Central Region and is the only region with efficient neutral particle detection. The main detector here is the BGO calorimeter, which is an excellent photon detector. The Barrel in front of the calorimeter crystals allows for charge identification.

---

[4] **Ex**tended **Pl**uggable **O**bjectoriented **R**OOT-ified **A**nalysis
[5] **Ge**ometry **an**d **T**racking 4 is a toolkit for Monte-Carlo method of particles passage through matter
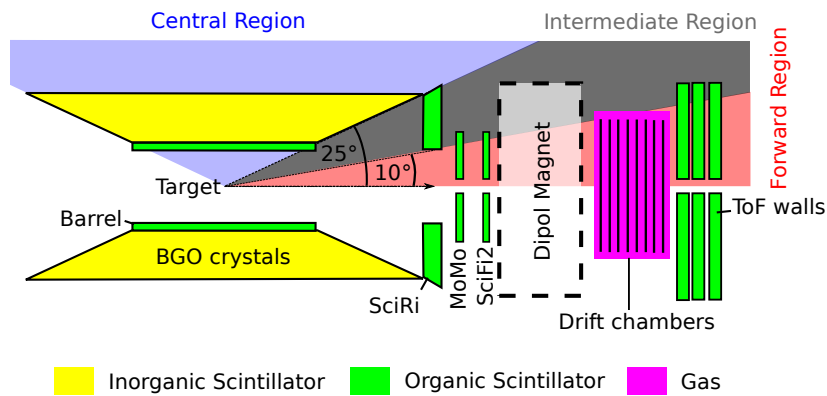
Figure 2.10: Overview of the detector polar angle acceptance. This figure is not to scale. The identification of the particles is divided into three different regions, and the areas are colored depending on the detection mechanism.
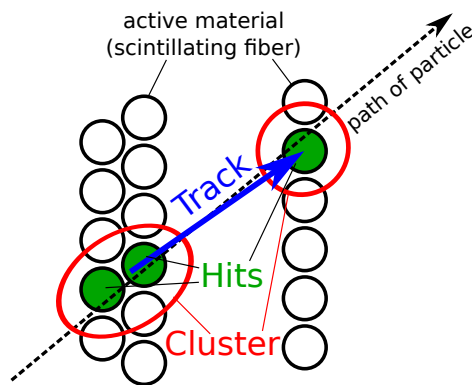
2.3.3 Hits, Clusters and Tracks

Figure 2.11: Picture shows basic reconstruction of a particle track. Hits(green) are added to form a cluster(red). Clusters in different detectors are used to determine the track of the particle.

The definition of a hit, cluster and track are elaborated in this section. Each detector segment registers a hit if the electrical signal corresponding to the deposited energy exceeds a preset threshold. A cluster is a combination of hits. It adds all activated detector segments corresponding to the same particle, usually due to their space and time correlation. The size of the cluster depends on the detector geometry and particle type. With the construction of clusters the detector space resolution improves in comparison to a single segment size. Figure 2.11 illustrates the relationship between hit, cluster and track.

Tracks can be formed with the clusters and hits from different detectors. All the information from the detectors inside the same acceptance region shown in figure 2.10 are combined into a single track. For the forward spectrometer, SciFi2 and MOMO are used to identify the particle trajectory before the open dipole magnet while the drift chambers and ToF wall are responsible for the trajectory after the magnet. This allows for a good tracking of the particle from target to ToF walls. Not all track types have the same saved parameters. The intermediate tracks only consists of SciRi detector hits. In this

track type	involved detectors	measured parameters
Tagger track	Tagger ARGUS	initial photon energy E_γ
Central track	BGO Barrel	kinetic energy position discriminates charged and neutral particles
Intermediate track	SciRi	position
Forward track	MOMO SciFi2 Drift chambers ToF	momentum direction time of flight charge

Table 2.1: Different tracks constructed from involved detectors and the provided information. Every detector has a time information correlated to the trigger and is not listed in this table as a separate point.

case the trajectory of the track originates from the center of the target. Table 2.1 lists the tracks types and descriptions. The tracks are described into more detail in the following sections. The Tagger tracks in section 2.3.4, central tracks in section 2.3.5, intermediate tracks in section 2.3.6 and forward tracks in section 2.3.7.

2.3.4 Tagger tracks

The tagger tracks are the combined information of the Tagger and the ARGUS detector. In the region where both detectors overlap, the ARGUS detector is used to determine the initial photon energy, E_γ. If ARGUS has no coincidence in time with the Tagger, only the Tagger information is used and the ARGUS cluster is ignored.
In figure 2.15(a) the tagger track time distribution to the event trigger is shown. The ARGUS has a worse time resolution in comparison to the Tagger, and so a Tagger cluster is mandatory for a tagger track. The peaks represent the electron bunch structure in the 500 MHz accelerator. Aside from the prompt peak at time from -1 ns to 1 ns, the peaks do not have any correlation with hadronic events and are just accidental coincidences. These events are removed by a time selection cut from -1.5 ns to 1.5 ns marked by the red lines.

2.3.5 Central tracks

For the central tracks the information from the BGO and Barrel detector are combined. The BGO is an electromagnetic calorimeter and thus is optimized for photon and electron detection. Part of the BGO calorimeter is shown in figure 2.12. The left picture illustrates a proton depositing energy in only one crystal. Heavy charged particles such as protons, $\pi^\pm$ and $K^\pm$ lose their energy mostly via Bethe-Bloch ionization. The resulting direction resolution of these particles is limited by the crystal size. The right figure shows a photon depositing energy in multiple crystals due to the creation of an electromagnetic shower via pair production and bremsstrahlung. In this case, the direction of the photon cluster is determined by all detector segments weighted by their measured energy.
Clusters are formed from the single crystal hits in the BGO calorimeter, using space and time correlation. The total energy in the cluster against the number of hits forming the cluster are plotted in figure 2.13. With higher energy photons, the electromagnetic shower distribute more energy over multiple crystals. In theory the transverse shower development is given by the Molière radius and is
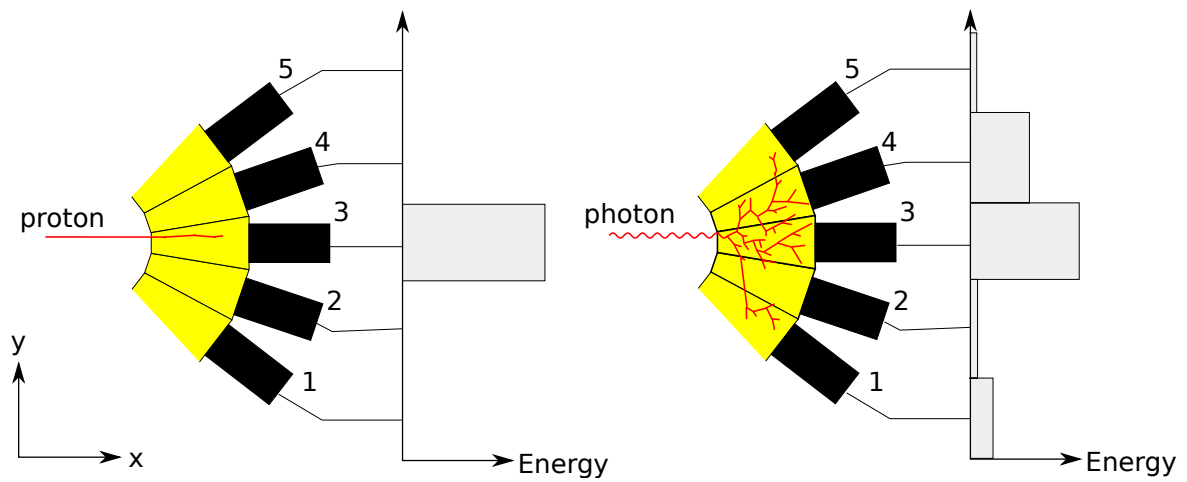
Figure 2.12: Creation of clusters in the BGO calorimeter. The yellow area marks individual scintillator crystals. The deposited energy is read out by the photomultiplier (PMT), which are marked by black boxes. The PMT channel is drawn against measured energy right to the PMT. The illustration shows how proton (left) and photon (right) deposit their energy in the calorimeter.
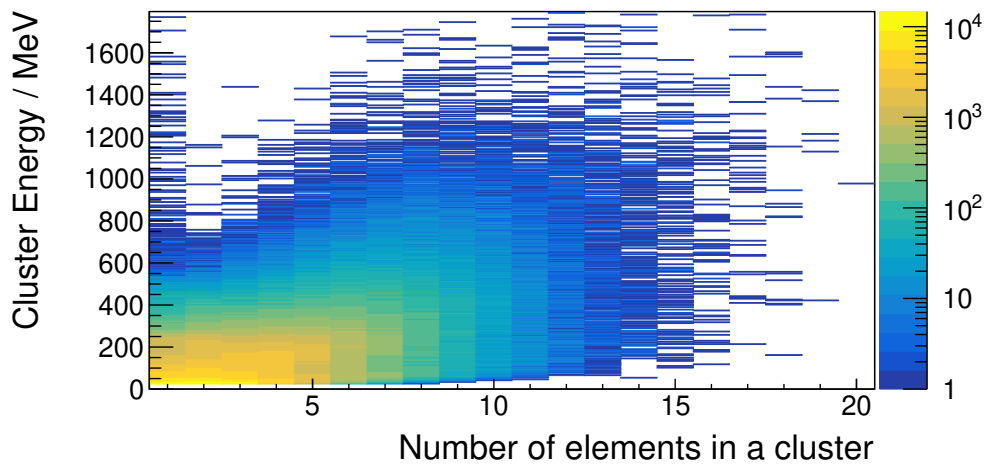

Figure 2.13: Cluster energy against number of hits in a cluster in the BGO calorimeter.

energy independent [3]. The expectation would be that the cluster size would be constant over energy. In reality the shower is of statistical nature and each detector segment suppresses low energy signals to remove detector noise. With higher photon energy, more segments surpass this threshold, thus the number of hits in cluster rises. The vertical line for exactly one hit in the cluster is due to the heavy charged particles, as they only deposit their energy in one or two crystals. This information is not used during the event identification, because it reduces the statistics as there is no clear discrimination between both possibilities.

In figure 2.12 a typical photon cluster is seen in the right figure. For a single event the energy deposited in the crystals is not perfectly Gaussian distributed due to the statistical nature of the electromagnetic shower development. This can lead to a split-off cluster. A detector registers hits only if the deposited energy exceeds a preset threshold. If the threshold in the figure is higher then the energy deposited for segment number 2, the segment signal number 1 will not be distinguishable from a low energetic proton. Thus two separate clusters can be registered from only one photon.

Figure 2.14: Barrel hit and BGO cluster ϕ difference. The red line marks the selection cut for the interpretation of a coincidence between both.

The BGO clusters are combined with the hits in the scintillating Barrel to form central tracks. The association of the two is done via the ϕ angle and time difference. The phi difference between both detector hits is shown in figure 2.14. The red lines mark the angle difference selection cut of $-20°$ to $20°$. The regularly appearing spikes are $11.25°$ apart and are created by heavy charged particles depositing energy in only one crystal, which limits the ϕ resolution to the crystal size.

The final central tracks are created by removing all tracks which are not coincident with the triggered initial photon. The time distribution relative to the trigger can be seen in figure 2.15(b). The time difference between the bremsstrahlung event and the associated hadron event is subtracted together with the target to the calorimeter distance. This results in a time distribution centered around zero and events between -5 ns to 5 ns are selected for further analysis.

2.3.6 Intermediate Tracks

The intermediate tracks usually consist of a single SciRi hit. Clusters in SciRi are only formed by particles which pass exactly between two scintillators, which only happens in 4 % of the events. Due to the avalanche photodiode readout of the detector, the detector time resolution is limited compared to a photomultiplier readout. The time distribution is seen in figure 2.15(c), with a selection cut of -50 ns to 50 ns applied. The avalanche photodiode was originally designed for inorganic scintillators with higher light output and needed adjustments. The energy resolution of this diode was sacrificed in favor of detection efficiency, therefore the energy information can not be used reliably for particle identification.
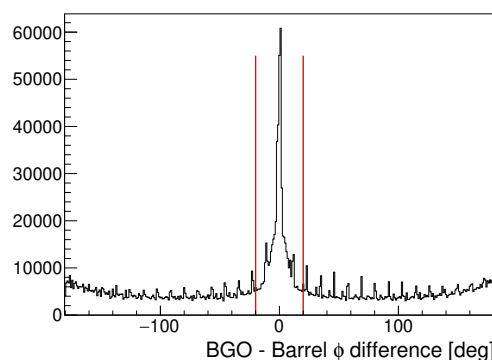
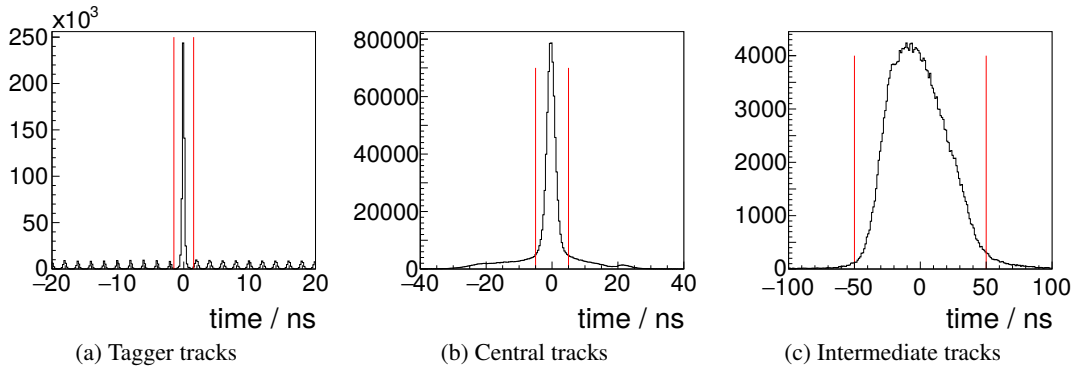(a) Tagger tracks (b) Central tracks (c) Intermediate tracks

Figure 2.15: Time distribution correlated to the trigger with time selection cuts marked by red lines. (a) through (c) show different detector regions. The time offset between trigger attempt and detector hit is already subtracted from the time difference.

2.3.7 Forward Tracks

The forward tracks combine information from MOMO, SciFi2, drift chambers and ToF walls. Complete overview of the detectors is seen in figure 2.7. The track before the open dipole magnet using the SciFi2 and MOMO detector is mandatory to form a track. The particle trajectory is determined before the magnet using the SciFi2 and MOMO. All particles not originating from the target are rejected. All tracks require at least one cluster in the ToF walls[32]. Hits in the three ToF walls are added to a cluster provided the position and time of the hits agree. The trajectory from MOMO and SciFi2 are extrapolated to the ToF z-position and the y-difference is used for ToF cluster association. The first estimate on the track trajectory after the magnet is then determined by the extrapolated MOMO and SciFi2 track to the magnet center and the ToF position. To this trajectory the closest drift chambers hits are associated. Afterwards the track is fitted to archive optimal results, which includes energy loss due to Bethe-Bloch ionization.
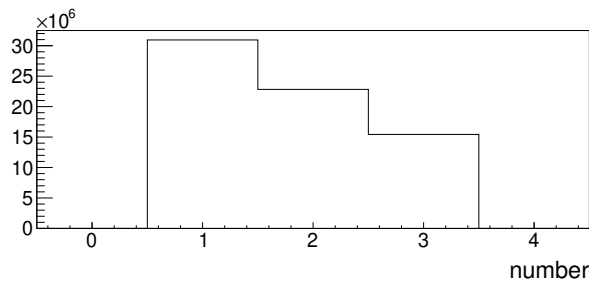

Figure 2.16: Number of ToF walls in a forward track.

The BGO-OD experiment has three separate ToF walls. In figure 2.16 the number of ToF walls in a complete track are shown. Tracks with only one ToF wall are more common as particles with low momentum are stopped by the first wall. In figures 2.17(b) and 2.17(a) the number of drift chambers inside a forward track are shown for two different running periods. In the November 2015 running period, the drift chamber efficiency was lower than usual, which resulted in poor identification efficiency if all drift chambers are required for the track. The problem was identified and corrected in the April 2017 running period. In this thesis both running periods are used to analyse data.
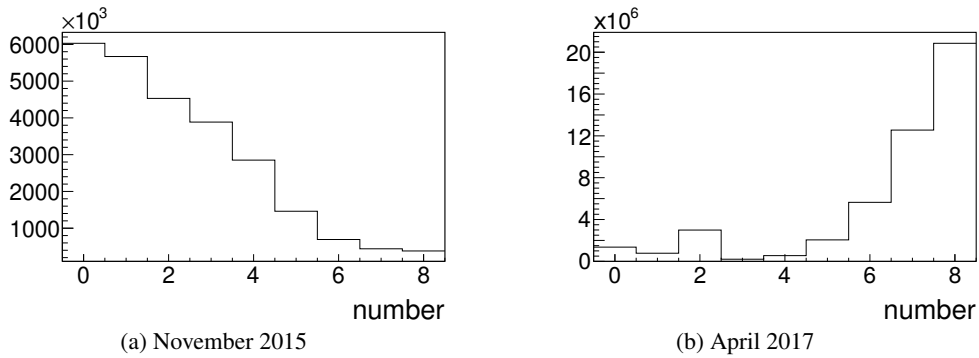
(a) November 2015

(b) April 2017

Figure 2.17: Number of drift chambers in a forward track for different running periods. (a) shows the November 2015 running period, where the drift chambers were less efficient then usual due to lower high voltage. As such the distribution is shifted to the left. For track identification not all 8 drift chambers are required.
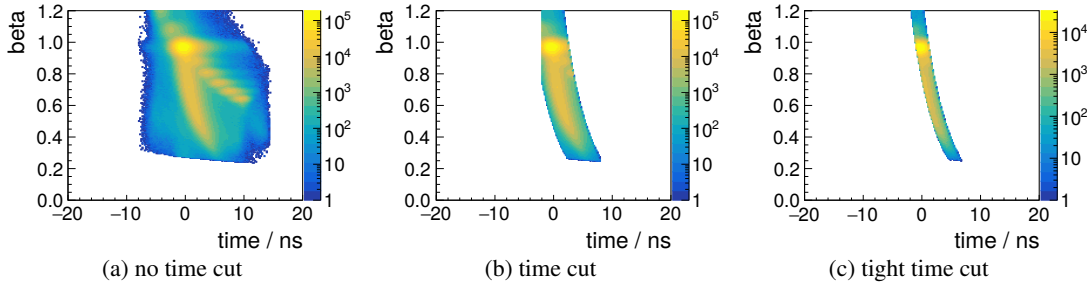

(a) no time cut

(b) time cut

(c) tight time cut

Figure 2.18: Particle velocity β vs MOMO and SciFi2 time. The high rate in the Tagger leads to accidental coincidences visible as peaks next to the β-time relation in (a). In (b) these combinatorics are removed by a selection cut. In (c) the time cut is more narrow removing more wrong combinations.
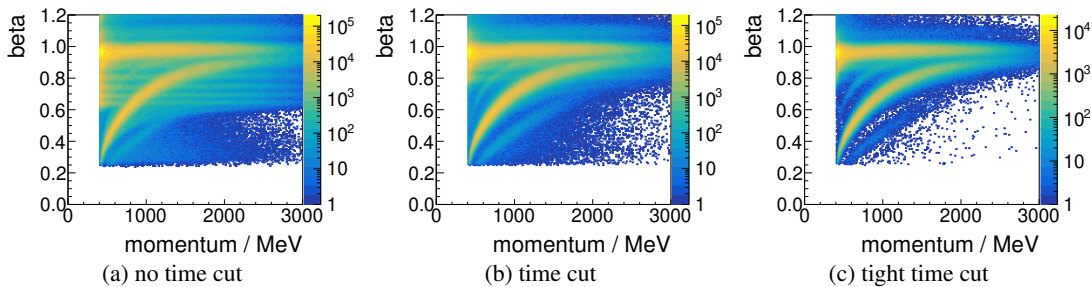

(a) no time cut

(b) time cut

(c) tight time cut

Figure 2.19: Particle velocity β against momentum in the forward spectrometer. The relation between velocity and momentum can be used to identify particle types. In (a) all forward tracks are seen. The wrong combinations are removed in (b) by the time selection cut of figure 2.18(b). (c) shows the distribution after the more restricted cut in figure 2.18(c). The visible lines correspond to the particle type. From top to bottom the particles are: electrons/pions, kaons, protons and deuterons.

For the time of flight, the ToF walls only measure the time at the end of the track. The Tagger time is used as a start time for the track. Time of flight for a low energetic proton can reach up to 40 ns. With such a big time window accidental coincidences can occur. In figure 2.18(a) the particle velocity β is plotted with respect to the time from MOMO and SciFi2. The correlation between time and velocity is particle type independent and can thus be used to reduce accidental coincidences. Some times the

wrong bremsstrahlung electron is used as the start time for the β determination, which is represented by additional peaks next to the expected β-time correlation. Wrong electron bunches can be removed by cutting into the two dimensional distribution shown in figure 2.18(b). This improves the β against momentum, p, distribution shown in figure 2.19(b). There is clear correlation between velocity and momentum, which is depending on particle mass m:

$$m = \sqrt{\left(\frac{p}{\beta}\right)^2 - p^2} \tag{2.2}$$

In figure 2.20 the particle mass determined from velocity β and momentum is drawn after the time selection cut. If the time selection cut is made more narrow like in figure 2.18(c), the β against momentum plot improves further as is seen in figure 2.19(c). Due to the reduction of statistic this narrow cut is not used.
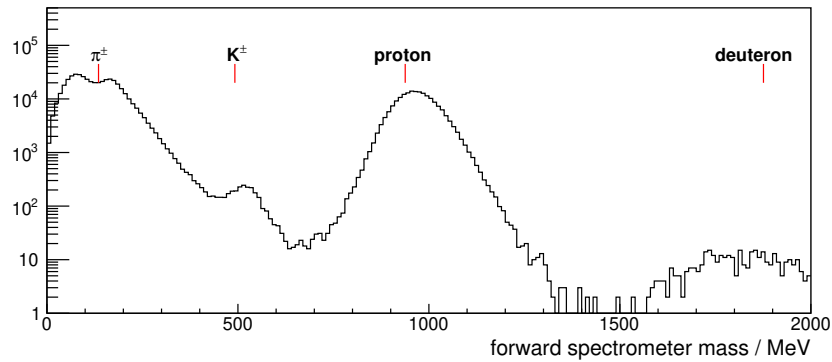

Figure 2.20: Particle mass determined from β and momentum. To reduce background only particles with momentum smaller then 900 MeV and the selection cut from figure 2.18(c) were used. Visible peaks correspond to particles in the figure. The deuteron peak originates from the target windows.

Analysis tools

This chapter shows the analysis techniques and tools used in this thesis. The basis for all analyses are the kinematic relations shown in section 3.1. For this thesis the improvement of the resolution of measured energy and momentum was mandatory to investigate more complex reactions. This was achieved with a kinematic fit, which was implemented into the ExPlORA framework during this thesis, and is explained in section 3.2. To extract the cross section of a reaction, the signal must be separated from a background of other hadronic reactions. This was achieved with the RooFit[33] library of the ROOT package, explained in section 3.3.

3.1 Kinematic relations

The trajectory of a particle can be described by its four-momentum. The single components of the four-momentum for a particle, $\boldsymbol{a}$, are written as:

$$\boldsymbol{a} = \begin{pmatrix} E \\ p_x \\ p_y \\ p_z \end{pmatrix} = \begin{pmatrix} E \\ \vec{p} \end{pmatrix} \tag{3.1}$$

With the mass of the particle m defined by its energy E and momentum $\vec{p}$ as $\sqrt{E^2 - (\vec{p})^2}$. With this definition the initial state for photoproduction in the BGO-OD experiment coordinate system (cf. section 2.2) can be written as:

$$\begin{pmatrix} E_\gamma \\ 0 \\ 0 \\ E_\gamma \end{pmatrix} + \begin{pmatrix} m_p \\ 0 \\ 0 \\ 0 \end{pmatrix} = \gamma_i \quad + \quad \boldsymbol{p}_i \tag{3.2}$$

With initial photon γ_i energy E_γ and proton p_i mass m_p. This assumes a beam along the z-axis and target proton at rest. As an example, 4-momentum conservation requires that the reaction, $\gamma p \rightarrow \pi^0 p$, fulfills:

$$\gamma_i + \boldsymbol{p}_i = \pi_f^0 + \boldsymbol{p}_f = \gamma_f^1 + \gamma_f^2 + \boldsymbol{p}_f \tag{3.3}$$

In this example, the π^0 decays into two photons. The invariant mass of the two photons yield the π^0 mass and can be used to identify the π^0 particle at the final-state:

$$\gamma\gamma \text{ invariant mass} : |\boldsymbol{\gamma}_f^1 + \boldsymbol{\gamma}_f^2| = m_{\pi^0} \tag{3.4}$$

If a particle was not detected, it is possible to determine the missing four-momentum and from this the missing mass. A missing proton in the same example reaction can be determined with the two final-state photons and the initial state:

$$\text{missing mass to } \gamma\gamma : |\boldsymbol{\gamma}_i + \boldsymbol{p}_i - \boldsymbol{\gamma}_f^1 - \boldsymbol{\gamma}_f^2| = |\boldsymbol{p}_f| = m_p \tag{3.5}$$

Most identifications in this thesis require the detection of all particles. In such cases the missing mass in the total reaction can be determined by subtracting the initial state mass and final-state mass:

$$\text{total missing mass} : |initial\ state| - |final\ state| = W_i - W_f = |\boldsymbol{\gamma}_i + \boldsymbol{p}_i| - |\boldsymbol{\pi}_f^0 + \boldsymbol{p}_f| = 0 \tag{3.6}$$

Here W is the mass in the center of mass frame, which can be determined from either the initial or final-state. This equation will be referred to as **total missing mass** during the identification in section 5.

Using the direction information and the momentum conservation of a reaction can be used to calculate the momentum of up to three particles[22]. The only remaining degree of freedom is energy conservation, which is not fulfilled if the wrong masses are associated to the particles. The determination of the momentum in this way ignores the angular resolution of the detectors, which leads to uncertainties in the momentum calculation. Including the detector resolution of the angle and momentum allows a likelihood fitting to the optimal values. This procedure is referred to as kinematic fit.

3.2 Kinematic fit

The measured direction, momentum or energy information of a detected particle always differ from its true value due to the detector resolutions. All reactions fulfill momentum and energy conservation and these constraints can be used to improve the detector resolution. This method is called a kinematic fit and was implemented in the BGO-OD software framework ExPlORA as part of this thesis. A summary is presented here. For a detailed description of kinematic fitter see the lecture notes of Paul Avery [34].

3.2.1 Theory

The kinematic fit uses the method of Lagrange multiplier to find the solution. This method generally describes the solution of a mathematical problem where a multidimensional function is maximized or minimized while a set condition is fulfilled. As an example, consider the function $f(x, y) = yx$ which must be maximized, while $y^2 + x^2 = 18$ is fulfilled. By introducing a new variable, λ, one can form the Lagrange function $L(x, y, \lambda)$ (3.7).

$$L(x, y, \lambda) = f(x, y) + \lambda(condition)$$
$$L(x, y, \lambda) = yx + \lambda(y^2 + x^2 - 18) \tag{3.7}$$

With the introduction of the variable λ it can be shown that $\frac{\delta L(x,y,\lambda)}{\delta y} = \frac{\delta L(x,y,\lambda)}{\delta x} = \frac{\delta L(x,y,\lambda)}{\delta \lambda} = 0$. In the previous example one gains three equations (3.8).

$$
\begin{aligned}
\frac{\delta L(x, y, \lambda)}{\delta y} &= & x + \lambda 2y & = 0 \rightarrow \lambda = -\frac{x}{2y} \\
\frac{\delta L(x, y, \lambda)}{\delta x} &= & y + \lambda 2x & = 0 \rightarrow \lambda = -\frac{y}{2x} \rightarrow x^2 = y^2 \\
\frac{\delta L(x, y, \lambda)}{\delta \lambda} &= & y^2 + x^2 - 18 & = 0 \rightarrow \{x_{1,2} = \pm 3, y_{1,2} = \pm 3\}
\end{aligned}
\tag{3.8}
$$

From these equations the solutions $\{x_{1,2} = \pm 3, y_{1,2} = \pm 3\}$ are obtained. After inserting the solutions into $f(x, y)$ the correct results $f(3, 3)$ and $f(-3, -3)$ are confirmed. The constraint was quadratic, so two solutions are obtained, which is not desirable in a kinematic fit. To use the method of Lagrange multiplier in the kinematic fit some adjustments and assumptions needs to be applied.

First, the function to be minimized, χ^2, (3.9) is defined. This is the summed difference of all measured parameters, y_l, and expected parameters, $f_l(\alpha)$, divided by the known standard deviation σ_l of that parameter. By minimizing this function, a simple least squares fitting is achieved. The expected values $f_l(\alpha)$ are obtained during the fit and fulfill the constraints. One important point is that it is assumed that the error of the parameters are Gaussian distributed. If one of the parameters is not Gaussian distributed the following approximations will result in a non optimal solution.

$$
\chi^2 = \sum_l \frac{(y_l - f_l(\alpha))^2}{\sigma_l^2}
\tag{3.9}
$$

One important approximation in the kinematic fit is the assumption that the expected value $f_l(\alpha)$ does not deviate significantly from the measured value y_l to allow a linear approximation of the $f_l(\alpha)$ (3.10) function by using a first order Taylor expansion.

$$
f_l(\alpha) = f_l(\alpha_A) + \sum_i (\alpha_i - \alpha_{iA}) \frac{\delta f_l(\alpha)}{\delta \alpha_i} \equiv f_{lA} + \sum_i A_{li} \eta_i
$$
$$
\Rightarrow \chi^2 \equiv \sum_l \frac{(\Delta y_l - \sum_i A_{li} \eta_i)^2}{\sigma_l^2}
\tag{3.10}
$$

With further steps, the matrix form of χ^2 (3.11) can be formulated[35]. This introduces the error covariance matrix $\mathbf{V}_y^{-1}$, defined by $cov(x_i, x_j) \equiv \mathbf{V}_{xij} = \langle (x_i - \bar{x}_i)(x_j - \bar{x}_j) \rangle \equiv \langle \delta x_i \delta x_j \rangle$.

$$
\chi^2 = (\Delta \boldsymbol{y} - \mathbf{A}\alpha)^t \mathbf{V}_y^{-1} (\Delta \boldsymbol{y} - \mathbf{A}\alpha)
\tag{3.11}
$$

The constraints on the kinematic fit are usually energy and momentum conservation, but for now the generic constraint vector $\mathbf{H}(\alpha) = 0$ is introduced. With a similar argument as for the χ^2, a linear approximation of $\mathbf{H}(\alpha)$ around point α_A (3.12) is formed.

$$
\mathbf{H}(\alpha_A) + \frac{\delta \mathbf{H}(\alpha_A)}{\delta \alpha}(\alpha - \alpha_A) \equiv \mathbf{d} + \mathbf{D}\delta \boldsymbol{\alpha} = 0
\tag{3.12}
$$

With both χ^2 and $\mathbf{H}(\alpha)$ linearized, the method of Lagrange multiplier has only one solution. The

Lagrange function is defined by equation (3.13). One can rewrite this equation as equation (3.14) by splitting the constant part from χ^2. The goal is the minimization of χ^2 and not the absolute value, so the constant part of χ^2 can be ignored. The Lagrange function for the kinematic fit is then constructed (3.14).

$$
\begin{aligned}
\chi^2 &= (\Delta \mathbf{y} - \mathbf{A}\alpha)^t \mathbf{V}_y^{-1}(\Delta \mathbf{y} - \mathbf{A}\alpha) + 2\lambda^t(\mathbf{d} + \mathbf{D}\delta\alpha) & (3.13) \\
\chi^2 &= (\Delta \mathbf{y} - \mathbf{A}\alpha_0)^t \mathbf{V}_y^{-1}(\Delta \mathbf{y} - \mathbf{A}\alpha_0) + (\alpha - \alpha_0)^t \mathbf{V}_{\alpha_0}^{-1}(\alpha - \alpha_0) \\
&\quad + 2\lambda^t(\mathbf{d} + \mathbf{D}\delta\alpha) \\
\chi^2 &= (\alpha - \alpha_0)^t \mathbf{V}_{\alpha_0}^{-1}(\alpha - \alpha_0) + 2\lambda^t(\mathbf{d} + \mathbf{D}\delta\alpha) & (3.14)
\end{aligned}
$$

With the derivatives $\frac{\delta\chi^2}{\delta\alpha} = 0$ and $\frac{\delta\chi^2}{\delta\lambda} = 0$, the Lagrange function can be solved, resulting in equation (3.15) [34]. $\delta\alpha_0 = \alpha_0 - \alpha_A$ where α_A is the evaluation point for the Taylor expansion and α_0 are the measured values.

$$
\begin{aligned}
&\rightarrow \quad \mathbf{V_D} = (\mathbf{D}\mathbf{V}_{\alpha_0}\mathbf{D^T})^{-1} \\
&\rightarrow \quad \lambda = \mathbf{V_D}(\mathbf{D}\delta\alpha_0 + \mathbf{d}) \\
&\rightarrow \quad \alpha = \alpha_0 - \mathbf{V}_{\alpha_0}\mathbf{D^T}\lambda \\
&\rightarrow \quad \mathbf{V}_\alpha = \mathbf{V}_{\alpha_0} - \mathbf{V}_{\alpha_0}\mathbf{D^T}\mathbf{V_D}\mathbf{D}\mathbf{V}_{\alpha_0} \\
&\Rightarrow \quad \chi^2 = \lambda^{\mathbf{T}}\mathbf{V_D^{-1}}\lambda = \lambda^T(\mathbf{D}\delta\alpha_0 + \mathbf{d}) & (3.15)
\end{aligned}
$$

Simple Example: $\pi^0 \rightarrow 2\gamma$

To calculate the expected values, α, first the measured vector, α_0, and its covariance matrix, $\mathbf{V}_{\alpha_0}$ is set. As an example, consider two photons produced in a π^0 decay. The α_0 vector would be formed out of these two measured photons four-momentum $\alpha^0 = \{\alpha_1^0, \alpha_2^0\}$. Together with the covariance matrix $\mathbf{V}_{\alpha_0}$ the vectors and matrix would look like equation (3.16).

$$
\alpha_1^0 = \begin{pmatrix} p_1^x \\ p_1^y \\ p_1^z \\ E_1 \end{pmatrix} \qquad
\alpha_2^0 = \begin{pmatrix} p_2^x \\ p_2^y \\ p_2^z \\ E_2 \end{pmatrix} \qquad
\mathbf{V}_{\alpha_0} = \begin{pmatrix}
(\delta p_1^x)^2 & \delta p_1^x \delta p_1^y & \cdots & \delta p_1^x \delta E_2 \\
\delta p_1^x \delta p_1^y & \ddots & & \vdots \\
\vdots & & \ddots & \delta E_2 \delta p_2^z \\
\delta E_2 \delta p_1^x & \cdots & \delta E_2 \delta p_2^z & (\delta E_2)^2
\end{pmatrix} \tag{3.16}
$$

The constraint in this example is the invariant mass of the two photons, which should equal the π^0 mass. The constraint vector, $\mathbf{H}(\alpha)$, has only one dimension:

$$
H(\alpha) = 0 = (E_1 + E_2)^2 - (p_1^x + p_2^x)^2 - (p_1^y + p_2^y)^2 - (p_1^z + p_2^z)^2 - m_{\pi^0}^2 \tag{3.17}
$$

The constraint is approximated around the point α_A, which here is equal to α_0. The mass of a photon is zero, so one can also write equation (3.18) for the $\mathbf{d}$ vector. Then $\mathbf{D}$ is given by equation (3.19).

$$
\mathbf{H}(\alpha^0) = 0 = E_1 E_2 - p_1^x p_2^x - p_1^y p_2^y - p_1^z p_2^z - \frac{1}{2}m_{\pi^0}^2 = \mathbf{d} \tag{3.18}
$$

$$
\mathbf{D} = \frac{\delta\mathbf{H}(\alpha_0)}{\delta\alpha} = (-p_2^x, -p_2^y, -p_2^z, E_2, 0, 0, 0, -p_1^x, -p_1^y, -p_1^z, E_1, 0, 0, 0) \tag{3.19}
$$

From this the kinematic fit can be solved with the equations (3.15) in the given order.

Error handling

After the kinematic fit, the fitted parameters fulfill the set constraints. The deviation of the fitted parameters to their initial values is expressed by the pull distribution, f_{pull}, which is normalized by equation (3.20). If the parameter errors are well understood, the pull distributions will be a Gaussian function with a width of sigma equal one. If sigma is smaller than one, the estimated parameter error is too big and vice versa. Note that a non Gaussian error distribution will also lead to a non Gaussian pull distribution.

$$f_{pull} = \frac{\alpha_0 - \alpha}{\sqrt{\sigma_{\alpha_0}^2 - \sigma_\alpha^2}} \qquad (3.20)$$

The distribution of χ^2 is dependent on the number of degrees of freedom, df, which is generally the number of constraints minus the number of parameters to be fitted. This is illustrated by figure 3.1. For $df > 2$ the distribution has a maximum point at $df - 2$. To have a comparable distribution for different degrees of freedom, the confidence level $P(\chi^2)$, can be defined by equation (3.21). The resulting distribution is ideally flat if all set parameter errors are correct. Failed fit results where the constraints could not be fulfilled can then be removed by a selection cut on the confidence level. Examples for χ^2, confidence level and pull distributions are shown in section 5.1.1 for the $\gamma p \rightarrow X \rightarrow \pi^0 p$ reaction.

$$P(\chi^2, df) = \frac{1}{\Gamma(df/2)} \int_{\chi^2/2}^{\infty} t^{df/2-1} e^{-t} dt \qquad (3.21)$$
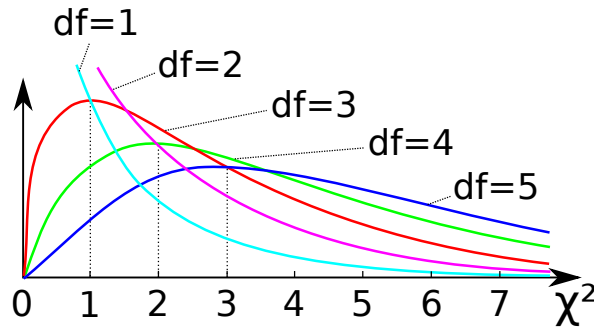
Figure 3.1: χ^2 distributions for different degree of freedom df. Each line represents a different degree of freedom.

3.2.2 Implementation

The kinematic fit was implemented in the ExPlORA framework. This framework combines C++ based plug-ins with an xml interface, allowing for a fast change without the need to recompile. Of course this only works if the C++ plug-ins are also written accordingly. The kinematic fit therefore needs to be easily configurable to the analysis requirements. A first version of a kinematic fit was implemented in the BGO-OD experiment with the name *BTKinematicFitter* during this thesis.

Parameter

For each particle, seven fit parameter are definable. The definition of these parameters differ in the direction and vertex fit mode of *BTKinematicFitter*. In equation (3.22) the fitting parameter for a particle *i* are shown.

$$
\begin{array}{cc}
\text{direction fit} & \text{vertex fit} \\
\begin{pmatrix}
\hat{P}^i_x \\
\hat{P}^i_y \\
\hat{P}^i_z \\
|\vec{P}^i| \\
V^i_x(unused) \\
V^i_y(unused) \\
V^i_z(unused)
\end{pmatrix}
&
\begin{pmatrix}
D^i_x \\
D^i_y \\
D^i_z \\
|\vec{P}^i| \\
V^i_x \\
V^i_y \\
V^i_z
\end{pmatrix}
\end{array}
\tag{3.22}
$$

During the direction fit, it is assumed that the reaction took place at the center of the target (0,0,0). The only remaining fitting parameters are then the particle direction unit vector $(\hat{P}^i_x, \hat{P}^i_y, \hat{P}^i_z)$ and the momentum $|\vec{P}^i|$. With the known particle mass m_i, the energy is determined from the momentum during the fit by $E_i = \sqrt{\vec{P}^{i^2} + m_i^2}$. In the vertex fit the fit parameters are detector position, D, vertex position, V, and momentum $|\vec{P}^i|$. The particle direction $\hat{P}_k$ is calculated by $(D_k - V_k)/|\vec{D} - \vec{V}|$. With this the vertex position is part of the momentum and energy definition. The four-momentum definitions are summarized in table 3.1.

Component	direction fit	vertex fit
P_x	$\hat{P}_x \cdot |\vec{P}|$	$\frac{(D_x - V_x)}{|\vec{D} - \vec{V}|} \cdot |\vec{P}|$
P_y	$\hat{P}_y \cdot |\vec{P}|$	$\frac{(D_y - V_y)}{|\vec{D} - \vec{V}|} \cdot |\vec{P}|$
P_z	$\hat{P}_z \cdot |\vec{P}|$	$\frac{(D_z - V_z)}{|\vec{D} - \vec{V}|} \cdot |\vec{P}|$
Energy	$\sqrt{\vec{P}^2 + m^2}$	$\sqrt{\vec{P}^2 + m^2}$

Table 3.1: 4-Momentum definitions for the kinematic fit

Kinematic constraints

The possible constraints for *BTKinematicFitter* are 4-momentum conservation, missing mass and invariant mass constraint. Single particle mass conservation is already fixed by the energy definition. The 4-momentum conservation constraints is defined by equation (3.23). The number of initial particles is $N1$, while the number of particles in the final-state is $N2$.

$$0 = \sum_i^{N1} E^i_{initial} - \sum_i^{N2} E^i_{final}$$

$$0 = \sum_i^{N1} \vec{P}^i_{initial} - \sum_i^{N2} \vec{P}^i_{final} \tag{3.23}$$

If a particle with known mass M_{miss} is missing, a missing mass constraint can be defined by equation (3.24):

$$0 = (\sum_i^{N1} E^i_{initial} - \sum_i^{N2} E^i_{final})^2 - (\sum_i^{N1} \vec{P}^i_{initial} - \sum_i^{N2} \vec{P}^i_{final})^2 - M^2_{miss} \tag{3.24}$$

Should N particles be a decay product of a particle with $M_{composed}$, a similar constraint can be added to the existing constraints with equation (3.25).

$$0 = (\sum_i^{N} E^i)^2 - (\sum_i^{N} \vec{P^i})^2 - M^2_{composed} \tag{3.25}$$

H(α_A) derivative

BT KinematicFitter uses numerical derivatives even though the function derivative can be easily calculated by hand and predefined in the code. The first reason for this is that a numerical derivative could be implemented faster. Secondly, the parameter definitions can be changed fast without the need to change their derivative. Additionally, errors due to the numerical derivative have no influence on the fit if the start value, α_A, is the expected value, which is achieved by multiple iterations.

Iterations

At the start, α_A is equal to the measured values α_0. After the kinematic fit calculation, the expected values α are used as α_A for the next iteration. Only with linear constraints and parameter definitions one can assume that the solution is found with only one iteration, due to the used approximations. *BT KinematicFitter* uses non linear parameters and constraint definitions, so one will approach the real expected value, α, only with multiple iterations. If the constraints are fulfilled the fitting procedure stops. In figure 3.2 an example distribution can be seen for the required number of iterations.

3.2.3 Example Reaction: $\gamma p \rightarrow K^+ \Sigma^0$

To demonstrate the *BT KinematicFitter*, identification of the $\gamma p \rightarrow K^+ \Sigma^0$ reactions is shown. The $K^+ \Sigma^0 \rightarrow K^+ \Lambda \gamma$ final-state decays with a branching ratio of $(63.9 \pm 0.5)\%$ into the $K^+ p \pi^- \gamma$ state. This final-state can be identified with the BGO-OD experiment.
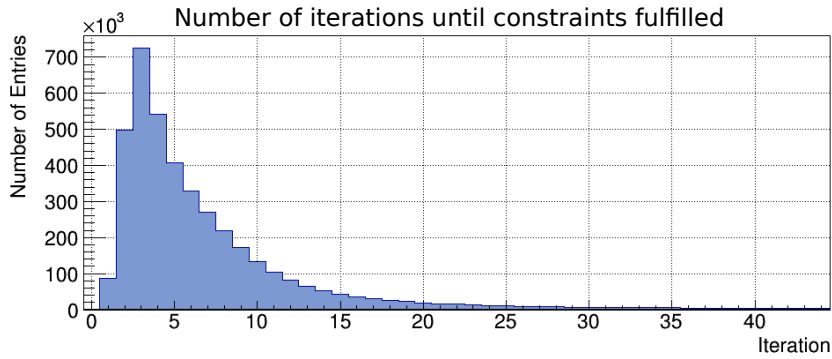
Figure 3.2: Number of iterations needed to find a solution where the result fulfills the set constraints below an allowed value.

Identification procedure

The identification procedure is explained in section 5.1.3 in more detail. The invariant mass of the $p\pi^-\gamma$ state for all combinations can be seen in the left of figure 3.3. A small peak at around 1190 MeV is visible, which is close to the expected Σ^0 mass of 1193 MeV.
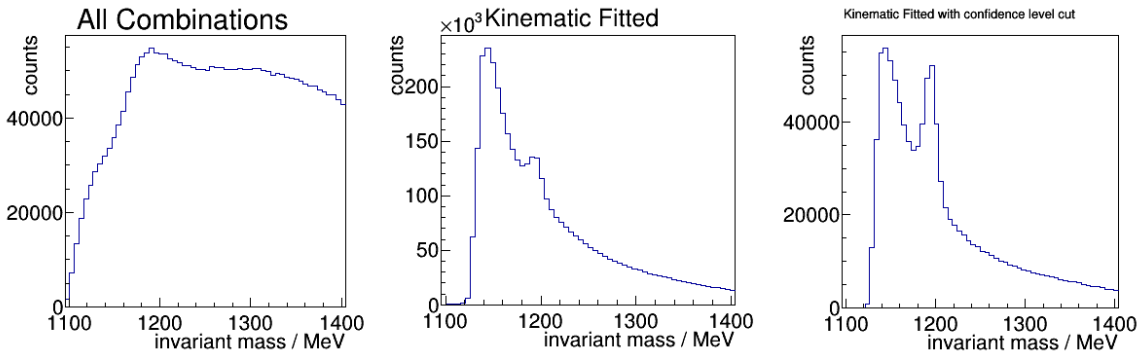

Figure 3.3: Invariant mass of the $p\pi^-\gamma$ state. Comparison between all combinations(left), after kinematic fit(middle) and kinematic fit results after confidence level cut of >1 % (right).

Kinematic fit influence

For the kinematic fit, the set constraints were four-momentum conservation and the $\Lambda \rightarrow p\pi^-$ invariant mass constraint, where the invariant mass of the p and π^- system is fixed to the Λ mass of 1116 MeV. This leads to a change in the background distribution, which starts at the Λ mass, peaks at 1150 MeV and falls of seemingly exponentially. Some of the kinematic fit results only fulfill the constraints if some particle parameters are changed by values bigger then the detector resolutions. These events are mostly combinatorical background that are removed by selecting fit results with a confidence level >1 %. In figure 3.4 the confidence level distribution can be seen. This distribution takes the degree of freedom into account to create a flat probability distribution. The rise on the left of the distribution are background events which only accidentally fulfill the constraints of the fit. The rise on the right shows

that the set parameter errors are too large. The invariant mass of selected events can be seen in the right figure 3.3. The Σ^0 peak is enhanced by suppression of the background distribution.
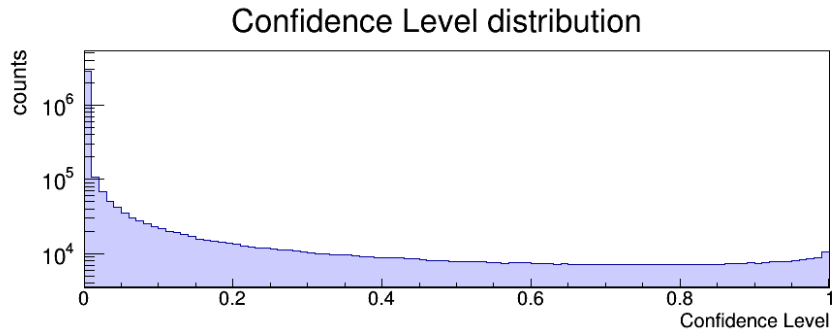
Figure 3.4: Confidence level distribution for $\gamma p \to K^+ \Sigma^0 \to K^+ \gamma \Lambda$.

Deviation from the approximations

The kinematic fit uses a lot of approximations to derive from the Lagrange multiplier a fitting algorithm which can be implemented in a program. One of these is the assumption of Gaussian error distribution mentioned in section 3.2.1. This assumption does not represent the error distributions in the Tagger or SciRi detector. The θ resolution of SciRi is limited to the size of one scintillator element of 5°, which is much bigger than the uncertainty from the target dimensions and multiple scattering. This results in a box shaped error distribution. The approximation with a Gaussian fuction does not account for this. An example of this can be seen in the invariant mass of the ω in the $\gamma p \to \omega p \to \pi^+ \pi^- \pi^0 p$ reaction, and was already seen in the PhD thesis of Oliver Freyermuth [30]. The identification is explained in more detail in section 5.1.2. In the kinematic fit the problem mainly arises because the meson and baryon angle resolution have different shapes. The meson θ error is Gaussian distributed, because it consists of multiple detected particles. As such, the θ direction of the meson is already known before the kinematic fit. After the kinematic fit the momentum conservation forces the agreement of the Gaussian(ω) and Non-Gaussian(proton) θ error distribution. In such cases the final θ direction is a convolution of both the omega and proton information. The workaround for this is to use the kinematic fit and ignore the θ information of the proton. This forces the kinematic fit to determine the θ direction from the other particles only, which results in Gaussian error distribution. In figure 3.5 the effect of a non-Gaussian error distribution is seen. The invariant mass of $\pi^0 \pi^+ \pi^-$ is shown with different simulated reactions. In this specific angular bin the effects are strongly visible showing the three SciRi rings as three separate peaks and the first crown of the BGO calorimeter in the invariant mass resulting in four peaks associated to the ω meson. The big gap in the invariant mass at around 790 MeV is the acceptance gap between BGO and SciRi. The fit on this distribution was performed with RooFit using simulated distributions (see section 3.3) which results in a successful fit due to the accurate simulated detector geometry. In figure 3.6 the kinematic fit was changed to reduce the influence of the proton on the θ direction. This removes the artificial structure of the ω mass distribution.

3.3 RooFit

RooFit [33] is used in this thesis to separate signal from background. RooFit is a toolkit for data modeling implemented in ROOT. The fit uses multiple probability functions to describe a given distribution. In this thesis, a Monte Carlo simulation of the experiment is used to determine the identification efficiency. The simulation uses accurate spatial, energy and time resolutions to provide results consistent with real data. This is used to determine the probability functions for RooFit. An example can be seen in figure 3.5 where the invariant mass distribution is strongly influenced by the detector geometry. The main requirement for a successful fit is a clear difference between the signal and background distribution. In figure 3.5 the $\pi^0\pi^-\pi^+ p$ and the $K^0\Sigma^+$ reactions show a similar distribution. In such cases the cross section can not be determined accurately for this final-states.
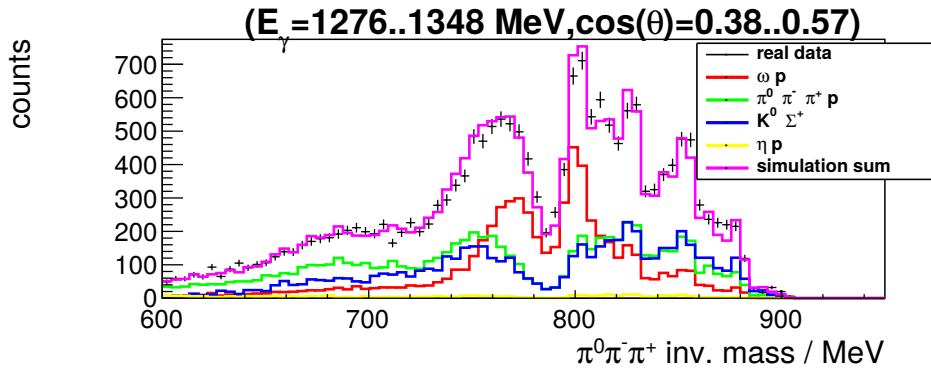
Figure 3.5: Invariant mass distribution of $\pi^0\pi^+\pi^-$ in the $\pi^0\pi^+\pi^- p$ final state with standard kinematic fit. Different colored lines show simulated contributions fitted to the real data in black.
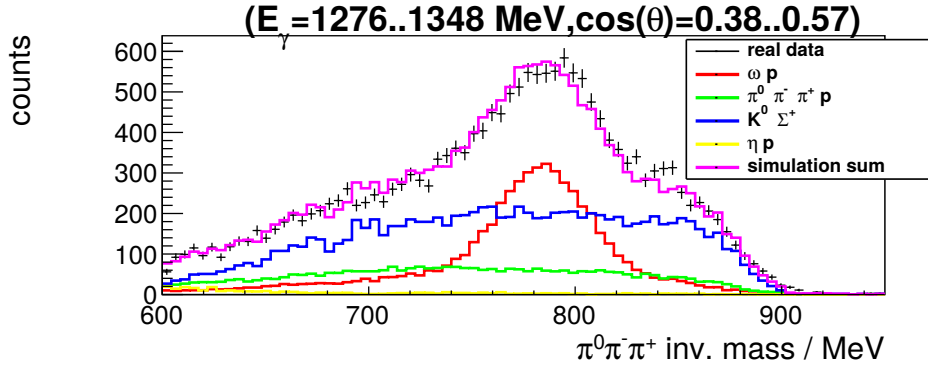
Figure 3.6: Invariant mass distribution of $\pi^0\pi^+\pi^-$ in the $\pi^0\pi^+\pi^- p$ final state with increased error on the proton θ direction in the kinematic fit. Different colored lines show simulated contributions of the real data in black. Removing the proton θ information from the fit removes the artificial structure in figure 3.5 and a ω peak is visible.

Techniques in cross section determination

Defined from classical scattering experiments, the cross section is the overlap area of the two colliding objects, which is proportional to the probability for a reaction to occur. By measuring the angular and energy dependence, the differential cross section, $d\sigma/d\Omega$, for a fixed target experiment is defined by the relation: [36],[37]

$$\frac{d\sigma}{d\Omega} = \frac{A}{F}\frac{dN_s}{d\Omega},$$
(4.1)

where F is the flux of incident particles, A is the target area density and $dN_s/d\Omega$ is the average number of reactions per solid angle $d\Omega$. The solid angle is defined as $\Omega = \int_{\phi^a}^{\phi^b}\int_{\theta^A}^{\theta^B} sin(\theta)d\theta d\phi$ with a/A and b/B as limits for ϕ/θ. With the assumption that the differential cross section is constant over a solid angle range, Ω, it is possible to write:

$$\frac{d\sigma}{d\Omega}(\Omega) = \frac{N_s \cdot A}{F \cdot \Omega},$$
(4.2)

which is a good approximation if Ω is small. The area density, A, is given by the target density n and the target cell length z. Due to detector acceptance and selection criteria, the detection efficiency of a given reaction is lower than 100 %. This efficiency η_{reco} is determined by the ratio of identified events using simulated data, N_{sim}, with the total number of generated reactions, N_{sim}^{total}. Using unpolarized beams and targets, cross sections are isotropically distributed in ϕ, so it is usual to integrate over all ϕ. Ω can be determined by $(cos(\theta_{cms}^B) - cos(\theta_{cms}^A)) \cdot 2\pi$, with the θ bin ranging from θ_{cms}^A to θ_{cms}^B. The cross section has then the form:

$$\frac{d\sigma}{d\Omega}(\Omega) = \frac{1}{F} \cdot A \cdot \frac{1}{\Omega} \cdot N_s$$
(4.3)

$$\frac{d\sigma}{d\Omega}(\theta) = \frac{1}{F} \cdot \frac{1}{n \cdot z} \cdot \frac{1}{(cos(\theta_{cms}^B) - cos(\theta_{cms}^A)) \cdot 2\pi} \cdot \frac{N}{\eta_{reco}}$$
(4.4)

The BGO-OD experiment uses a photon beam via bremsstrahlung, with the energy of single photons given as E_γ. The cross section, as a function of E_γ and θ can be written as:

$$\frac{d\sigma}{d\Omega}(E_\gamma, \theta) = \frac{1}{F(E_\gamma)} \cdot \frac{1}{n \cdot z} \cdot \frac{1}{(cos(\theta_{cms}^B) - cos(\theta_{cms}^A)) \cdot 2\pi} \cdot \frac{N(E_\gamma, \theta)}{\eta_{reco}(E_\gamma, \theta)}$$
(4.5)

To measure the differential cross section, the number of reaction events are divided in E_γ and θ bins. Additionally the target area density, A, incident particle flux, $F(E_\gamma)$, and detection efficiency, η_{reco}, need to be determined. The target area density, A, is determined in section 4.1 and the photon flux, $F(E_\gamma)$, in section 4.2. The detection efficiency, η_{reco}, of a reaction depends on the particle kinematics, thus no generalized statement can be made here. For each given reaction, η_{reco} is simulated with the known detector geometry and efficiency. In section 4.3 the detector efficiency for protons is determined from the $\gamma p \to \pi^0 p$ and $\gamma p \to \eta p$ reactions. The data acquisition does not save every occurring detector signal. Only events which fulfill the set trigger conditions are saved. These trigger conditions influence the detection efficiency, η_{reco} and are explained in more detail in section 4.4. After determining these individual parameters, the cross section can be determined with the detected event number $N(E_\gamma, \theta)$. The cross section is determined for some example reactions in chapter 5.

material	Atomic Mass A	Charge Z	density (kg/m^3)
hydrogen (liquid)	1.007	1	70.85
hydrogen (gas)	1.007	1	0.08988
deuterium (liquid)	2.014	1	169
deuterium (gas)	2.014	1	0.1680
carbon	12.017	6	2620
air	14.683	7.32	1.204
Mylar foil	12.886	6.46	1370

Table 4.1: Relevant materials for a BGO-OD target with their mass and density.

material	nucleus density $(1/m^3)$	proton density $(1/(\mu barn \cdot cm))$	neutron density $(1/(\mu barn \cdot cm))$
hydrogen (liquid)	4.237×10^{28}	4.237×10^{-8}	0
hydrogen (gas)	5.375×10^{25}	5.375×10^{-11}	0
deuterium (liquid)	5.053×10^{28}	5.053×10^{-8}	5.053×10^{-8}
deuterium (gas)	5.025×10^{25}	5.025×10^{-11}	5.025×10^{-11}
carbon	1.313×10^{29}	7.878×10^{-7}	7.878×10^{-7}
air	4.938×10^{25}	3.615×10^{-10}	3.634×10^{-10}
Mylar foil	6.403×10^{28}	4.136×10^{-7}	4.111×10^{-7}

Table 4.2: Relevant materials for a BGO-OD target with the density recalculated into proton/neutron density for the cross section calculation.

4.1 Target area density determination

The target size and composition must be known to determine the area density, A. The target cell, shown in section 2.2.2, is enclosed with a foil to reduce interactions with the photon beam. Due to the pressure difference in the target cell and vacuum in the beam pipe, the foil expands and therefore the target volume. The effective target length, z, is 6.1 cm for the 5 cm cell and 11.1 cm for the 10 cm cell. Due to the uncertainty on the curvature of the target windows the target length has an assumed uncertainty of up to 1 mm. Table 4.1 and 4.2 shows the density n for different materials [3],[38]. The

given density for liquid hydrogen and deuterium is at 18 K. The composition of air is assumed to be 78 %N, 21 %O and 1 %Ar. Mylar is a manufacturer for foil made of polyethylene terephthalate, which consists of 63 %C, 33 %O and 4 %H. Using this, it can be determine that $n \cdot z = A$ for liquid hydrogen is $(2.58 \pm 0.04) \times 10^{-7} \, \mu b^{-1}$ for running periods before January 2018 and $(4.70 \pm 0.04) \times 10^{-7} \, \mu b^{-1}$ after that. The influence of the Mylar windows on the cross section can be measured by taking data using an empty target cell.
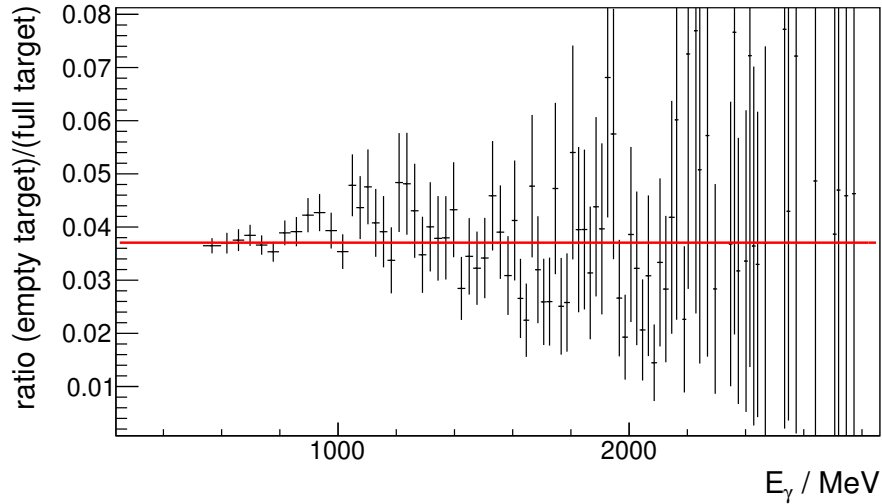
Figure 4.1: Ratio between normalized counts (N/F) with empty target and full target from the $\pi^0 p$ reaction against incoming photon energy E_γ for the April 2017 running period. The red line marks the average value.

Using the densities from table 4.2 one can estimate that for the 5 cm cell around 3.7 % of the measured reactions will occur in the Mylar foil. To check this for the $\gamma p \to \pi^0 p$ reaction, data with an empty target cell can be used to determine the ratio with the full target. The reaction identification is described into more detail in section 5.1.1. The identified events, N, from the $\pi^0 p$ reaction were normalized by the corresponding flux, F, for the empty target and full target. The ratio between the empty and full target for the April 2017 running period can be seen in figure 4.1. The red line marks the average value of (3.70 ± 0.01) %, which agrees to the estimated 3.7 % from the density values for the 5 cm target cell.

4.2 Photon flux determination

In this section the photon flux determination is described. For the BGO-OD experiment, the Tagger detector counts the number of post-bremsstrahlung electrons from which the photon number can be derived. Due to the collimation of the photon beam, not all photons reach the target. The flux monitors GIM and FluMo, which are located at the end of the experiment, are used to measure the photon flux at the target cell. The probability of a bremsstrahlung photon to reach the target is called the tagging efficiency, $P_\gamma(E)$, and is the main focus of this chapter.

The complete overview of the photon beam line at the BGO-OD experiment can be seen in figure 4.2. The photons are produced via bremsstrahlung in the radiator. The initial photon number at the radiator is determined by counting the post bremsstrahlung electrons with the Tagger hodoscope
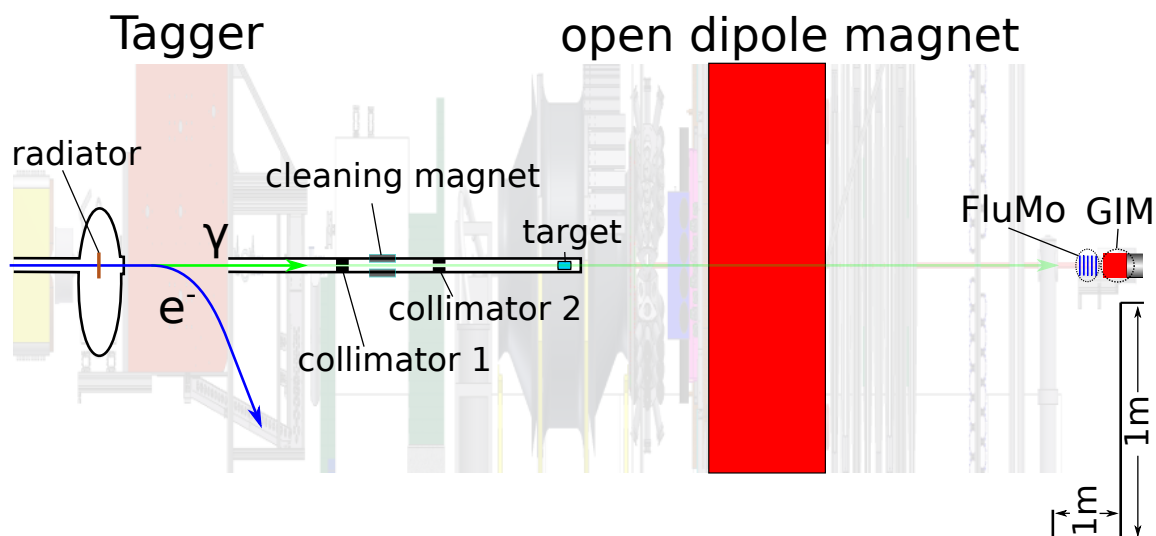
Figure 4.2: Side view over the BGO-OD experiment scaled asymmetrically. The important components to determine the photon flux are highlighted. Compare with figure 2.2 for better orientation.

(described in section 4.2.1). The photon beam passes through a collimator before it hits the target. This is cylindrically shaped with a small hole in the middle, and is made off lead. The collimator fills the beam pipe completely effectively reducing the beam pipe diameter to the small hole of the collimator. The first collimator had a diameter of 3 mm during June and October 2015 running period and was changed to 7 mm for the April and February 2017 running period. After the first collimator, the sweeping magnet removes these charged particles which were produced in the material of the first collimator and could not be stopped. To remove the higher-momentum particles, which may not be deflected enough by the magnet, a second collimator is used. This collimator has a diameter of 12 mm and can thus only stop secondary particles produced by the first collimator. The now collimated photon beam enters the target cell. Photons which did not interact with the target will leave the vacuum beam pipe and move through the forward spectrometer to the end of the experiment, where two monitoring detectors, FluMo and GIM, are positioned. These detectors are used together with the Tagger to determine the tagging efficiency, $P_\gamma(E)$. The GIM has a high efficiency for photon detection but is limited by its detection dead time and cannot be used during data taking. The FluMo detector was constructed to overcome this problem by measuring only a fraction of the total photon rate. In section 4.2.2 the GIM detector and in section 4.2.3 the FluMo are described in detail. $P_\gamma(E)$ depends on the photon beam position and any fluctuation in the ELSA electron beam. As such, it is important to monitor this value constantly to determine the photon flux at the target position. In section 4.2.4 the photon flux is determined for the April 2017 running period.

4.2.1 Tagger

The Tagger is used to detect the post-bremsstrahlung electrons and was described in chapter 2.2.1. This section focuses on the components important for the photon flux determination.

The Tagger scintillators, shown in figure 4.3, have an overlap of around 55 % with each other, ensuring
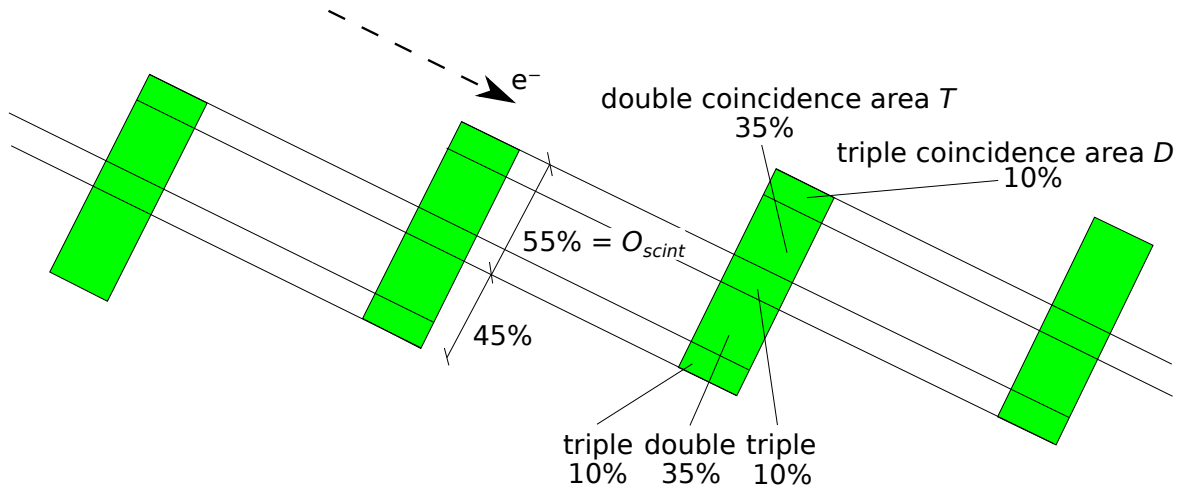
Figure 4.3: Four scintillators of the horizontal part of the Tagger. The green rectangle represent the scintillators. An electron indicated by the dashed line moves perpendicular to the scintillators and crosses two or three scintillators. The area of overlap is given in percent of the complete scintillator area.

an electron always passes through at least two scintillators. A Tagger signal is therefore defined by a coincidence of at least two neighboring channels. The 55 % overlap between two scintillators occasionally gives a coincidence among three scintillators. The probability for that to happen is 30 % as indicated by the marked areas in the figure. The real overlap may deviate from the expected geometry, due to the manufacturing process, which is described in section 4.2.1.

For data acquisition, the Tagger uses a VFB6 FPGA[1] board. This board has the jTagger firmware, implementing a combination of TDC, trigger logic and scaler counter. The TDC acquires the single channel data. These signals are contaminated with noise coming from the photomultiplier or δ electrons, which can be removed by building a coincidence of at least two scintillators. Due to the limitation of the FPGA size, only a double-coincidence logic is implemented. This means that every time a triple coincidence takes place two double-coincidence signals are registered. Every electron which passes through three scintillators will therefore add two counts. This double counting of electrons needs to be corrected during the data analysis. To correct this the TDC data is used to simulate the coincidence logic of the VME-Board. This is called scaler-logic clustering, *sln*, and like the FPGA logic, this produces too many hits. With the normal clustering, *nc*, of the Tagger hit where this double counting is not present, one can determine the ratio $R_{nc/sln}$ between normal clustering and scaler-logic clustering. With this ratio it is possible to correct the scaler information of the Tagger and get the real number of post-bremsstrahlung electrons. The process to determine the ratio is described in the next section.

Determination of Tagger scintillator overlap ratio $R_{nc/sln}$

The TDC data time distribution relative to the event trigger is shown in figure 4.4. The time range window of the TDC is around $1.2\,\mu$s. Only events fulfilling the pre-defined trigger conditions, shown in section 4.4, are acquired. The Tagger is part of the trigger, so a clear correlation to the trigger time zero can be seen as a peak. To estimate the rate of the electrons, the region around the peak cannot be

---

[1] Field-Programmable Gate Array
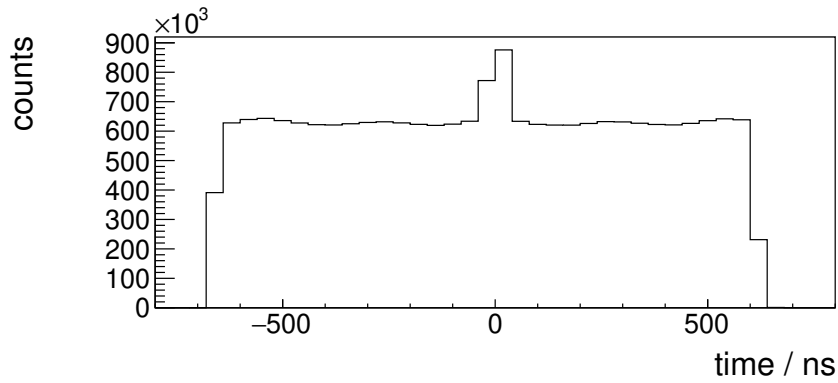
Figure 4.4: Time distribution of the Tagger TDC data. A prompt peak for the trigger attempt at 0 ns is visible on top of a continuum. The continuum is limited by the TDC time window for acquisition.

used due to the correlation to the trigger. Instead the events in the time region $-400\,\text{ns}$ to $-200\,\text{ns}$ and $200\,\text{ns}$ to $400\,\text{ns}$ are used to determine the rate. The result of this can be seen in figure 4.5. Comparing the different methods to determine the rate in the Tagger, it is clear that the Tagger scaler counts too many events, however the scaler rate agrees to the scaler-like clustering from the TDC data. The scaler counts the electrons non-stop, while the TDC only counts over a small window around the triggered event. For the TDC data it is assumed that the electrons are equally distributed over time, however this only applies to a stable and continuous electron beam. In reality the beam has current fluctuations, especially at the beginning and end of the extraction spill of ELSA . The probability to have a triggered event during the high current period is higher than during the low current period of the beam, which means more of the TDC data was taken during the higher current periods of the beam, leading to a rate higher than the actual average rate. The scaler counter is therefore vital for accurate photon flux determination.
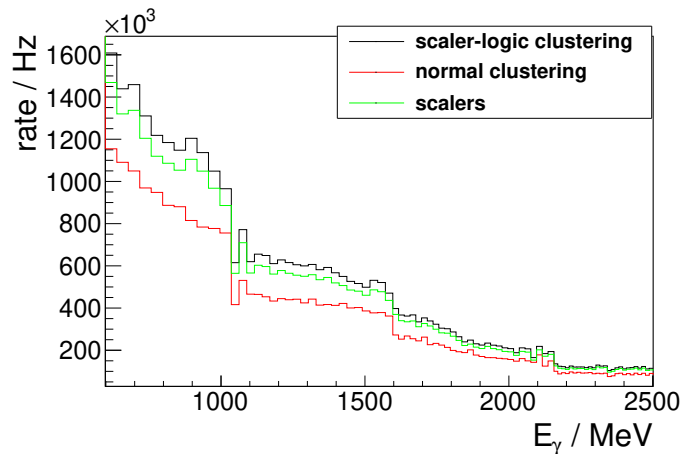
Figure 4.5: Tagger intensity distribution against initial photon energy. The rate determined from TDC data is marked with red for the normal clustering of hits, and in black for the recreation of the scaler-like clustering. In green the rate determined using the electronic scaler counter of the Tagger is plotted. The Tagger uses five different scintillator sizes to cover the acceptance which is visible as different bin widths in the distribution.

The determined TDC rates for the normal clustering, *nc*, and scaler logic clustering, *sln*, methods are divided to determine the $R_{nc/sln}$ ratio. The results for real data and simulation can be seen in figure 4.6. The fluctuations between the bins shows that the scintillators do not have a constant overlap to each other. The simulated Tagger geometry, however, agrees well to the actual Tagger construction.
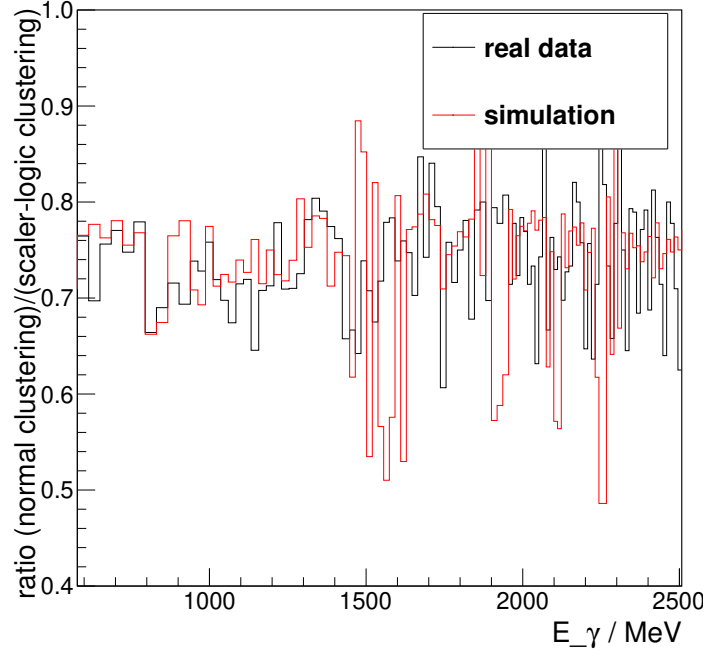
Figure 4.6: Ratio $R_{nc/sln}$ between normal clustering(2 or 3 scintillators) and scaler-logic clustering(2 scintillators) against initial photon energy. Simulated and real data in red and black respectively. The ratio is a direct result of the detector geometry.

From the geometry shown in figure 4.3, one can find the following relation for the ratio $R_{nc/sln}$ and the scintillator overlap O_{scint}:

$$\text{Area for Triple coincidence} = T \quad = \quad 2 \cdot O_{scint} - 1 \tag{4.6}$$

$$\text{Area for Double coincidence} = D \quad = \quad 2 - 3 \cdot O_{scint} \tag{4.7}$$

$$R_{nc/sln} = \frac{T + D}{2 \cdot T + D} \quad = \quad \frac{1 - O_{scint}}{O_{scint}} \tag{4.8}$$

$$\Rightarrow O_{scint} \quad = \quad \frac{1}{1 + R_{nc/sln}} \tag{4.9}$$

T, D and O_{scint} are shown in figure 4.3. This relations are only defined for $0.\bar{6} > O_{scint} > 0.5$ and if electrons move perpendicular to the scintillators. For O_{scint} greater than $0.\bar{6}$, double coincidences are replaced by quadruple coincidences. If O_{scint} is smaller 0.5 no triple coincidence can take place. The average ratio of $R_{nc/sln} = 0.75$ in figure 4.3 translates to an average scintillator overlap of around 57 %, which is a little higher than the stated overlap. By using this distribution we can correct the scaler counts and determine the number of bremsstrahlung electrons per energy bin.

4.2.2 GIM

The detection of photons at the very end of the experiment is used to determine the tagging efficiency, P_γ. Any produced bremsstrahlung photon is indirectly counted by the Tagger via bremsstrahlung electron detection. Some of the photons are stopped by the collimators. To determine how many photons could potentially interact with the target, a coincidence logic is used during the data analysis between the Tagger and the flux monitors, GIM and FluMo. The GIM (described in section 2.2.6) is located at the end of the experiment and is used to detect photons. Due to the single PMT readout, the detector cannot handle the high rate of the photon beam. The dead time of the PMT reduces the detection efficiency. The GIM can therefore only be used for short periods with low-intensity beams. The tagging efficiency P_γ(E), can be determined with TDC data by building a coincidence between the Tagger and GIM (Tagger(E)∧GIM). The Tagger assigns an energy to the photons detected by GIM at the end of the experiment. The P_γ(E) is then the ratio between all bremsstrahlung electrons (Tagger(E)) and photons at the end of experiment (Tagger(E)∧GIM):

$$P_\gamma(\text{E}) = \frac{\text{Tagger(E)} \wedge \text{GIM}}{\text{Tagger(E)}} \tag{4.10}$$

P_γ determined with the GIM and Tagger can be seen in figure 4.7. P_γ has a value of about 80 %. The photon beam collimator is the main cause for the reduction in P_γ, which in this case stops 20 % of the photons. The small increase in P_γ for energies between 1400 MeV to 1800 MeV originates from polarized coherent bremsstrahlung, due to a crystalline radiator being used. The bremsstrahlung distribution differs from an amorphous radiator as illustrated in figure 4.8. The coherent photon beam is more narrowly distributed compared to the incoherent beam. Fewer photons are stopped by the collimator and P_γ is increased. The decrease in P_γ at high photon energy is not fully understood. It appears that the Tagger counts too many electrons in that energy region, which deviates from the expected $1/E_\gamma$ bremsstrahlung relation. These low energetic electrons seem to be present in the ELSA electron beam before the interaction with the radiator, as they do not disappear by removing the radiator.
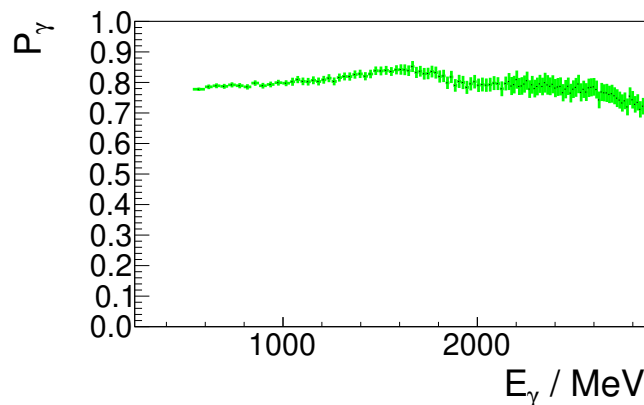
Figure 4.7: P_γ against photon energy using the GIM detector for a single data taking run (6 min).

P_γ measurements for different running periods are shown in figures 4.9. The run number can be interpreted as progress in time. Between the November/October 2015 and the April 2017 running period, the 3 mm diameter collimator was replaced by a 7 mm diameter collimator. This changed the
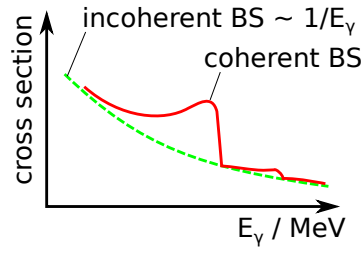
Figure 4.8: Bremsstrahlung spectrum for an crystalline radiator. The green line shows the incoherent bremsstrahlung present for all materials. In a crystalline radiator bremsstrahlung can also occur coherent resulting in a total distribution shown by the red line.

average P_γ from 22 % to 75 %. The photon beam has a σ width of around 3 mm at the collimator position. Thus the 3 mm diameter collimator removes a large portion of the beam. The P_γ results fluctuate due to the ELSA electron beam position, which is not stable.

The GIM is only used for short periods each day and at low intensities for the following reasons. The lead glass of the GIM is not radiation hard. During data taking the lead glass would turn brown after a couple days and absorb the produced light before it can reach the photomultiplier. A second problem with this detector is the rate instabilities. The highest rate on one Tagger scintillator is around 4 MHz. Additionally all electrons with energy lower than 10 % of the ELSA energy do not hit the Tagger hodoscope. The GIM however detects all bremsstrahlung photons and has only one photo multiplier, resulting in too high event rates for the data acquisition. The GIM can be moved into and out of the beam. To determine $P_\gamma(E)$ using the GIM, the ELSA current is reduced and the GIM is moved into the beam. Due to this time-consuming process, the $P_\gamma(E)$ measurement with GIM was only performed once every day. For monitoring during data taking the FluMo is used, which is located in front of the GIM.

4.2.3 FluMo

The FluMo (cf. 2.2.6) consists of five thin plastic scintillators with photomultiplier readouts. Photons leave the vacuum pipe after the target and pass through the varying detector elements, where in any part conversion may take place. However only a small portion of the photons interact, so the rate at the FluMo is much lower compared to GIM. Also the use of five detectors allows coincidences, which are useful to remove noise, and increase detection efficiency as only two out of five are needed to identify an event. Additionally, the detector energy resolution is sufficient to distinguish the number of charged particles in a hit. The electron-position pairs can be clearly distinguished from single-charged particles, as the signal is twice as large.

To use the FluMo for $P_\gamma(E)$, determination one first needs to find out the probability of photon conversion to electron-position pairs. This is called the **photon efficiency** and is used to determine the number of bremsstrahlung photons at the end of the experiment. The **photon efficiency** is the convolution of the FluMo detector efficiency and the pair production cross section. The master's thesis of Katrin Kohl [29] gives more details of the procedure. To determine the efficiency we use the GIM detector:

$$\text{Photon efficiency}(E) = \frac{\text{Tagger(E)} \wedge \text{Flumo} \wedge \text{GIM}}{\text{Tagger(E)} \wedge \text{GIM}} \qquad (4.11)$$

(a) June/July 2015, 3 mm collimator

(b) November/October 2015, 3 mm collimator

(c) April 2017, 7 mm collimator

(d) June/July 2018, 7 mm collimator
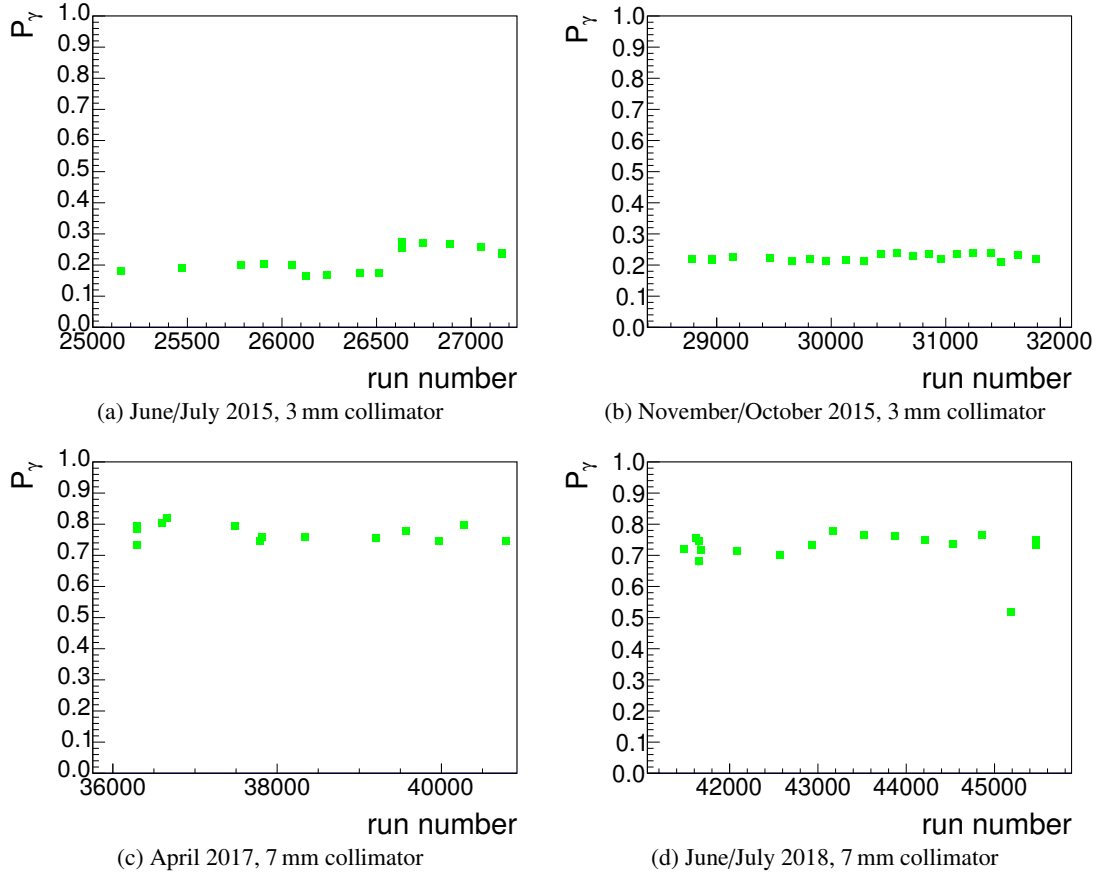
Figure 4.9: P_γ average using the GIM detector for different runs and running periods. Fluctuations in P_γ during a running period are due to a change of electron beam position.

Every coincident detector hit in both the Tagger and GIM should also produce a hit in FluMo. The photon pair production cross section σ_{pair} can be calculated [37]:

$$\sigma_{pair} = 4 \cdot Z^2 \alpha r_e^2 \cdot \left[\frac{7}{9} \left(\ln \left(\frac{2h\nu}{m_e c^2} \right) - f(Z) \right) - \frac{109}{54} \right] \tag{4.12}$$

with r_e and m_e as classical radius and mass of electron, α the fine-structure constant and Z the nucleus charge. We can approximate this equation to:

$$\sigma_{pair} \approx A \cdot \ln(E_\gamma) + B, \quad A = \frac{28}{9} Z^2 \alpha r_e^2, \quad B = 4Z^2 \alpha \, r_e^2 \left[\frac{7}{9} \left(\ln(\frac{2}{m_e c^2}) - f(Z) \right) - \frac{109}{54} \right] \tag{4.13}$$

with $h\nu = E_\gamma$, where E_γ is the initial photon energy. A and B will be constant if Z is constant. In the figure 4.10 the pair production cross section formula is fitted to the determined **photon efficiency** with A and B as variable parameters. The fit function describes the data well, confirming that the FluMo detector detects electron-positron pair production. The absolute cross section itself cannot be determined as the conversion material thickness and density is complex and cannot be easily simulated.

FluMo is used to determine $P_\gamma(E)$ during the data taking. The TDC is readout if an event trigger occurs.
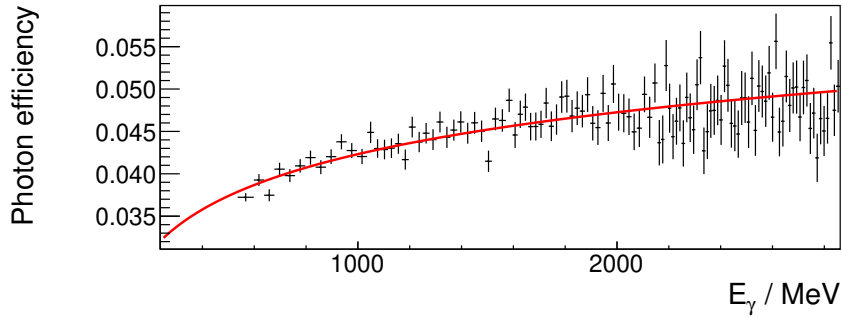
Figure 4.10: FluMo **photon efficiency** against photon energy. The FluMo detects events with two charged particles at the same time. The red line is a fit of $A \cdot \ln(E_\gamma) + B$, which correctly satisfies the pair production cross section.

This happens when the bremsstrahlung photon interacts with the target, so that no electron-position pair is detected in FluMo. Similarly to the Tagger TDC selection for rate determination, events are selected outside of the triggered events with the same time selection cuts as for the Tagger. By using the known FluMo **photon efficiency** and building the coincidence between Tagger and FluMo, the $P_\gamma(E)$ can be determined:

$$P_\gamma(E) = \frac{1}{\text{Photon efficiency}(E)} \cdot \frac{\text{Tagger}(E) \wedge \text{FluMo}}{\text{Tagger}(E)} \qquad (4.14)$$

(a) single data taking run ($\approx$6 min)

(b) full running period ($\approx$22000 min)
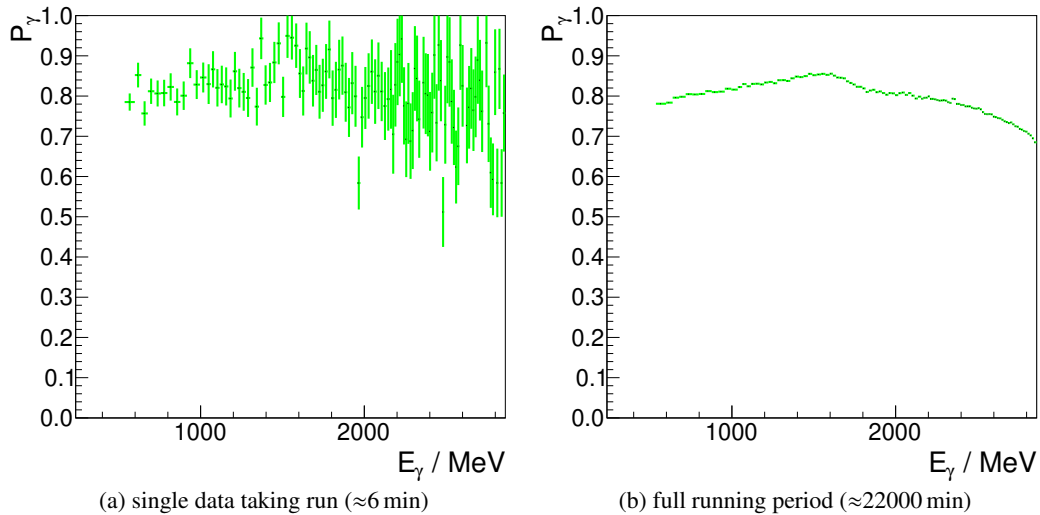
Figure 4.11: P_γ against photon energy using the FluMo detector.

Figure 4.11(a) shows the determined P_γ using the FluMo detector and compared to the results with GIM. The statistical error is larger for Flumo compared to GIM. This is due to the lower photon detection efficiency of around 4 % compared to almost 100 % of the GIM detector. P_γ from FluMo however is measured in parallel to the normal data taking, which is more practical for P_γ measurements

than using the GIM. In figure 4.11(b) P_γ was determined for the complete running period of April 2017, which shows the average P_γ during the data taking. In either case, FluMo tracks the flux admirably well.

4.2.4 Determination of the April 2017 running period photon flux

With the known number of bremsstrahlung electrons and $P_\gamma(E)$, the photon flux can be determined by multiplying them both together. Figure 4.12 shows the necessary steps to achieve this. First the bremsstrahlung electrons are counted using the Tagger scaler electronics. This is shown by the black points in the plot. This is too high due to the double counting in the Tagger scaler electronics (section 4.2.1). By multiplying this with figure 4.6, the correct number of electrons registered by the Tagger can be determined, which is shown by the red points. Not every bremsstrahlung photon reaches the target cell due to collimation. For this, the P_γ measurement with GIM or FluMo is needed. The green points are the product of P_γ measured with GIM with the corrected Tagger hits (red points). Similarly, the blue points use the FluMo P_γ. Both P_γ measurements agree with each other and thus the photon flux distributions are equal.
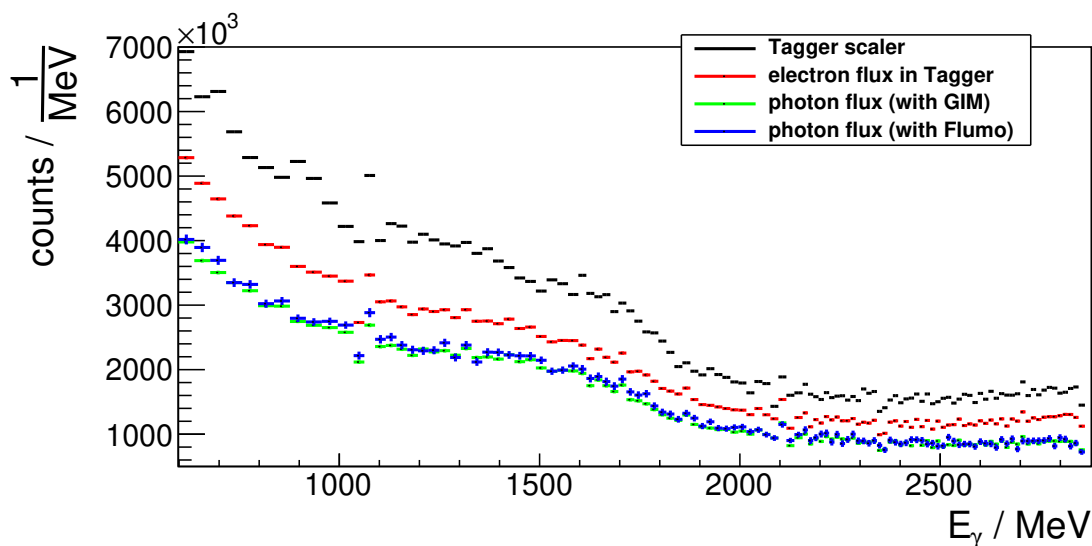
Figure 4.12: Normalized flux distribution. The individual bin content divided by the bin width against photon energy. The black points mark the counted coincidences in the Tagger during data taking. These are corrected and result in the electron number marked by the red points. Multiplied by P_γ from GIM results in the green points, while multiplied with P_γ from Flumo results in the blue points. After normalization, a $1/E_\gamma$ distribution is expected from the bremsstrahlung cross section. Due to coherent bremsstrahlung, a peak at $1700\,\text{MeV}$ is visible. Deviation from the expected distribution, as seen at $1050\,\text{MeV}$, means that the used bin width does not correspond the Tagger scintillator size.

If only the Tagger is used to determine the photon number, the high energy photon distributions show a deviation from the expected bremsstrahlung cross section as it increases with energy. This can be better seen in figure 4.13, where only the highest energy photon distribution is shown for different methods of photon flux determination. Before the inclusion of P_γ (red and black line), the number of photons increase with energy. After including the determined P_γ (green line), the photon number

starts to drop as like expected, showing the importance of measuring the energy dependence of P_γ. The most probable explanation for the rise in counts for higher energies, are low energetic electrons in the electron beam of ELSA . These are probably produced by the scattering of the main electron beam with the beam pipe walls.
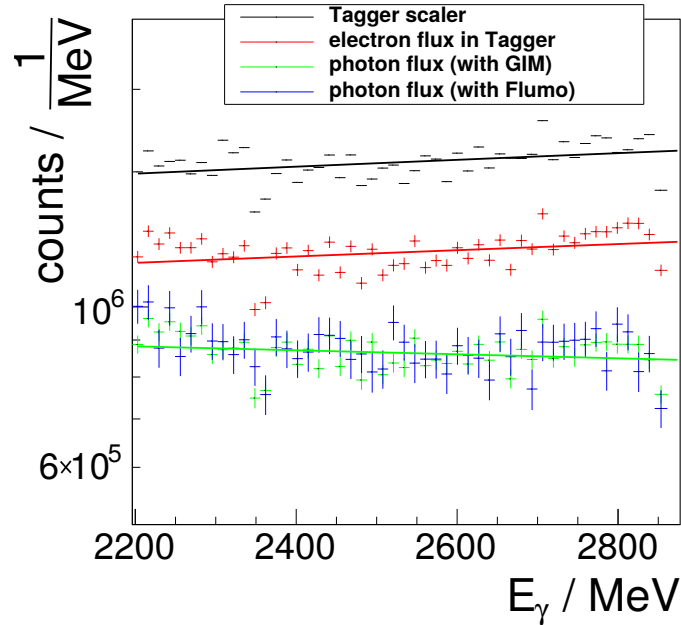
Figure 4.13: Same as figure 4.12, but zoomed in the high energy region. A first degree polynomial function was fitted to the data.

4.3 Verifying the proton detection efficiency

In the previous sections the target density and photon flux were determined for cross section measurements. The detection efficiency is also required for accurate determinations of cross sections. This efficiency depends on the geometry and detection efficiencies of all involved detectors, and is calculated using a Monte-Carlo simulation. The identification efficiency is separated in this thesis into two section: The simulated detection efficiency of hadronic reactions in this section, and the simulation of the triggering system of the data acquisition in section 4.4.

The GEANT4 [31] Monte Carlo simulation is used to determine the deposited energy inside the active detector material. From this energy, the detector response is emulated. After this the identification of the reaction follows the exact same steps as with real data. The geometry and efficiency of the detectors in the simulation must closely represent the reality. In this chapter, the proton detection efficiency is determined by using the $\gamma p \rightarrow Xp \rightarrow \gamma\gamma p$ photoproduction. The meson, X, can be either a π^0 or an η, as both decay into $\gamma\gamma$. After the meson identification, the direction of the proton, p, can be determined. On the event that a detected particle can be found with the same direction as the reconstructed direction, the proton is counted as detected. With this, the detection efficiency for the proton is determined. In this thesis it is assumed that other charged particles have a similar detection efficiency. The goal is to establish the agreement of real data and simulation. The reaction identification is described in section

(a) just BGO calorimeter

(b) no associated Barrel signal
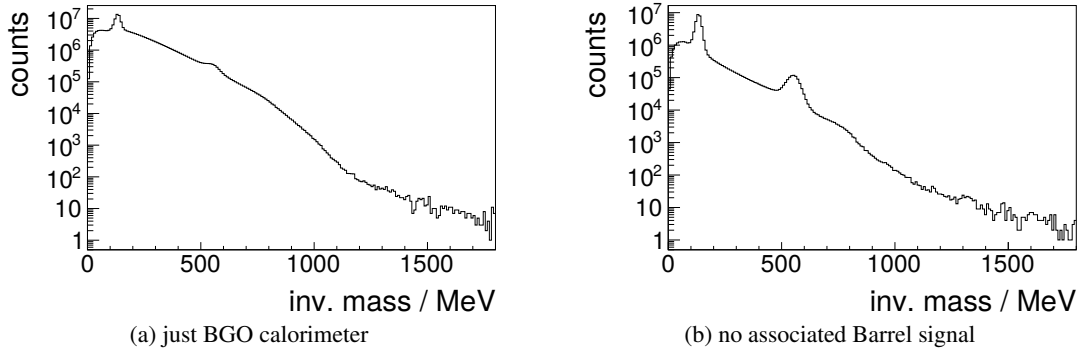
Figure 4.14: Invariant mass of two hits, assumed to be photons, in the BGO calorimeter. Two mesons the π^0 at 135 MeV and η at 550 MeV can be seen. The peaks in (a) are enhanced by additionally using the Barrel detector information in (b).

4.3.1 $\gamma p \rightarrow X p \rightarrow \gamma \gamma p$ identification
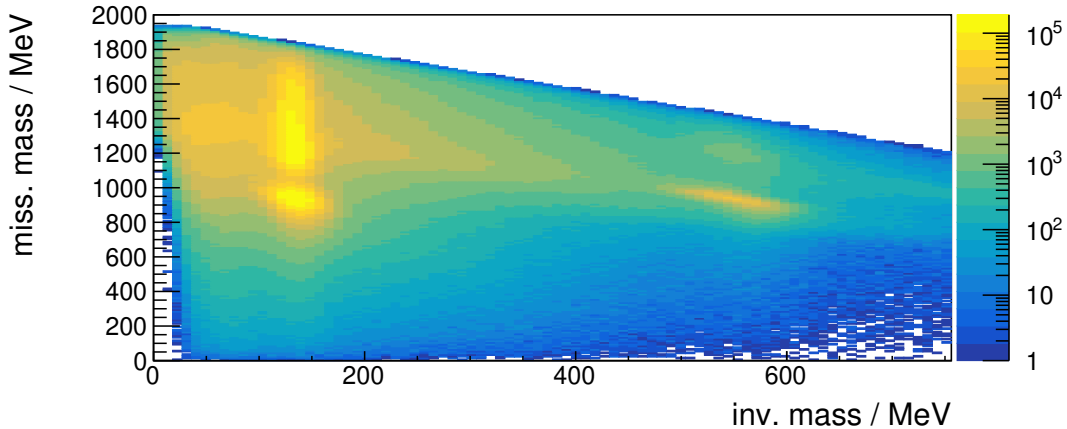
Figure 4.15: Missing mass against the invariant mass of a two-photon system. The colors show an intensity distribution. For missing mass of proton the π^0 and η are visible. Higher missing mass than 938 MeV means that the $\gamma \gamma$ meson has more particles in the final-state. The distribution stops on a diagonal line marking the kinetic limits.

To determine the proton detection efficiency, first the $\gamma p \rightarrow X p \rightarrow \gamma \gamma p$ reaction is identified initially by ignoring the final-state proton. For this, the initial and final-state photon momenta must be measured. The initial photon energy is measured by the Tagger detector, while the final-state photons are detected with the BGO calorimeter. With this the final-state proton momentum can be determined using four-momentum conservation. The $\gamma \gamma$ final-state mostly originates from a π^0 or η meson decay as seen in figure 4.14(a) where the invariant mass of the two photons is shown. A peak can be seen at the π^0 mass of 135 MeV and a smaller peak at the η mass of 550 MeV. The Barrel detector can be used to reduce the background contribution. The thin scintillator in front the BGO calorimeter
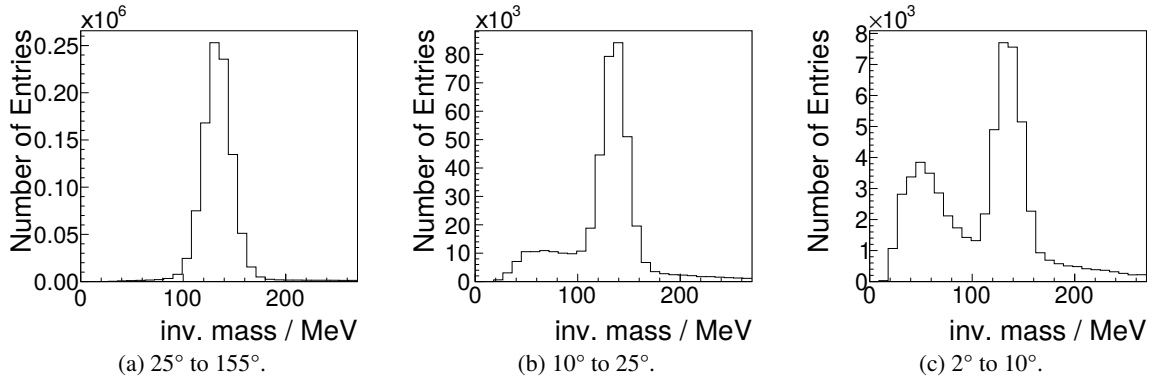
Figure 4.16: Invariant mass of $\gamma\gamma$ in the $\gamma p \to \pi^0 p$ reaction with different missing proton θ directions. The peak correspond to identified π^0 mesons. The background under the peak depends on the missing proton direction. The plots are divided in different detector regions with (a) for the BGO calorimeter, (b) for SciRi and (c) for the forward spectrometer.

has almost no response to photons, therefore both detected clusters in the BGO should not have any corresponding Barrel hit. In such cases the invariant mass of figure 4.14(a) changes to figure 4.14(b). Using the initial photon measured by the Tagger detector and assuming a target proton at rest, the missing mass to the two photon system can be determined. The missing mass to $\gamma\gamma$ against invariant mass of $\gamma\gamma$ is plotted in figure 4.15. A peak at the invariant mass of 135 MeV and missing mass of 938 MeV is visible. These are events from the $\pi^0 p$ reaction. Similarly the ηp reaction can be identified. Events with a $\gamma\gamma$ invariant mass consistent with a π^0 show in the missing mass, not only a peak for the proton but also a more wider distribution for higher missing mass. These events are from reactions like $\gamma p \to \pi^0\pi^0 p$, $\gamma p \to \Delta^0\pi^+$, and other reaction with a π^0 in the final-state. When selecting events the missing mass is in the range between 880 MeV to 1020 MeV the wrong reactions with π^0 or η are mostly removed. Figures 4.16 and 4.17 show the invariant mass depending on the missing proton direction. In figure 4.16 the π^0 peak can be identified, while figure 4.17 shows an η peak. The plots are divided depending on the expected proton direction. The background below the π^0 peak is almost non-existent for large proton angles and increases for smaller proton angles, whereas the background under the η meson mass peak increases with larger proton angles. Using the detection of both $\gamma p \to \pi^0 p$ and ηp to determine the proton detection efficiency allows for systematic checks.

4.3.2 proton detection efficiency

In the previous section, the π^0 are selected with an invariant mass between 109 MeV to 162 MeV, which corresponds to almost a 2σ cut. A larger acceptance would lead to smaller signal to noise ratio. The η events are selected in the mass region between 500 MeV to 600 MeV. Both the $\pi^0 p$ and the ηp final-states are used for the proton detection efficiency. From the identified meson and the initial state, the missing proton four-momentum can be determined. This predicted proton direction is compared to the remaining detected particles not associated with the meson. The angle difference between the predicted and detected proton can be seen in figures 4.18, 4.19, 4.20 and 4.21. The width of the angle difference depends on the angular resolution of the detected meson and proton. Thus, the width of the distributions depend on the identified meson momentum and can be seen by comparing figure 4.19 and 4.21. The ϕ difference width in figure 4.21 is in the order of 20°, which means the angular dependence of the efficiency cannot resolve specific geometrical effects and small gaps in acceptance. Events with a detected proton with a θ difference between $-10°$ to $10°$ and ϕ difference from $-50°$ to

(a) 25° to 155°. (b) 10° to 25°. (c) 2° to 10°.
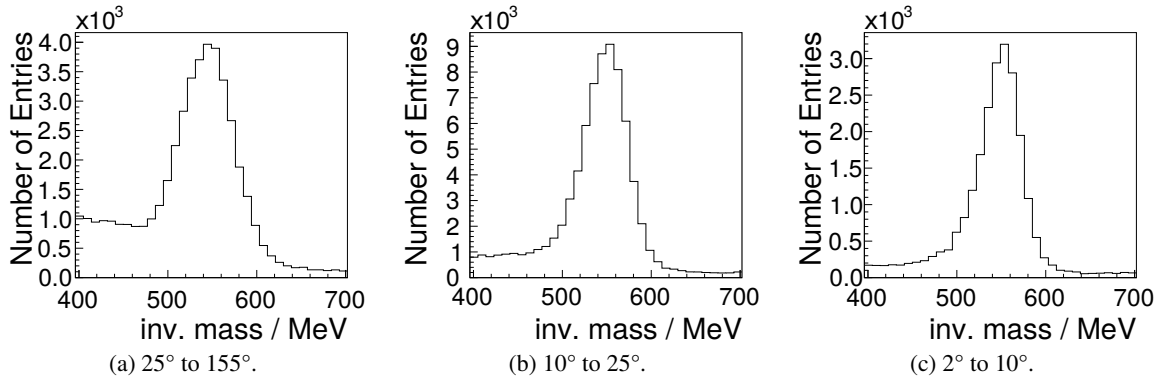
Figure 4.17: Invariant mass of $\gamma\gamma$ in the $\gamma p \rightarrow \eta p$ reaction with different missing proton θ directions. The peak correspond to identified η mesons. The background under the peak depends on the missing proton direction. The plots are divided in different detector regions with (a) for the BGO calorimeter, (b) for SciRi and (c) for the forward spectrometer.

50° are counted together with the total number of events to determine the proton detection efficiency. The resulting efficiency is dependent on ϕ, θ and momentum of the proton. In figure 4.22, the measured efficiency is plotted depending on θ and momentum of the calculated proton. The red line marks the change of detector regions. It is expected that the efficiency drops to zero between 24.7° to 25°, as no detector covers these angles. This is not the case due to the angular resolution of the meson, which was used to determine the proton direction. These events with momentum 1000 MeV to 1400 MeV were selected for the efficiency against θ plot in figure 4.23 with black points. The ηp reaction was also included, marked by the green points. The simulation for $\pi^0 p$ is marked with red and ηp with blue points. The dip in the efficiency can be seen at the detector acceptance change from SciRi to the forward spectrometer at around 9° and from SciRi to BGO at 27°. As mentioned before, due to the limited angular resolution the change in efficiency is smeared out. The efficiency does not account for particle loss due to multiple scattering or geometry. Even if the detector efficiency is 100 % the efficiency determined through this method may show a smaller result. The goal for this efficiency determination is the agreement of real data analysis and simulation, to ensure that the geometry and efficiency of the detectors is understood. The ratio between real data and simulation can be seen in figure 4.24. Black points show the ratio for the $\pi^0 p$ final-state and red points for the ηp final-state. These ratios should be exactly unity if the BGO-OD experiment geometry were correctly represented in the simulation. This is achieved with the $\pi^0 p$ reaction to a level of 5 %, however the ηp identification does not show the same distribution, particularly in the gap between the different detector regions. This deviation is still under investigation. It would hint on possible geometry difference between real and simulated data. The presented cross sections in section 5 confirm this indirectly as some angular bins show deviations from the known cross sections.

4.4 Trigger influence on the data

The detector efficiency influences the data acquisition. To preselect the data of interest, a trigger system was implemented, which decides within nanoseconds if a hadronic event took place. A hadronic event can be identified by forming a timing coincidence from different detector segments. All trigger conditions are shown in table 4.3. Before a hadronic reaction can take place, a bremsstrahlung event should produce a photon at the radiator. This means a Tagger hits should always be present. The
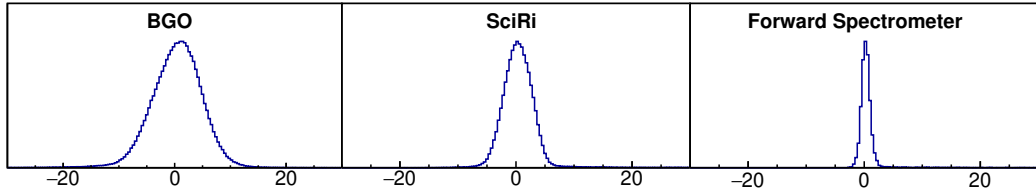
Figure 4.18: θ difference in degree between calculated and measured proton direction for the $\pi^0 p$ final-state.
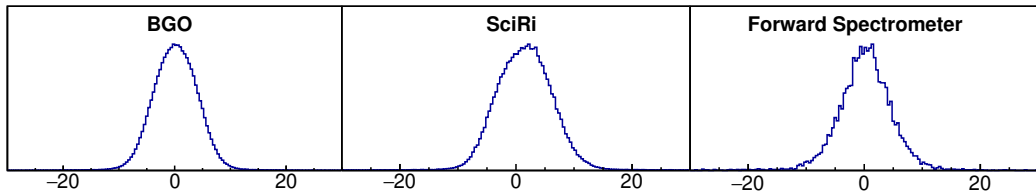
Figure 4.19: ϕ difference in degree between calculated and measured proton direction for the $\pi^0 p$ final-state.
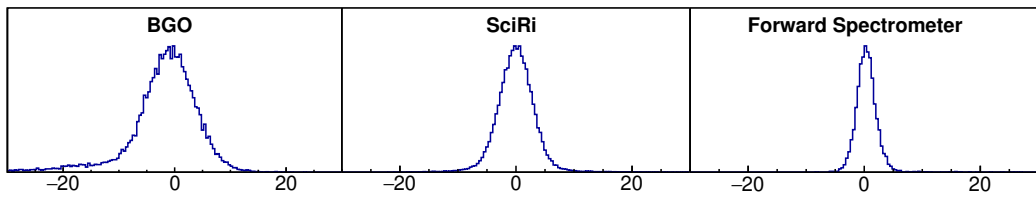
Figure 4.20: θ difference in degree between calculated and measured proton direction for the ηp final-state.
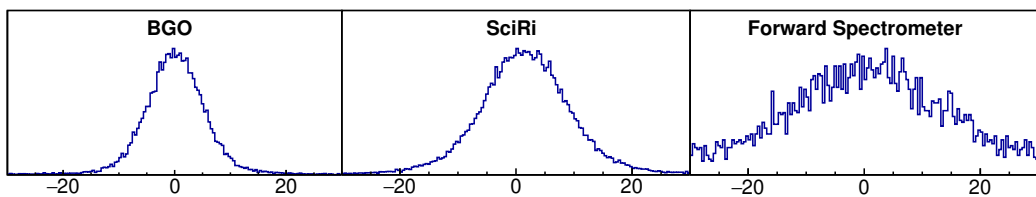
Figure 4.21: ϕ difference in degree between calculated and measured proton direction for the ηp final-state.
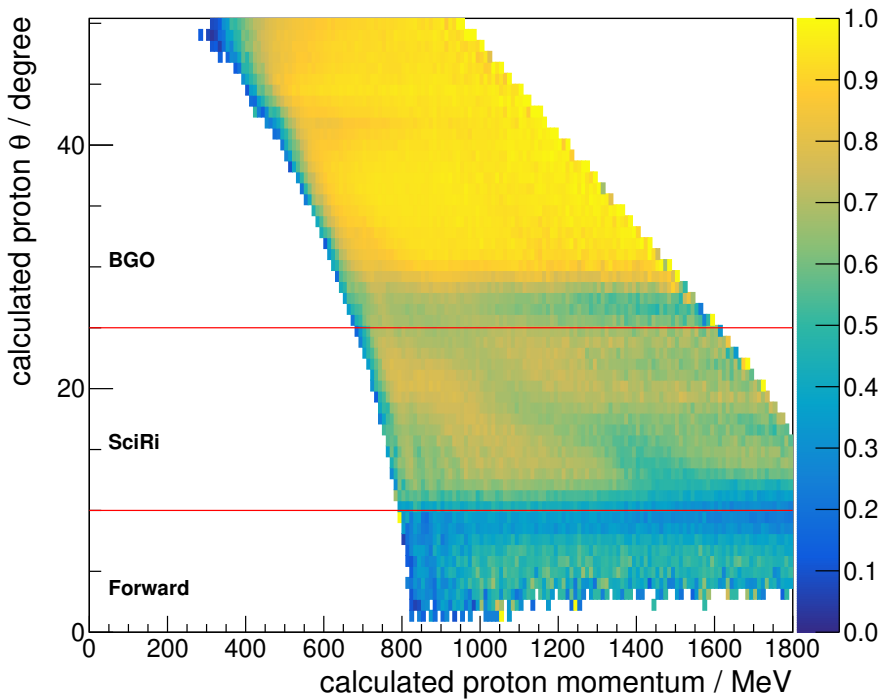
Figure 4.22: Proton detection efficiency as a function of proton θ and momentum for the $\pi^0 p$ reaction. The proton direction and momentum are determined from the detected π^0 and beam energy. The determined efficiency is shown in color. The change in detector region is indicated by the red lines.
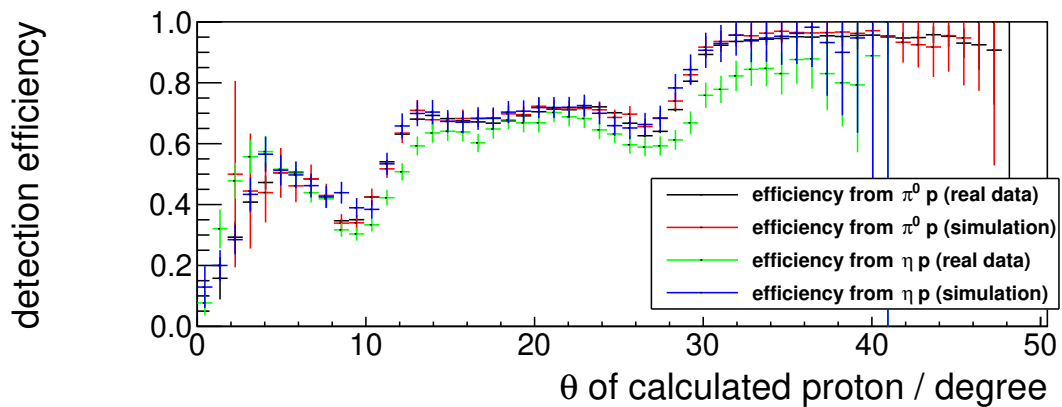
Figure 4.23: Proton detection efficiency as a function of θ. The proton direction was determined from the meson and beam energy. The black points mark the efficiency determined for the $\pi^0 p$ final-state, while the ηp final-state is marked by the green points. The simulation for $\pi^0 p$ is marked with red and ηp with blue points.
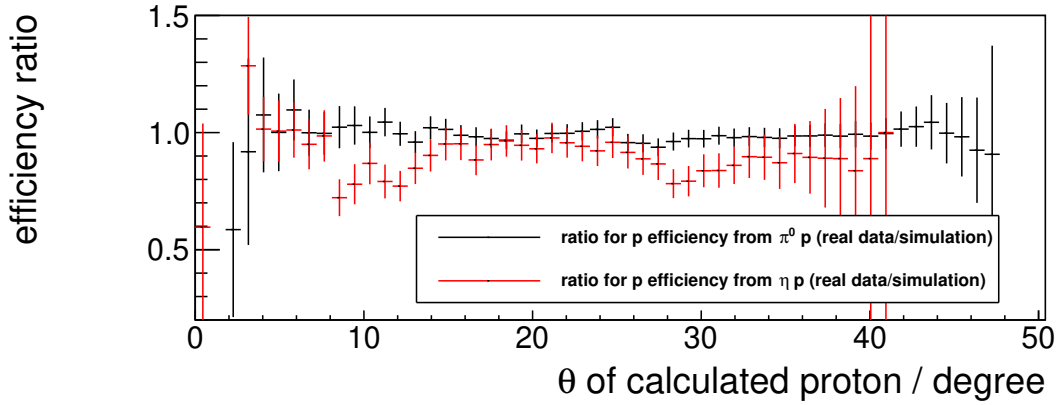
Figure 4.24: Proton detection efficiency ratio between real data and simulation as a function of θ for the $\gamma\gamma p$ final-state. Black points are determined from the $\pi^0 p$ reaction and red points from the ηp reaction.

Trigger	Condition
1	Tagger & BGO ($\gtrsim 200\,\text{MeV}$)
2	Tagger & BGO ($\gtrsim 100\,\text{MeV}$) & SciRi
3	Tagger & SciRi & SciFi2 & ToF
4	Tagger & BGO ($\gtrsim 100\,\text{MeV}$) & SciFi2 & ToF

Table 4.3: Currently used trigger conditions. During data taking any trigger can start the data acquisition. The Tagger has the best time resolution and is responsible for the time offset correction and is required for all triggers. The values in brackets show the minimal energy deposit in the BGO for the trigger.

BGO calorimeter produces a signal for most hadronic events, due to the large angular acceptance and sensitivity to most particles. The analog signals of the 480 BGO crystals are summed up to a single signal which is then discriminated to produce a trigger signal depending on the total energy deposited in the BGO calorimeter. Two discriminators are used to produce different energy thresholds. The first is a constant fraction discriminator which creates a signal for a total energy of around 200 MeV or higher. This is usually referred to as the high energy threshold inside the triggering system. The second discriminator creates a trigger signal for total energies of 100 MeV or higher, which is only used in coincidence with other detector regions and is therefore called the low energy threshold. The BGO energy trigger is described in detail in section 4.4.2.

The trigger conditions in table 4.3 were created to cover most hadronic reactions. As shown in chapter 2, the detectors used for triggering have different angular acceptances. The BGO calorimeter covers the central region from 25° to 155°. This means that trigger 1 is responsible for reactions which prefer to decay into this region, e.g., $\gamma p \to \pi^0 p$. Trigger 2 includes the SciRi detector which covers the angle 10° to 25°. Due to the additional detector, one can use the lower energy threshold for the BGO calorimeter. Trigger 3 and 4 include the forward region covering 2° to 12°. For this, the coincidence of SciFi2 and ToF is required. Trigger 2, 3 and 4 are responsible for the mixed charged decays e.g. $\gamma p \to K^+ \Sigma^0 \to K^+ \gamma \pi^- p$, as SciRi, SciFi2 and ToF do not efficiently detect neutral particles.

4.4.1 Timing

The trigger logic is implemented on an FPGA. During data taking the firmware is configured to the trigger conditions from table 4.3. The firmware of the FPGA samples incoming detector trigger attempts in 833 ps time steps. The Tagger has the best time resolution of all detectors and is used to create the trigger. The trigger is sampled in 833 ps time steps and is corrected afterwards during the analysis with the known time offset between the Tagger and trigger. More information about trigger and timing can be found in the PhD thesis of Daniel Hammann [39]. For the trigger simulation, this FPGA timing logic and behavior was modeled. The procedure is similar to standard time selection cuts, with the addition that the time of the signals are downsampled into 833 ps time steps.

4.4.2 BGO calorimeter energy threshold

In figure 4.25 the counts from the different trigger conditions are plotted against BGO energy. The two peaks in the distribution represent the two BGO energy thresholds used in the trigger. The high BGO threshold is in the range of 100 MeV to 220 MeV, the low threshold is at 50 MeV to 90 MeV and the trigger with no BGO energy requirement has no clear threshold. Note that the threshold is smeared out over a broad energy range instead of the expected sudden cutoff illustrated in figure 4.26. This has multiple reasons. First, the trigger signal discriminates the signal amplitude, while the energy in figure 4.25 is the summed integral. Deposited energy is proportional to the integral and amplitude of the PMT signal. The signal shape however is not stable and thus the relation between integral and amplitude is smeared accordingly. The second reason is the calibration of the crystals. The PMT's high voltage are calibrated roughly to a similar gain and during the analysis of the data the calibration is improved. Thus the resolutions of the energy during triggering and analysis are not equal.
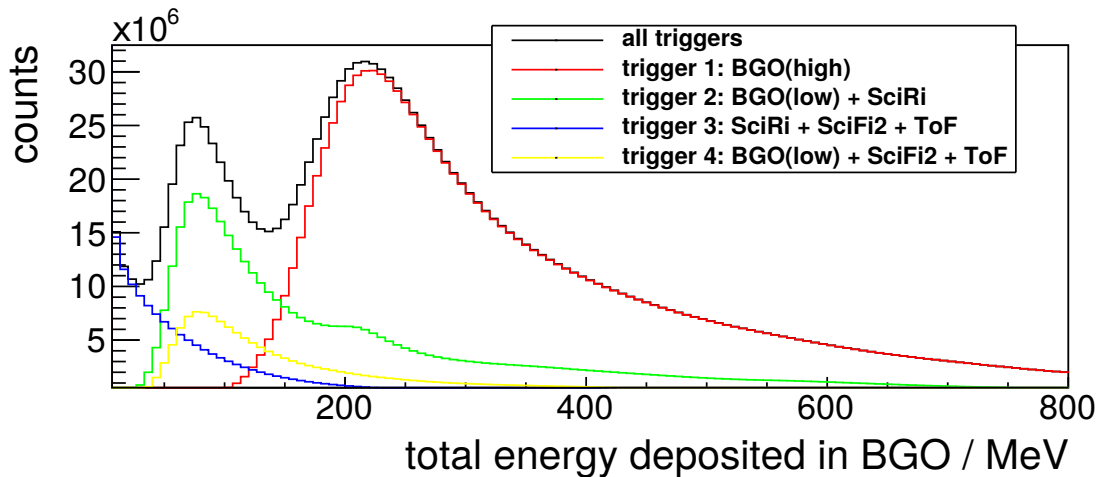
Figure 4.25: Total energy deposited in the BGO during the data taking. The energy is only measured during readout of triggered events. Black shows the total energy for the data taking for all trigger, while the colored lines represent individual triggers.

The distribution of the energy threshold needs to be simulated to determine the trigger efficiency during data taking. Each saved event has an entry for the fulfilled trigger conditions. This information can be used to determine the distribution of the BGO energy threshold. To determine the efficiency

of the high BGO energy threshold, η_{BGO}^{high}, combinations of the individual triggers are used. BGO energy $E_{trigger3}^{sum}$ with trigger 3 is triggered independent of the BGO energy. If the trigger 1 is active additionally to trigger 3, the resulting energy distribution $E_{trigger1+trigger3}^{sum}$ would form a product with the energy threshold, η_{BGO}^{high}. In figure 4.26 η_{BGO}^{high} is represented by the solid green line, $E_{trigger3}^{sum}$ has the same distribution as the dotted blue line and $E_{trigger1+trigger3}^{sum}$ follows the distribution of the dotted green line. Dividing the $E_{trigger1+trigger3}^{sum}$ by the $E_{trigger3}^{sum}$ distribution will result in η_{BGO}^{high}:

$$\eta_{BGO}^{high} = \frac{E_{trigger1+trigger3}^{sum}}{E_{trigger3}^{sum}} \tag{4.15}$$

This efficiencies are shown in figure 4.27. Note that this also includes inefficiencies of the BGO detector which are energy independent. In the older running periods a lower maximal efficiency resulted from a too narrow time cut for the analog energy sum signal, which limits the maximum efficiency value. This was resolved in the later running periods. The efficiency of the lower BGO energy threshold η_{BGO}^{low} can be determined:

$$\eta_{BGO}^{low} = \frac{E_{trigger2+trigger4}^{sum}}{E_{trigger3}^{sum}} \tag{4.16}$$

The results are shown in figure 4.28. The BGO threshold efficiencies are used directly as a probability function for the BGO trigger. This means the previous mentioned energy independent effects are simulated at the same time.
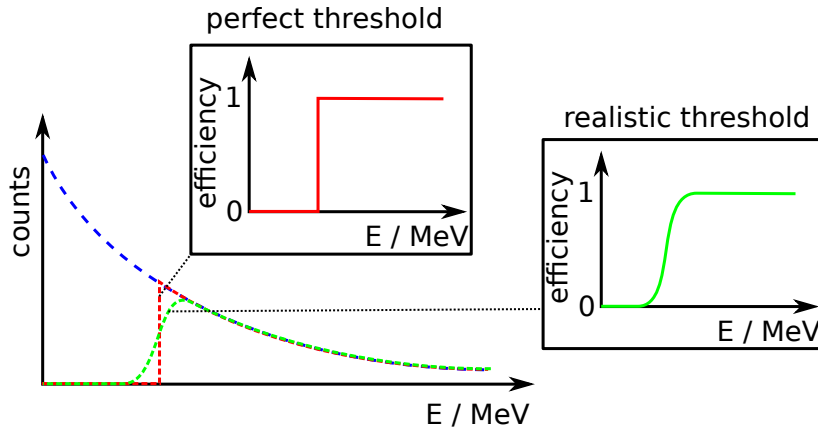
Figure 4.26: Threshold effects on energy distribution. The blue dotted line shows the total energy distribution. The green and red line show the resulting energy distribution with a perfect and realistic energy threshold.

The trigger can now be simulated depending on the reaction. As the trigger efficiency strongly depends on the reaction kinematics, no general statement on the efficiency can be made. For example, the prominent $\pi^0 p$ reaction would be detected by the $\pi^0 \rightarrow \gamma\gamma$ decay. This means at least 135 MeV is deposited in the BGO, if a π^0 is identified. Comparing with the efficiency in figure 4.27, it is clear that the influence of the trigger will decrease with higher beam energies due to the increase of the π^0 energy. The trigger efficiency influence on this reaction can be seen in the differential cross section in figure 5.15(b). The cross section for the identification without a trigger simulation is marked by blue points, and when including a trigger simulation by green points. They differ for low beam energies,

E_γ, but converge at higher energies. This shows that in the $\pi^0 p$ reaction the simulation of the trigger is not necessary for higher π^0 energies. As mentioned before this can not be stated for all reactions and individual studies are needed.
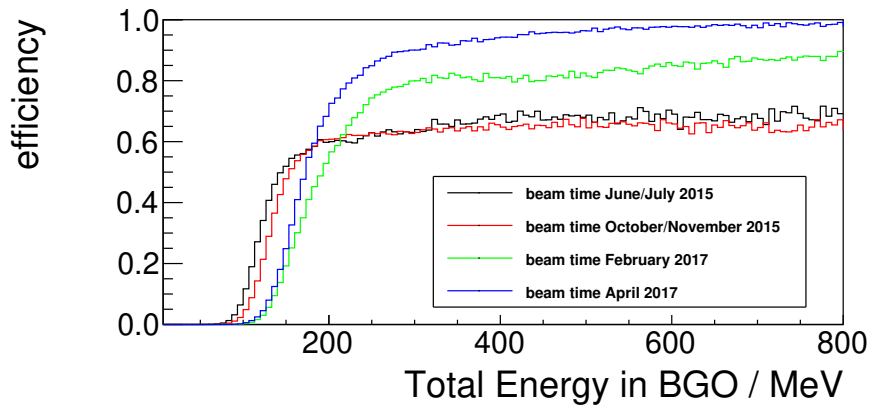
Figure 4.27: Trigger efficiency for the high BGO energy threshold for different running periods.
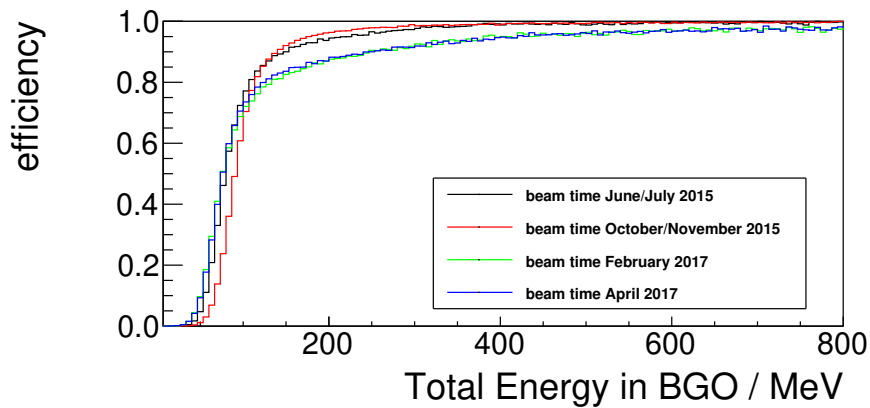
Figure 4.28: Trigger efficiency for the low BGO energy threshold for different running periods.

Benchmark reaction cross sections with BGO-OD

Section 4 described the steps taken to determine cross sections. The detector and trigger efficiency were shown in section 4.3 and 4.4 respectively. With this the reaction identification efficiency, η_{reco}, can be determined, and the identified event number from real data corrected. In this chapter, hadronic reactions are identified and the number of reactions are determined to extract differential cross sections in section 5.2. The reaction identification in real data and simulation are identical, so only the event identification procedure using real data will be shown. Most of the identified reactions have a well known cross section and are perfect to test the detector performance of the BGO-OD experiment. Table 5.1 lists the identified final-states and the extracted cross sections. The systematical errors are discussed in section 5.3. A summary of the results are presented in section 5.4.

5.1 Reaction identification

The event identification of the hadronic reactions is explained in detail in this section. The extracted cross section from the event identification is used to verify the photon flux number and the detector efficiency from chapter 4. Particles which decay and are identified in the final state of the studied reactions are listed in table 5.2. The event identification itself is similar for all the reactions identified in this chapter and follow these four steps:

1. Create all possible combinations of tracks. The event is discarded if the total number of tracks exceeds or is lower than the expected number of final particles of the reaction. All combinations

identified final-state	cross section
$\gamma p \to X p \to \gamma \gamma p$ (section 5.1.1)	$X = \pi^0$ (section 5.2.1)
	$X = \eta$ (section 5.2.2)
	$X = \eta'$ (section 5.2.4)
$\gamma p \to X p \to \gamma \gamma \pi^+ \pi^- p$ (section 5.1.2)	$X = \eta$ (section 5.2.2)
	$X = \omega$ (section 5.2.3)
	$X = \eta'$ (section 5.2.4)
$\gamma p \to K^+ \Sigma^0 \to K^+ \gamma \pi^- p$ (section 5.1.3)	(section 5.2.5)

Table 5.1: Identified reactions to benchmark the BGO-OD setup.

particle	mass / MeV	decay modes	branching ratio / %
p	938.3	stable	
$\pi^\pm$	139.6	$\mu^\pm \nu$	100
π^0	135.0	$\gamma\gamma$	99
η	547.9	$\gamma\gamma$	39
		$\pi^0\pi^0\pi^0$	33
		$\pi^0\pi^+\pi^-$	23
ω	782.7	$\pi^0\pi^+\pi^-$	89
		$\pi^0\gamma$	8
η'	957.8	$\pi^+\pi^-\eta$	43.4
		$\rho\gamma$	29.3
		$\pi^0\pi^0\eta$	21.6
		$\omega\gamma$	3
		$\gamma\gamma$	2
K^+	493.7	$\mu^+\nu_\mu$	63.6
		$\pi^+\pi^0$	20.7
Λ	1115.7	$p\pi^-$	64
		$n\pi^0$	36
Σ^0	1192.6	$\Lambda\gamma$	100

Table 5.2: Dominant decay modes of mesons and baryons used for particle identification in the analysis [3]. Shown particles decay almost immediately with the exception of the $\pi^\pm$ and K^+ meson. The $\pi^\pm$ has a life time of 26 ns and K^+ a live time of 12 ns, allowing the direct detection of these particles.

with the correct number of tracks are saved into a new array object. Each array entry includes the Tagger information for the initial state and the four-momentum of the final-state particles, which are determined from the tracks. Usually, only momentum or energy and the direction are measured. The mass of the particle is determined by which particle the track was associated to. This assumption leads to large number of combinatorics as each track can be associated to all possible final-state particles.

2. Select events where particles have the expected charge. In all detector regions it is possible to measure if a track is charged. The forward region determines the sign of the charge by the direction of deflection of the particle trajectory in the magnetic field. The intermediate region only detects charged particles, but no charge sign discrimination. The central region uses a BGO-Barrel coincidence to detect charge, but again no charge sign discrimination. The cut on the correct particle charge reduces the possible number of combinations significantly.

3. Select events where the total invariant mass of the initial and final-state are equal. The difference between initial and final state mass will be referred to as *excess mass*. The cut on this entity requires the detection of the initial photon and all final-state particles. The intermediate region lacks any energy or momentum information, so four momenta cannot be reconstructed. To overcome this, the measured particle direction and momentum conservation of the reaction are used to determine the momentum of up to three particles. This is described in detail in my Master thesis[22].

4. Employ a kinematic fit (see section 3.2). The kinematic fit improves the mass resolution of the
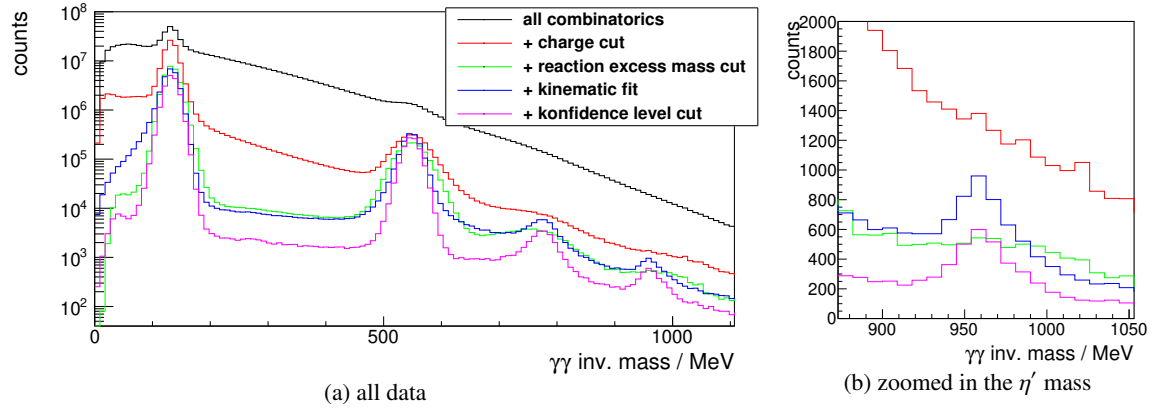
Figure 5.1: Invariant mass distribution of $\gamma\gamma$ for the $\gamma p \to Xp \to \gamma\gamma p$ reaction. The line colors in the legend list the chronicle development of the identification. Starting from the top the black line mark all combinations with three particles, red line adds the charge selection cut, green lines adds the reaction excess mass cut, blue line improves resolution using the kinematic fit technique and the purple line adds the confidence level cut from the kinematic fit. Figure (a) shows an overview over a large mass range. Showing peaks for π^0, η, ω and η' mesons. The figure (b) shows the mass around the η' mass.

reaction by improving the energy and direction resolutions of the particles and helps suppress noise and background events which do not fulfill the set constraints. The most basic constraint is the four-momentum conservation, which results in better results for the particle momentum compared to momentum determination from particle direction in step 3.

At this point the event identification is complete, and the remaining events are used to determine the yield for the wanted reaction. Usually background events remain after the selection cuts, with the signal seen on top of a background distribution. In this thesis the simulation is used to determine the different background distributions and RooFit[33] is used to determine the number of events. These events are then used to determine the differential cross section.

Well known reactions are identified in this section. These have been used for systematic checks of the BGO-OD detection efficiency and flux determination. These reactions are γp into $\pi^0 p$, ηp, $\eta' p$, ωp and $K^+\Sigma^0$. The final-state $K^+\Sigma^0$ is similar to $K^+\Sigma^0\pi^0$, which is identified in chapter 6 for $\Lambda(1405)$.

5.1.1 Identifying the $\gamma p \to Xp \to \gamma\gamma p$ reaction

The π^0, η and η' mesons can decay directly into two photons. This means that all events are selected where only three particles were detected. The possible combinatorics are then built from these three particles. In figure 5.1(a), the invariant mass of $\gamma\gamma$ is shown for all combinations by a black line. A π^0 peak and a η peak can be already seen at this point of the analysis. The signal to background ratio would make the signal extraction challenging however, and additionally, no η' signal is visible. The next step is to remove all combinations where the detected charges of the particle do not agree, for example, the afore mentioned method of using the Barrel detector for charge identification. The remaining combinations are shown by the red line in the same figure. At this point, the π^0 and η mesons yield could be extracted, however for the reaction identification the final-state proton needs to be confirmed first. Reactions with a π^0 in the final-state(e.g. $\gamma p \to \pi^0\pi^+ n...$) could not be distinguished from $\pi^0 p$ otherwise. This can be done in two ways. Either using the missing mass to the meson to identify the reaction, or by detecting the proton and check if the reaction has *excess mass*.

(a) reaction excess mass against $\gamma\gamma$ invariant mass.

(b) reaction excess mass
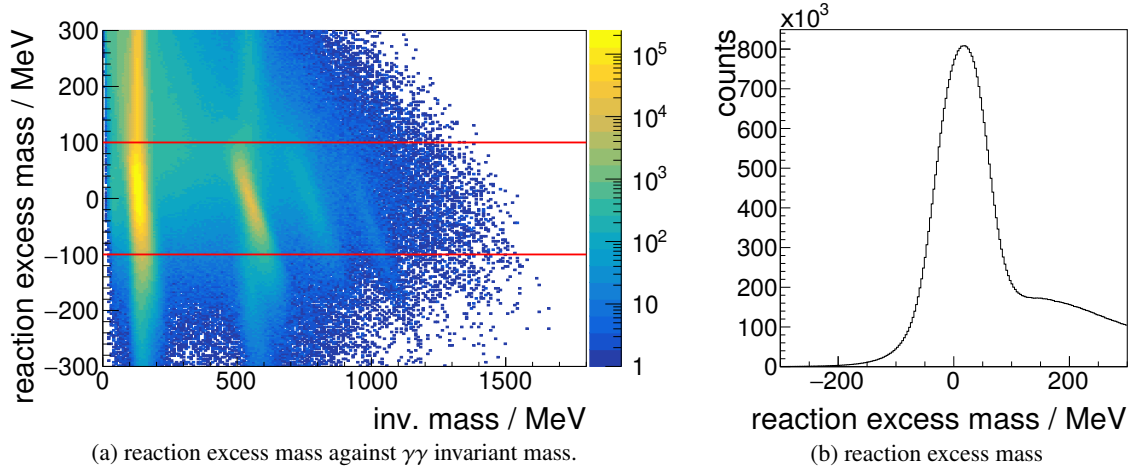
Figure 5.2: (a) shows the reaction missing mass against invariant mass of $\gamma\gamma$ for the $\gamma p \rightarrow X p \rightarrow \gamma\gamma p$ reaction. The colors represent an intensity distribution. A peak at zero reaction excess mass means that the detected particles agree to the assumed reaction. The $\pi^0 p$ events are seen at 135 MeV invariant $\gamma\gamma$ mass and no reaction excess mass. Additionally the ηp is seen for 550 MeV invariant $\gamma\gamma$ mass. Red lines mark the selection cut range for the event identification. The mass projection can be seen in (b).

The identification of the reaction using the missing mass technique does not need any further steps and the cross section is extracted in section 5.2.1. For the complete detection of the final-state, the mass difference between initial and final-state is used and so the four-momentum of all particles are needed. This is called reaction excess mass from here on. Particles detected in the intermediate region have only direction information, so the momentum needs to be determined using the initial state and the meson momentum. In figure 5.2 the reaction excess mass $|\gamma_{initial} + p_{initial}| - |\gamma_{final} + \gamma_{final} + p_{final}|$ against invariant mass of two photons is plotted. The red lines mark the selected region of events. While the η meson shows a peak within this selection cut, the π^0 peak looks more like a line extending to higher reaction excess mass. This line is due to the afore mentioned reactions with a π^0 in the final-state, such as $\pi^0\pi^+n$. It is expected that the reaction excess mass in this case would start at 135 MeV and extend to higher mass depending on the kinematics of the multi particle system. This means the other π^0 final-states and the $\pi^0 p$ state would be separated by at least 135 MeV reaction excess mass. The energy resolution of the BGO calorimeter smears out the missing mass to the point where both reactions overlap as seen in figure 5.2. The same also applies to η production, but is less pronounced. In figure 5.1(a) the selected events from figure 5.2 are marked by the green line. Peaks for ω and η' start to appear. The ω meson decays into $\pi^0\gamma$, but sometimes the electromagnetic shower of the two photons from the π^0 decay overlap resulting in the identification of only one high energy photon. Together with the other photon, the invariant mass of two photons will be that of the ω.

An improvement of the resolution using the kinematic fit is not needed for the identification of $\gamma p \rightarrow X p \rightarrow \gamma\gamma p$, but is done to check the kinematic fit performance. The constraint on the kinematic fit (see section 3.2) is only the four-momentum conservation. After the fit the invariant mass distribution changes slightly as seen in figure 5.1(a) marked by the blue line. The π^0 peak is distorted due to the events which have a π^0 in the final-state but are not from the $\gamma p \rightarrow \pi^0 p$ reaction (e.g. $\gamma p \rightarrow \pi^0\pi^0 p$...). In these cases the reaction excess mass selection cut did not remove all background channels. The remaining background channels are pushed to fulfill the four-momentum conservation, which in this case can only be achieved by changing the invariant mass. The result is a change in the background distribution. The resulting χ^2 distribution can be seen in 5.3(a). The distribution was

(a) χ^2 distribution with four degrees of freedom.

(b) χ^2 distribution with three degrees of freedom.

(c) Confidence level distribution. Black line marks selection cut.
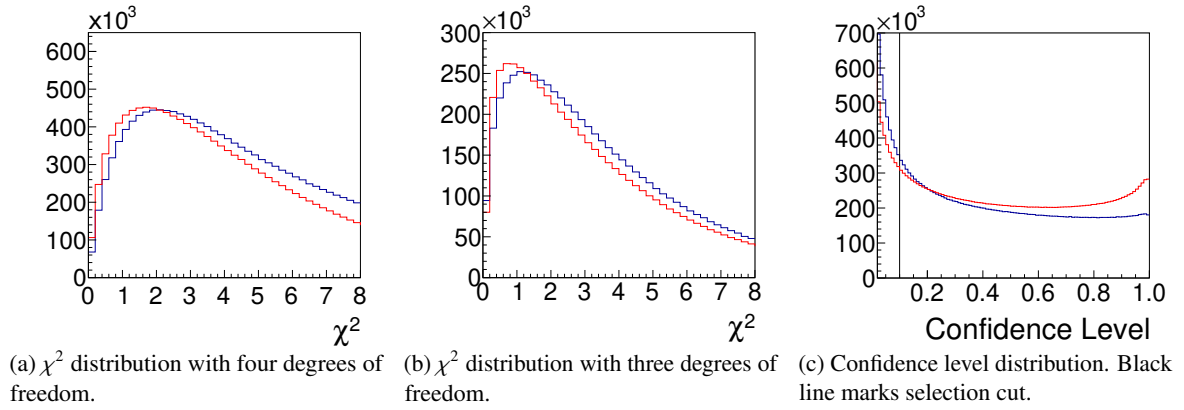
Figure 5.3: Kinematic fit results for the $\gamma p \to X p \to \gamma\gamma p$ reaction used to check the fit quality. Blue line marks the real data, while the red line is taken from simulation. Plot (a) and (b) show the χ^2 distributions. This distributions depend on the degree of freedom. Four degrees of freedom in plot (a) should peak at $\chi^2 = 2$ and three degree of freedom peaks at $\chi^2 = 1$. The confidence level distribution in plot (c) is determined with degree of freedom and χ^2, ideally resulting in a flat distribution.

already introduced in figure 3.1 and it is expected that it peaks at χ^2 of 2 for a degree of freedom of four. While the real data agrees to this prediction, the simulation peaks at a lower χ^2. This would indicate that the detector resolutions in the simulation are better than in reality. For protons detected in the intermediate region, the momentum is set to an indiscriminate number with a large error. This removes one degree of freedom from the kinematic fit, as the momentum in these cases is unknown and is determined by the kinematic fit. The resulting χ^2 distribution is seen in figure 5.3(b). The distribution peaks at χ^2 of 1 like expected. There are small deviations in the distributions between simulation and real data, they however agree sufficient to say that the kinematic fit works as expected. A lot of the background events can be removed using the confidence level of the kinematic fit. This value represents how much the single detector values needed to be changed to fulfill the condition and is determined using χ^2 and the degree of freedom. The confidence level distribution is shown in figure 5.3(c) with the selection cut marked by the black line. In section 3.2.1 it was mentioned that the confidence level distribution must be flat if the used particle errors in the kinematic fit are similar to the real uncertainties. A rise at high confidence level means that the detector resolution used during the fit are too large. A drop would indicate too small errors. The rise on lower confidence level is expected to appear from background events which only accidentally fulfill the constraints. They are expected to follow an exponential distribution and the cut on confidence level needs to be set to the optimal signal background ratio. Using the confidence level cut more background events are removed which results in the purple line in figure 5.1(a). Compared to the green line the mass resolution has improved and the signal to background ratio has improved. The ω and η' meson masses are also more defined.

The difference between the fitted and the measured reaction parameters is used to determine the pull distributions of the individual parameters used in the fit. Each pull distribution is shown in figure 5.4. The x-axis is in multiple of sigma of the expected error provided to the kinematic fit. The simulation in red and real data in blue are shown in comparison to the expected distribution in green. If the errors provided to the kinematic fit agree with the actual detector divergences, the pull distribution will have a Gaussian shape with a sigma width of exactly one. The initial photon z component (figure 5.4(a)) does not agree to the simulation. A narrower distribution suggests that the given errors are too large, and that this needs further investigation. The momentum pull distribution for the SciRi detector 5.4(e)

is also narrower then the nominal distribution, however in this case it was deliberate. SciRi has no momentum resolution, thus setting the momentum error to a impossibly large value means that this parameter has no weight on the kinematic fit result. In general the $\hat{z}$ component for all particles seem to differ the most from the expected distribution. This could mean that the z component of one of the particle has an offset, which is then compensated by the other particles leading to an offset in the pull distribution for all particles. In such cases it is difficult to determine the main responsible detector. Apart from this discrepancies the pull distributions have a good agreement between simulation and real data, which indicates that the experiment setup is mostly understood.

Signal yield extraction

After the previous analysis steps, the background and signal are usually not separated completely. The mass distribution will usually show a background distribution with a Gaussian signal peak. The signal integral can be then extracted using side band subtraction and function fitting. This can only be done as a last step as all other information is lost at that point. For the differential cross section, the signals are extracted as a function of E_γ and $\cos(\theta_{CMS})$. The data is divided into intervals of cosines of meson production angle in the center of mass system, $\cos(\theta_{CMS})$, and initial photon energy, E_γ. Multiple invariant mass histograms are created for each $\cos(\theta_{CMS})$ and E_γ combination. The signal is extracted from these histograms by using the integral if the background contribution is negligible or fitting to determine the signal to noise ratio.

To check the influence of the trigger efficiency (section 4.4) and kinematic fit (section 3.2) the signal extraction is performed at different points in the analysis. First the signal is extracted after the reaction excess mass cut marked by the green line in figure 5.1(a). This extracted signal is corrected by the identification efficiency determined by the simulation in two different ways: One includes the simulated trigger efficiency and the other does not. Finally, the kinematic fit is applied with a confidence level cut. The three different cross section measurements are plotted in section 5.2.1.

Before the kinematic fit, the invariant mass of $\gamma\gamma$ can be seen in figure 5.5(a) and 5.5(b) for two angular bins. The pion mass peak has no visible background. Figure 5.6(a) and 5.6(b) shows a background distribution for higher missing mass originating from reactions with an additional particle to the missing proton. The simulated distributions for different reactions were fitted to the real data and are indicated in the legend. Figure 5.6(b) shows a mass offset between real data and the simulation. This shift in mass originates from non-linearities in the energy measurement of the BGO calorimeter for higher photon energies, which is currently under investigation.

After applying the kinematic fit, the invariant mass distribution does not change significantly, as seen in figure 5.7(a) and 5.7(b). The missing mass to $\gamma\gamma$ is forced to the proton mass, due to the kinematic fit four-momentum constraint. Background contributions can not be distinguished from the signal using the missing mass to $\gamma\gamma$. In figures 5.6, the missing mass to the π^0 before the kinematic fit has almost no background below the proton peak. The background in this case is assumed negligible and the signal number is equal to the π^0 number. In figure 5.1(a) it is possible to estimate the signal to background ratio. For the $\pi^0 p$ final-state, the signal is almost three orders of magnitude higher than the background, and the background can be estimated to 0.1 %. The ηp final-state signal is two orders of magnitude higher then the background, leading to an estimated 1 % background. The $\eta' p$ state can be seen in figure 5.1(b) more clearly and the background can be estimated to around 30 %.

The cross section is extracted in section 5.2.1 for $\pi^0 p$, section 5.2.2 for ηp and section 5.2.4 for $\eta' p$. The $\pi^0 p$ cross section was also extracted without using a kinematic fit.

(a) initial photon γ_i detected by Tagger

(b) photon γ_f detected by BGO calorimter

(c) proton p_f detected by BGO calorimeter

(d) proton p_f detected by SciRi

(e) proton p_f detected by forward detector
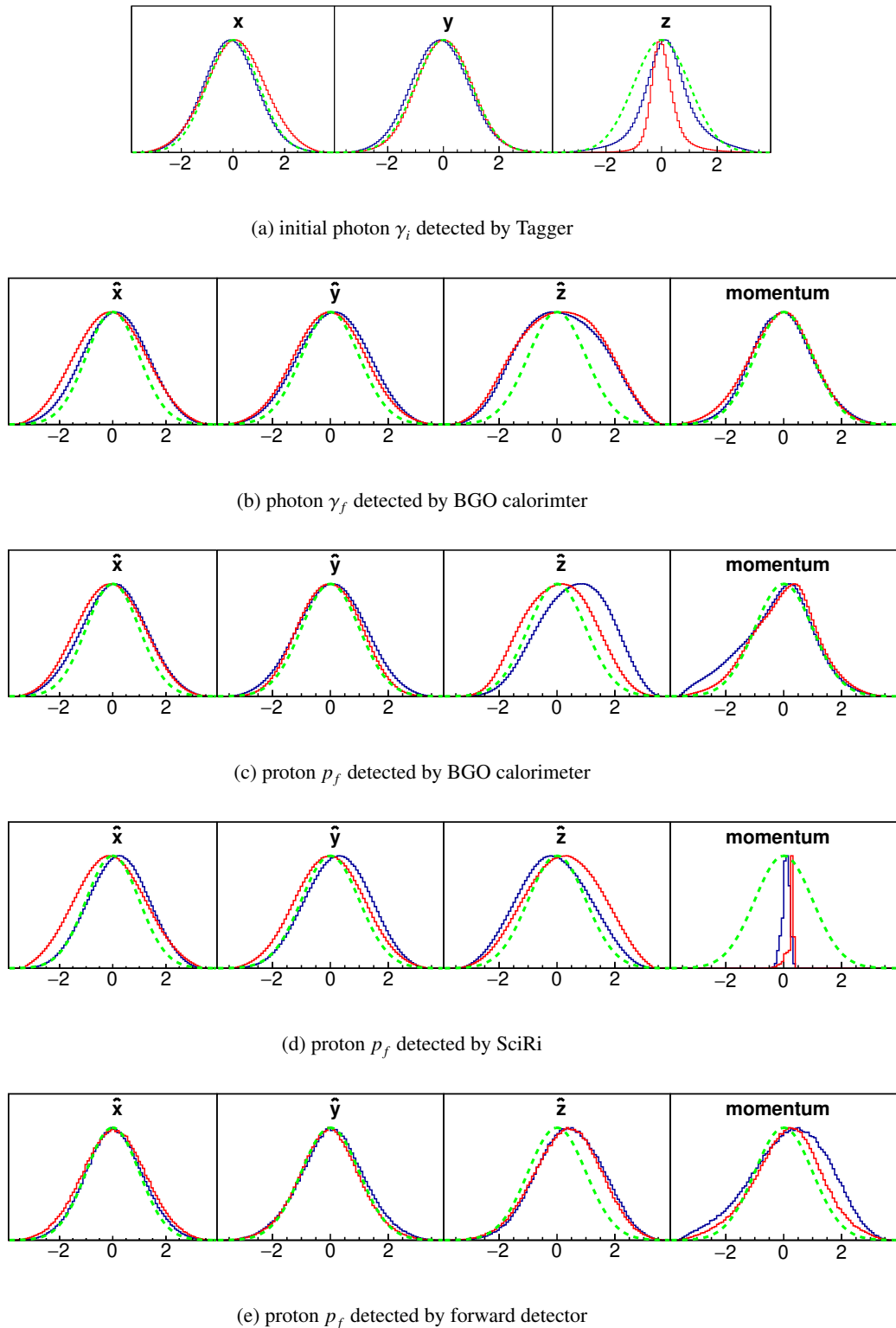
Figure 5.4: Pull distributions for the kinematic fit on the $\gamma_i p_i \rightarrow \gamma_f \gamma_f p_f$ reaction for different particles. A pull distribution gives the difference between the measured and fitted value in dimensions of σ widths. Blue line is for real data, while the red line is taken from simulation. The green dotted line marks the expected distribution of a Gaussian with a σ width of one.
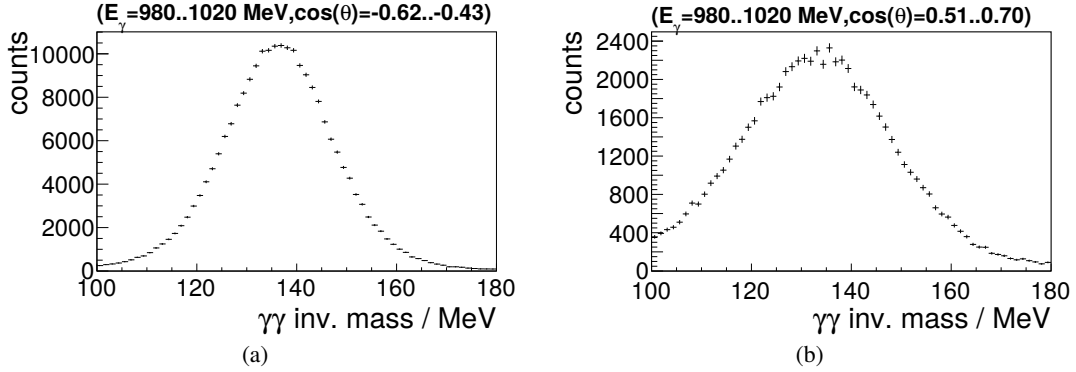
Figure 5.5: Invariant mass of $\gamma\gamma$ distribution in the $\gamma p \rightarrow Xp \rightarrow \gamma\gamma p$ reaction. The plots (a) and (b) show two bins in $\cos(\theta_{CMS})$ and E_γ. In both plots a peak for the π^0 mass is visible with negligible background contribution.
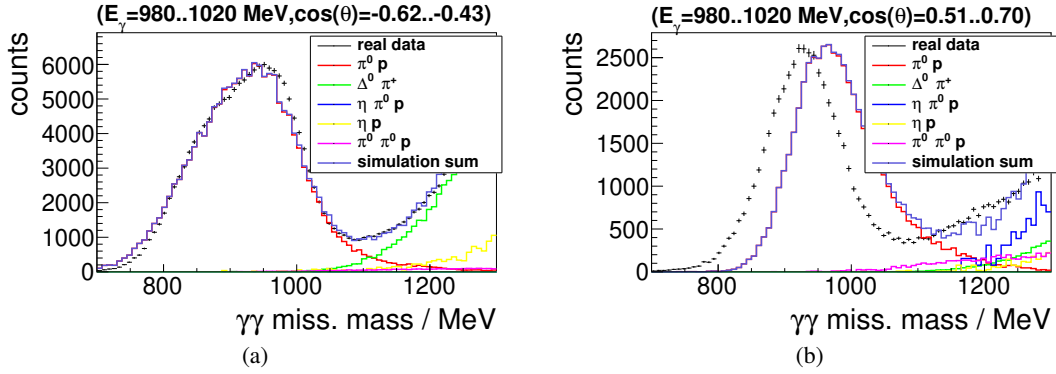
Figure 5.6: Missing mass to $\gamma\gamma$ distribution in the $\gamma p \rightarrow Xp \rightarrow \gamma\gamma p$ reaction. The plots (a) and (b) show two bins in $\cos(\theta_{CMS})$ and E_γ. The black points mark the real data. In both plots a peak for the proton is visible with a background contribution increasing with mass. The colored lines show the different fitted contributions from simulated reaction to the real data, while the blue line is the sum of all simulated reactions. The legend shows the color scheme for the simulated reactions.
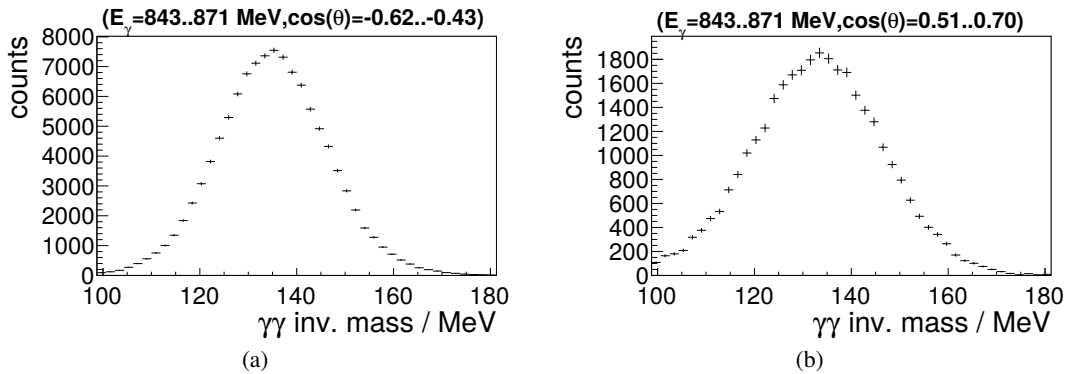
Figure 5.7: Invariant mass of $\gamma\gamma$ distribution in the $\gamma p \rightarrow Xp \rightarrow \gamma\gamma p$ reaction after applying the kinematic fit. (a) and (b) show two bins in $\cos(\theta_{CMS})$ and E_γ. In both plots a peak for the π^0 mass is visible without any background contribution.

5.1.2 Identifying the $\gamma p \rightarrow Xp \rightarrow \gamma\gamma\pi^+\pi^- p$ reaction

In this section η, ω and η' are identified via the $\gamma p \rightarrow Xp \rightarrow \gamma\gamma\pi^+\pi^- p$ reaction. The first three analysis steps are analogous to the $\gamma\gamma p$ final-state. The invariant mass for $\gamma\gamma\pi^+\pi^-$ is shown in figure 5.8 for all combinations by the black line. After the charge selection cut, the distribution is described by the red line reducing the statistics by an order of magnitude. Despite this, no peak corresponding to meson mass can be identified. The green line marks the invariant mass after the reaction excess mass cut. After this additional selection criteria small peaks at the $\eta(550\,\mathrm{MeV})$ and $\omega(782\,\mathrm{MeV})$ masses appear. The $\gamma\gamma$ invariant mass can be used to further reduce any background. In figure 5.9, the invariant mass of $\gamma\gamma$ is shown. The π^0 and η mesons can be clearly identified. Compared to the identification in section 5.1.1, the background contribution below the π^0 and η mesons is higher, due to their smaller cross sections. The next step of the analysis uses the kinematic fit. The $\gamma\gamma$ mass constrain is added to the usual four-momentum constraint. There are two options for this condition, either that the two photons originate from a π^0 or η decay. Both options are investigated and are set as a constraint to the kinematic fit.
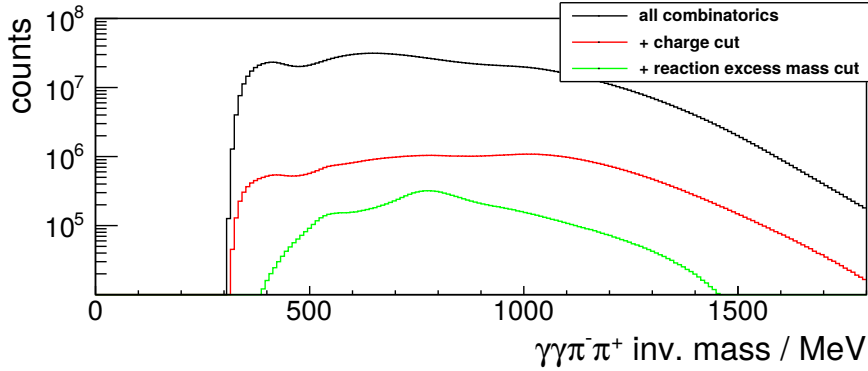
Figure 5.8: Invariant mass distribution of $\gamma\gamma\pi^+\pi^-$ for the $\gamma p \rightarrow \gamma\gamma\pi^+\pi^- p$ reaction. The line colors in the legend list the chronicle development of the event identification. Starting from the top the black line mark all combinations with five particles, red line adds the charge selection cut and green lines adds the reaction excess mass cut. Further analysis steps depend on the $\gamma\gamma$ mass. After the reaction excess mass selection cut, small peaks consistent with the ω and η mesons are visible.

$\pi^0 \rightarrow \gamma\gamma$ constraint in the $\gamma p \rightarrow Xp \rightarrow \gamma\gamma\pi^+\pi^- p$ reaction

If the two photons originate from the π^0 decay, the total final-state is $\pi^0\pi^+\pi^- p$. Both ω and η can decay into $\pi^0\pi^+\pi^-$, so both mesons should be reproducible in the invariant mass spectrum. The invariant mass after the kinematic fit is shown in figure 5.10. Compared to the distribution in 5.8, the η and ω are sharper and clearly visible. The distribution below the peak originates from the free production of $\pi^0\pi^+\pi^-$. This can not be removed by a kinematic fit, as it fulfills all imposed constraints. Figure 5.11 shows two example bins, where signal and background have been fitted. The cross section extracted for the η and ω is shown in section 5.2.2 and section 5.2.3 respectively.
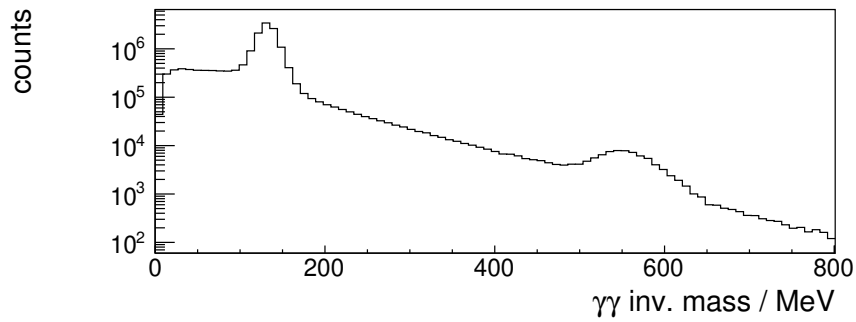
Figure 5.9: Invariant mass distribution of $\gamma\gamma$ in the $\gamma p \to \gamma\gamma\pi^+\pi^- p$ reaction. This distribution is achieved after the missing mass cut (green line in figure 5.8). A peak for the π^0 and η meson are visible.
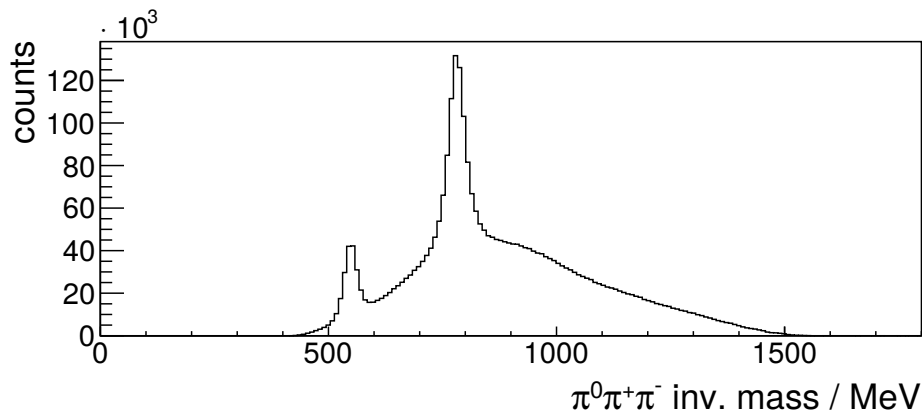
Figure 5.10: Invariant mass distribution of $\pi^0\pi^+\pi^-$ for the $\gamma p \to \pi^0\pi^+\pi^- p$ reaction. The shown results are after a kinematic fit with confidence level cut. One additional condition on the fit was the $\pi^0 \to \gamma\gamma$ decay. The η and ω meson masses are clearly visible.
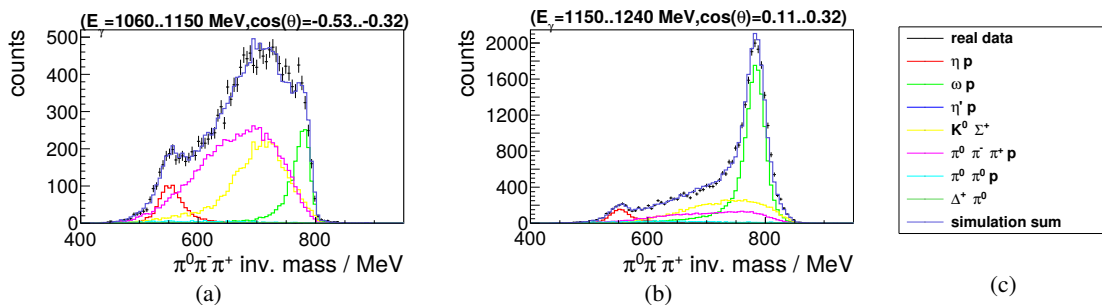
Figure 5.11: Invariant mass of $\pi^0\pi^+\pi^-$ distribution in the $\gamma p \to Xp \to \pi^0\pi^+\pi^- p$ reaction. The plots (a) and (b) show two angle and energy bins. The real data is marked by black points while different simulated reactions are indicated by the colors in (c).

$\eta \to \gamma\gamma$ constraint in the $\gamma p \to Xp \to \gamma\gamma\pi^+\pi^- p$ reaction

Selecting events where the two photon mass is consistent with the η are used to identify the η' decay into $\eta\pi^+\pi^-$. Figure 5.12 shows the results of the kinematic fit with the additional constraint that the two photons originate from an η decay. A clear peak at the η' mass is visible. The data set is not sufficient to fit the background for every angle and energy bin, and the background is estimated to increase the cross section by up to 20 %. The extracted cross section is discussed in section 5.2.4.
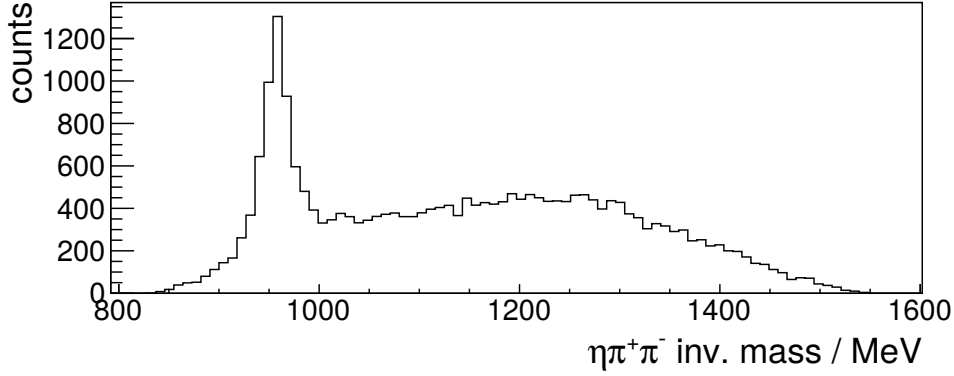
Figure 5.12: Invariant mass distribution of $\eta\pi^+\pi^-$ for the $\gamma p \to \eta\pi^+\pi^- p$ reaction. The shown results are after a kinematic fit with confidence level cut. One additional condition on the fit was the $\eta \to \gamma\gamma$ decay. A peak for the η' meson is visible.

5.1.3 Identifying the $\gamma p \to K^+\Sigma^0 \to K^+\gamma\Lambda \to K^+\gamma\pi^- p$ reaction
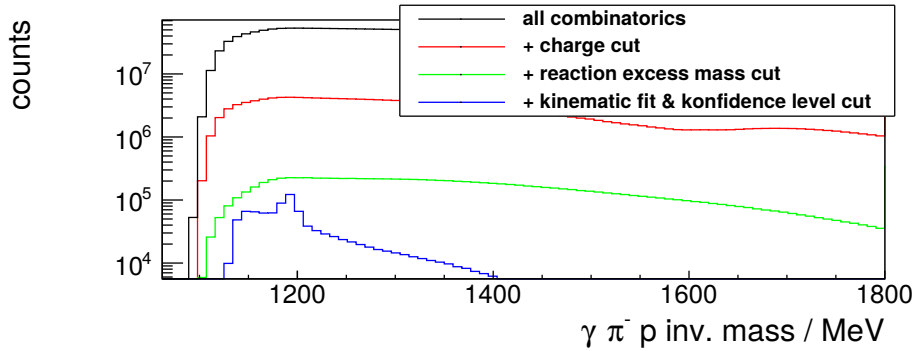
Figure 5.13: Invariant mass distribution of $\gamma\pi^- p$ for the $\gamma p \to K^+\gamma\Lambda$ reaction. The line colors in the legend list the chronicle development of the identification. Starting from the top the black line mark all combinations with four particles, red line adds the charge selection cut, green lines adds the reaction excess mass cut and blue line improves resolution using the kinematic fit technique while removing events below the confidence level cut. After the kinematic fit a peak for the Σ^0 hyperon mass at 1192 MeV is visible.

The goal is to identify $\gamma p \to K^+\Sigma^0$ via $\gamma p \to K^+\Sigma^0 \to K^+\gamma\Lambda \to K^+\gamma\pi^- p$. The Σ^0 decays exclusively into $\gamma\Lambda$. In this event identification, the $\Lambda \to \pi^- p$ decay is used to identify Λ with a branching ratio

of 64 %. The final-state, $K^+\gamma\pi^- p$ has three charged and one uncharged particle and is comparable to the event identification in section 5.1.2. In figure 5.13 the steps of the identification are shown in the invariant mass of $\gamma\pi^- p$. All combinatorial are in black. No structure can be identified at this point. With no particle identification, pions and kaons may be misidentified. Adding the charge selection cut yields the red distribution, however this does not differentiate between different charged particles. The reaction excess mass cut shown by the green line does also not change the distribution. So far, each step in the analysis reduced the statistics by a factor of ten, but no definite Σ^0 peak is visible. This means that almost all reactions with higher or similar cross sections contribute to the background. Applying a kinematic fit with a confidence level cut results in the distribution shown by the blue line. This reduces the background to a point where a Σ^0 peak is now distinguishable from the background. The constraint of the $\Lambda \rightarrow \pi^- p$ decay was added to the kinematic fit to the standard four-momentum conservation, increasing the mass resolution.

The data after the kinematic fit is divided in energy and angular bins and the invariant mass is fitted. One example fit is shown in figure 5.14. The main contributions to the background are ωp and $\pi^+\pi^-\pi^0 p$ which have similar kinematics, and the $K^+\Lambda$ reaction where an additional photon is created by split off clusters or noise (see section 2.3.3). The cross section is extracted in section 5.2.5.
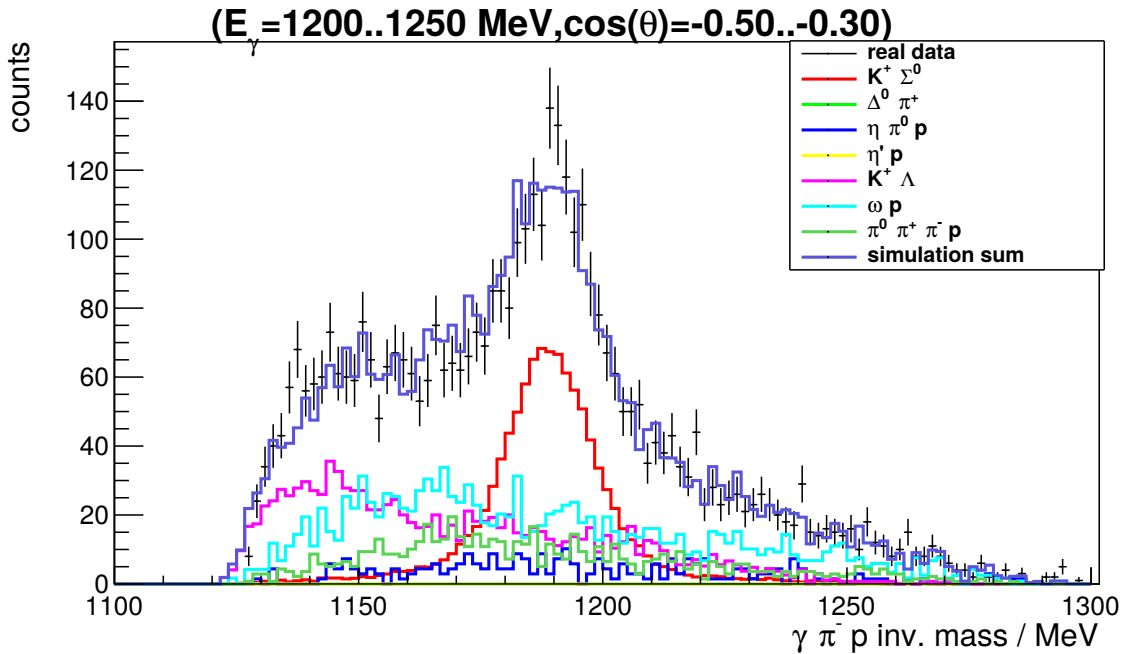
Figure 5.14: Invariant mass of $\gamma\pi^- p$ distribution in the $\gamma p \rightarrow K^+\gamma\pi^- p$ reaction. The distribution shows a $E_\gamma = (1225 \pm 25)\,$MeV and $\cos(\theta_{CMS}) = -0.4 \pm 0.1$ bin. The real data is marked by black points while different simulated reactions are indicated by the colors in the legend. Not all simulated reaction show a contribution in this bin, but are needed for other energy and theta bins.

5.2 Differential cross section

In this section the differential cross section is determined for a selected list of reactions and discussed. The differential cross section is determined using the methods shown in chapter 4, and the number of events extracted shown in section 5.1. The reaction identification efficiency is determined using simulated data. Using the photon flux from chapter 4.2, the reaction number is normalized and the differential cross section can then be determined using the target density. The cross sections are compared to results from other experiments, as well as the Bonn-Gatchina Partial Wave Analysis Group [40] solutions if present. A partial wave analysis is a technique for solving scattering problems. It decomposes each wave into its constituent angular momentum component and solves the equations using boundary conditions.

5.2.1 $\gamma p \rightarrow \pi^0 p$

The identification of $\pi^0 p$ is done via the $\pi^0 \rightarrow \gamma\gamma$ decay which has a branching ratio of 98.8 %. The event identification is explained in more detail in section 5.1.1. The differential cross section against beam energy E_γ is shown in figure 5.15(a) and against $\cos(\theta_{CMS})$ in figure 5.15(b). The red line shows the fit results of the Bonn-Gatchina Partial Wave Analysis Group [40].
The blue, green and black points represent different stages in the identification of $\gamma p \rightarrow \pi^0 p$:

blue line: The event identification ends with the reaction excess mass cut. The simulated identification efficiency for event normalization does not include the trigger efficiency of the data taking.

green line: The event identification ends with the reaction excess mass cut. The simulated identification efficiency includes all known efficiencies.

black line: The event identification goes through all steps. The kinematic fit is applied with a confidence level cut. The simulated identification efficiency includes all known efficiencies.

The difference between the blue and green lines shows the influence of the trigger simulation. The BGO calorimeter high energy threshold for data taking is around 100 MeV to 200 MeV. The simulation of the trigger (section 4.4) checks how much energy was deposited in the BGO. Reconstructing a π^0 however can only be done if both photons are detected, which means at least 135 MeV, the mass of the π^0, deposited in the BGO. With higher beam energies the average energy of the π^0 increases. The requirement to identify $\pi^0 p$ fulfills the trigger system energy threshold most of the time. In figure 5.15(b), at low beam energy, the data with no trigger simulation (blue points) deviates from the Bonn-Gatchina fit, but agrees better at higher beam energies due to higher π^0 energy. The cross section including the trigger efficiency (green points) however agrees better to the Bonn-Gatchina fit even at low beam energies.
The kinematic fit uses constraints and known detector resolutions to improve the reaction resolution and suppress background events. These detector resolutions are usually simulated with the known detector response and geometry. Using the kinematic fit to improve the reaction resolution will work even if the simulated detector resolution does not agree perfectly to the real detector efficiency. The main problem arises during the confidence level cut. The confidence level is determined from the deviation of measured and fitted values normalized by the detector resolution. This means that the difference between detector resolution in real data and simulation could lead to a wrong determined event identification efficiency, resulting in too high or low cross sections. The black points in figure 5.15(b) include the kinematic fit. Compared to the green points with no kinematic fit, the influence
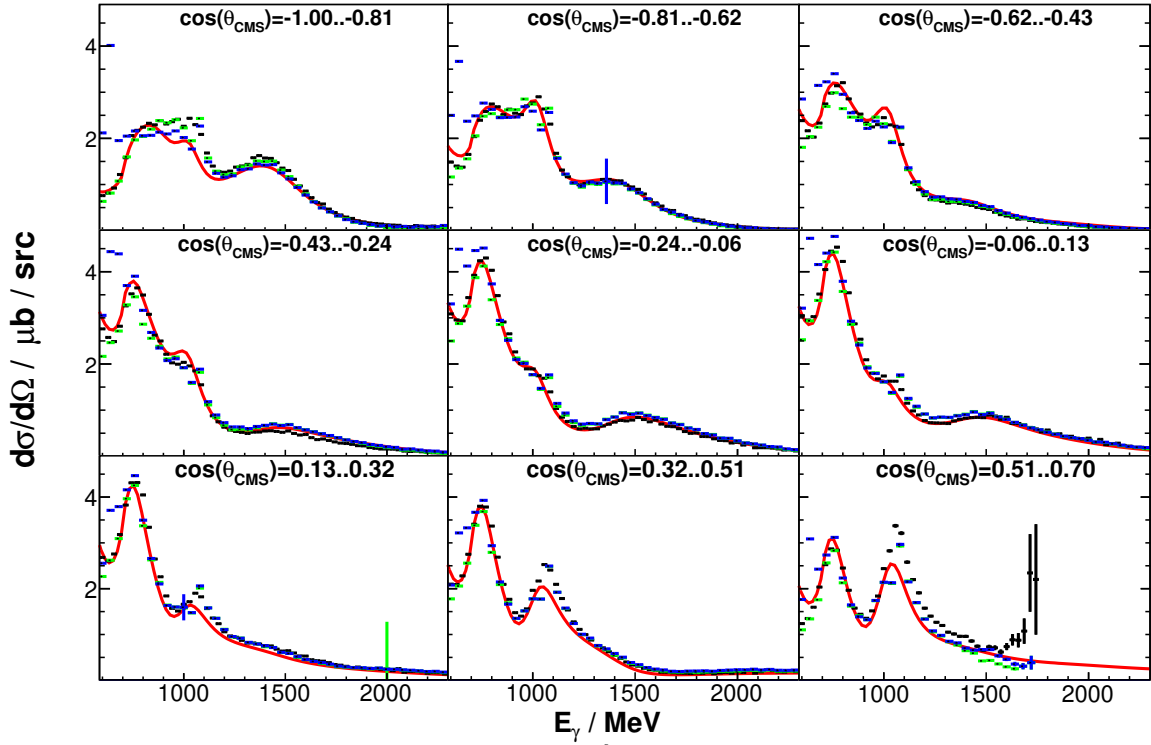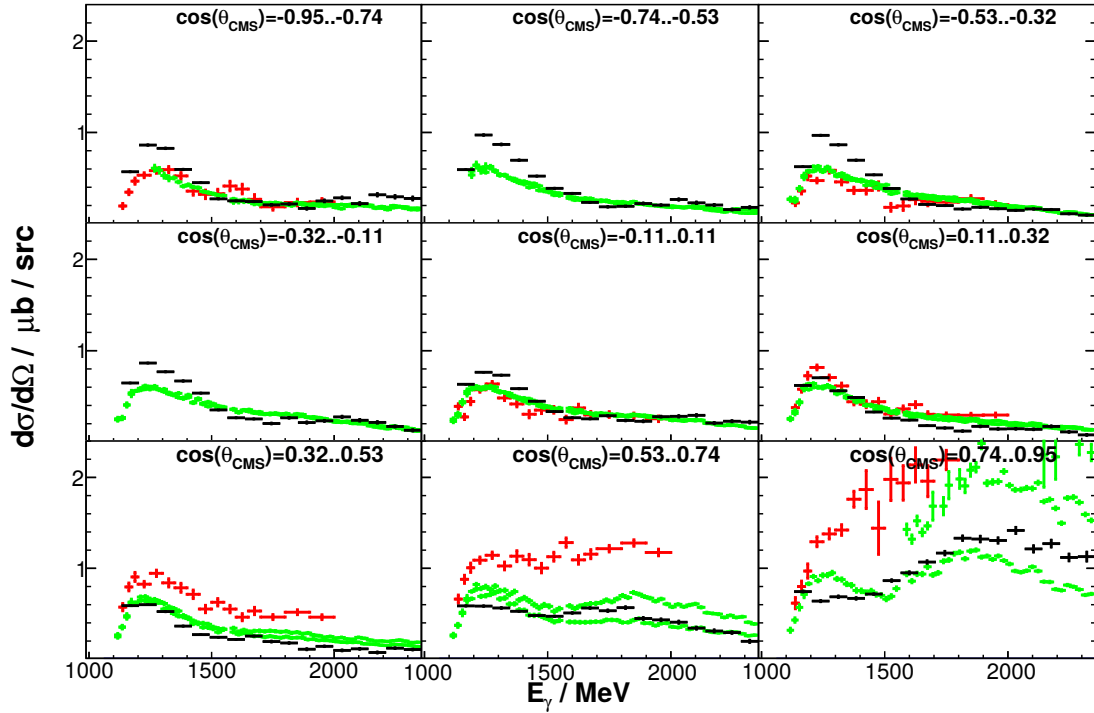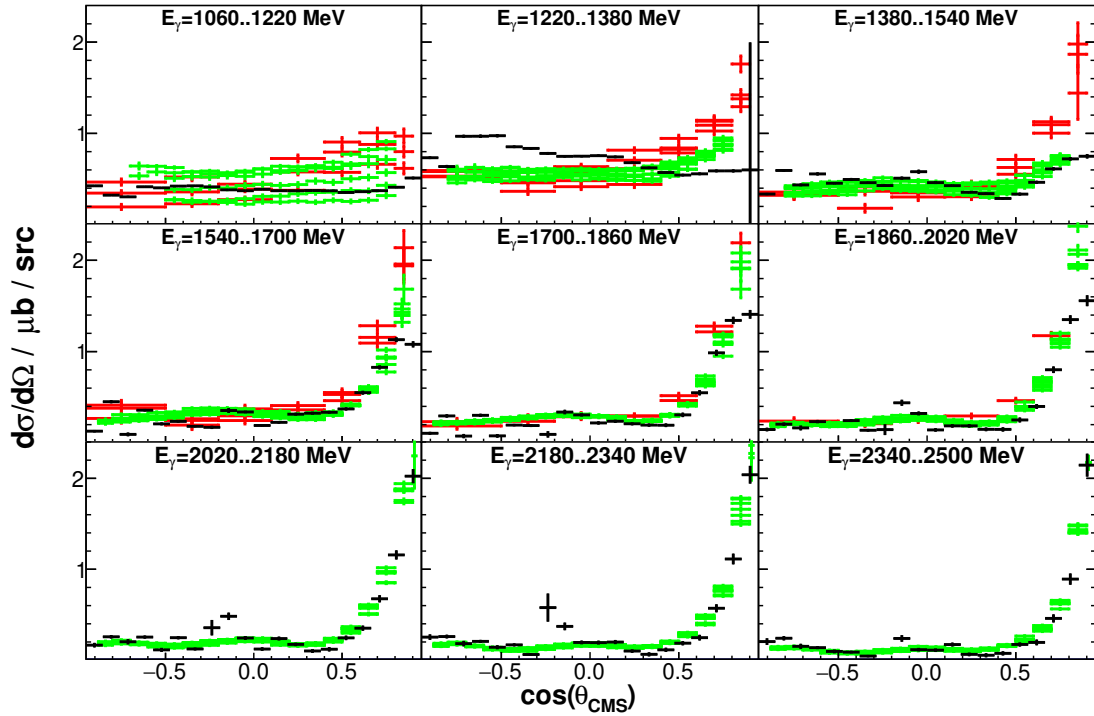
(a) Differential cross section for $\gamma p \to \pi^0 p$ against initial photon energy E_γ.
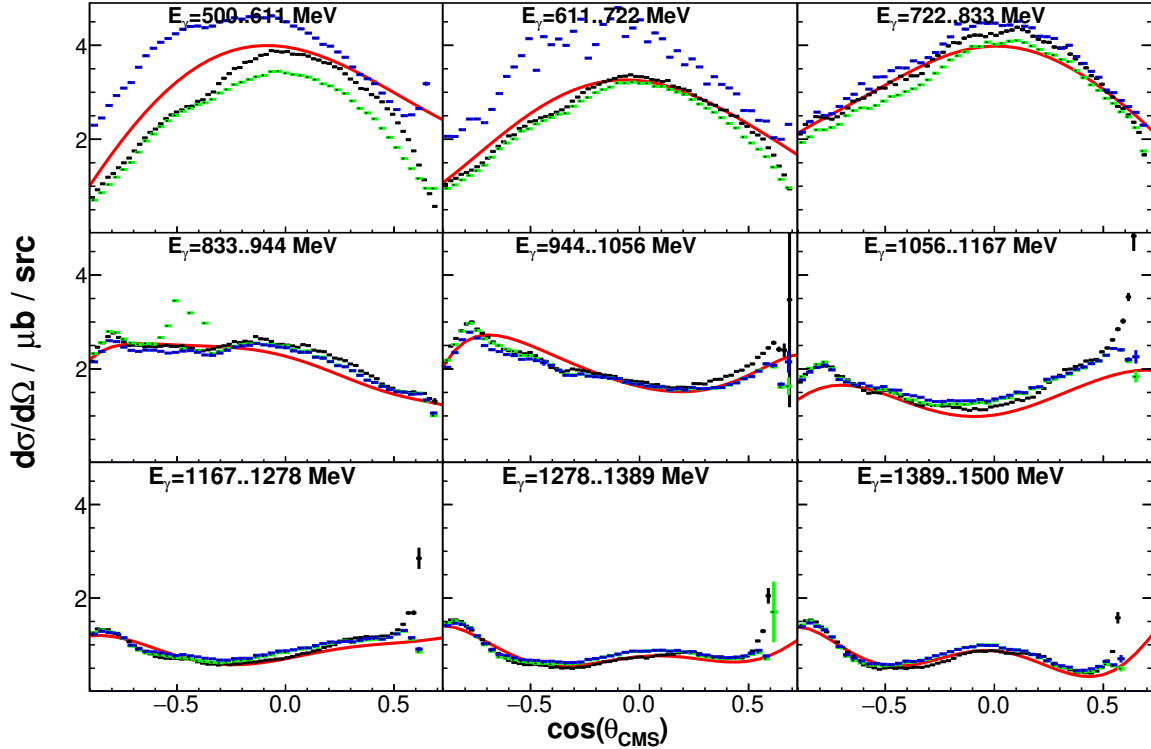
(b) Differential cross section for $\gamma p \to \pi^0 p$ against cosine θ of the meson in the center of mass system.

Figure 5.15: Differential cross section for $\gamma p \to \pi^0 p$. (a) is against initial photon energy E_γ and (b) against cosine θ of the meson in the center of mass system. Red line was taken from the Bonn-Gatchina Partial Wave Analysis Group [40]. Blue points are from the simplest event identification, green points are with simulated trigger conditions and black points are results with kinematic fit determined in this thesis.

seems to be negligible except for the low energy bin. This means the used detector resolutions for the kinematic fit determined through simulation agree with the real detector resolutions.

5.2.2 $\gamma p \to \eta p$

The ηp reaction is identified via the $\eta \to \gamma\gamma$ decay with 39.3 % and $\eta \to \pi^+\pi^-\pi^0$ decay with 22.7 % branching ratio. Except for the mass, the $\eta \to \gamma\gamma$ identification is identical to the $\pi^0 \to \gamma\gamma$ in section 5.2.1. The $\eta \to \pi^+\pi^-\pi^0$ identification was explained in section 5.1.2. The extracted cross sections can be seen in figures 5.16(a) and 5.16(b).

The extracted cross section from the $\eta \to \gamma\gamma$ and $\eta \to \pi^+\pi^-\pi^0$ decays agree. The $\gamma\gamma$ decay has a higher identification efficiency then the $\pi^+\pi^-\pi^0$ decay. The identification efficiency is inversely proportional to the particle number in the final-state due to small acceptance gaps in the setup. Also, the $\gamma\gamma$ decay has a higher branching ratio, which combined with the identification efficiency results in smaller statistical errors compared to the $\pi^+\pi^-\pi^0$ decay. In general the determined cross section agrees well to other experimental results. The BGO-OD experiment is also the only experiment identifying both decay modes.

Both event identifications show a smaller cross section for $\cos(\theta_{CMS})$ -1.0 to -0.5 and E_γ 700 MeV to 900 MeV than data from other experiments. This is also the case for $\cos(\theta_{CMS})$ 0.7 to 1.0. In both cases the $\gamma\gamma$ and $\pi^+\pi^-\pi^0$ decay agree, suggesting it is the kinematics of the final-state proton that causes these discrepancies. Investigations showed that in this region the proton is detected at θ_{lab} of $6°$ to $12°$. This angular region is covered by the forward spectrometer and SciRi. The drop in cross section could be explained by the acceptance change between both detectors. Further investigations are needed.

5.2.3 $\gamma p \to \omega p$

The ω decays to $\pi^0\pi^+\pi^-$ with a branching ratio of 89.2 %. This final-state was identified in section 5.1.2 and the extracted cross section is plotted in figures 5.17(a) and 5.17(b) with black points. The cross section agrees well to the CLAS data and shows smaller statistical errors then the Crystal Barrel experiment. The determined cross section deviates from other experiments for E_γ =1200 MeV to 1400 MeV and $\cos(\theta_{CMS})$ =-1.0 to -0.1 ω directions. Investigations in this region showed similar results to the findings in section 5.2.2. The θ_{lab} angle of the proton is between $6°$ to $12°$. In figure 5.17(b), the higher beam energies show a jump in the cross section at -0.2. In this case the angle represent the acceptance change between SciRi and BGO calorimeter. The angle covered by one SciRi ring is larger than the used $\cos(\theta_{CMS})$ bin size. This also creates a small rise and fall of the cross section over the angular range. This movement could be reduced by using larger angular bins. However the cross section should agree with the other experiments regardless of the angular binning, if the detector geometry was reproduced perfectly in the simulation.

5.2.4 $\gamma p \to \eta' p$

η' decays to $\gamma\gamma$ with a branching ratio of 2.2 % and to $\eta\pi^+\pi^- \to \gamma\gamma\pi^+\pi^-$ final-state with a branching ratio of 17.0 %. Section 5.1.1 shows how the $\gamma\gamma$ decay was identified and section 5.1.2 shows the steps for the $\eta\pi^+\pi^-$ decay. The cross sections in figure 5.18(a) and 5.18(b) are the results from this identification. The small cross section limits the statistics, preventing any background subtraction. Thus, the presented results are higher than the data of other experiments. Due to this, no general
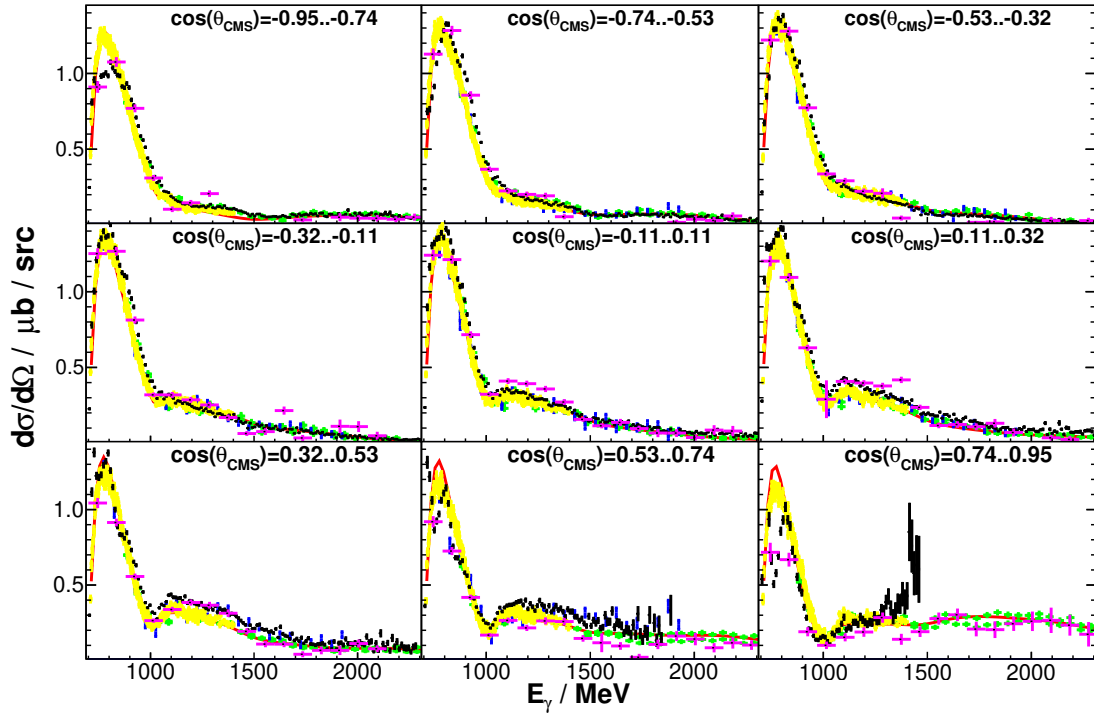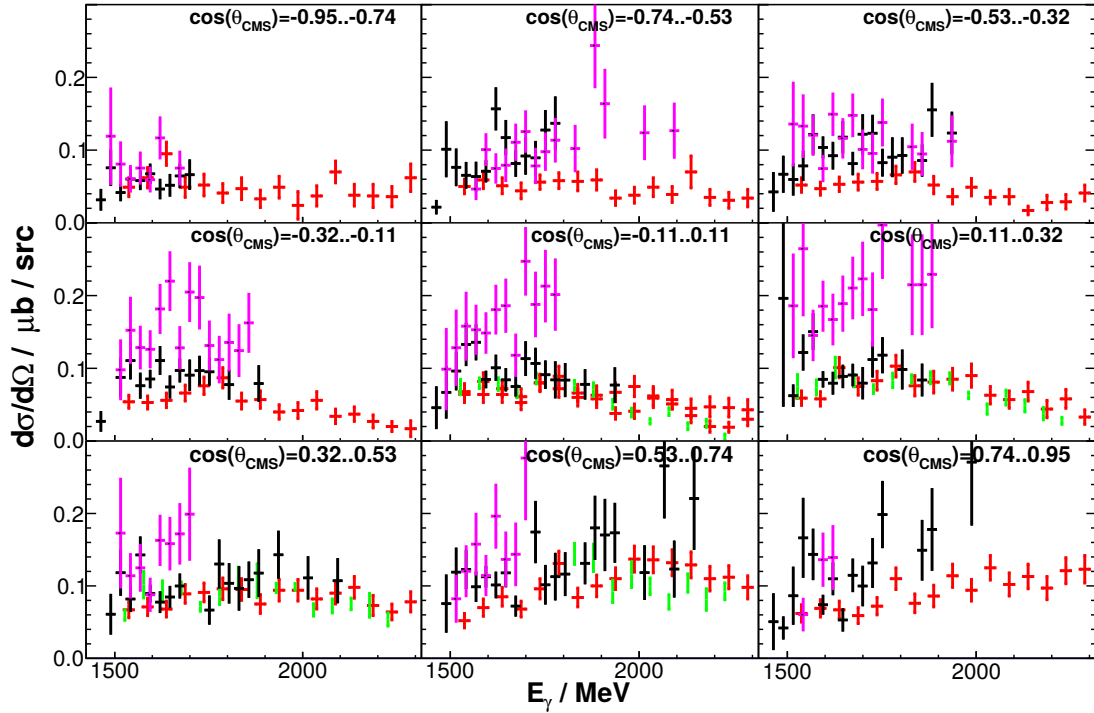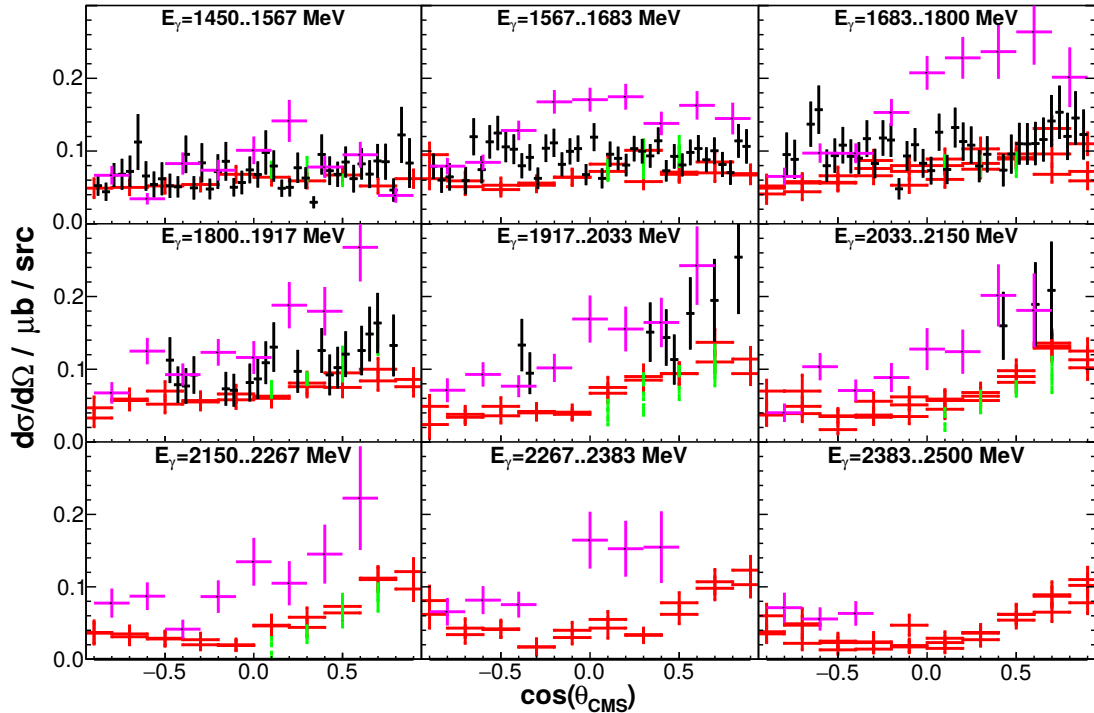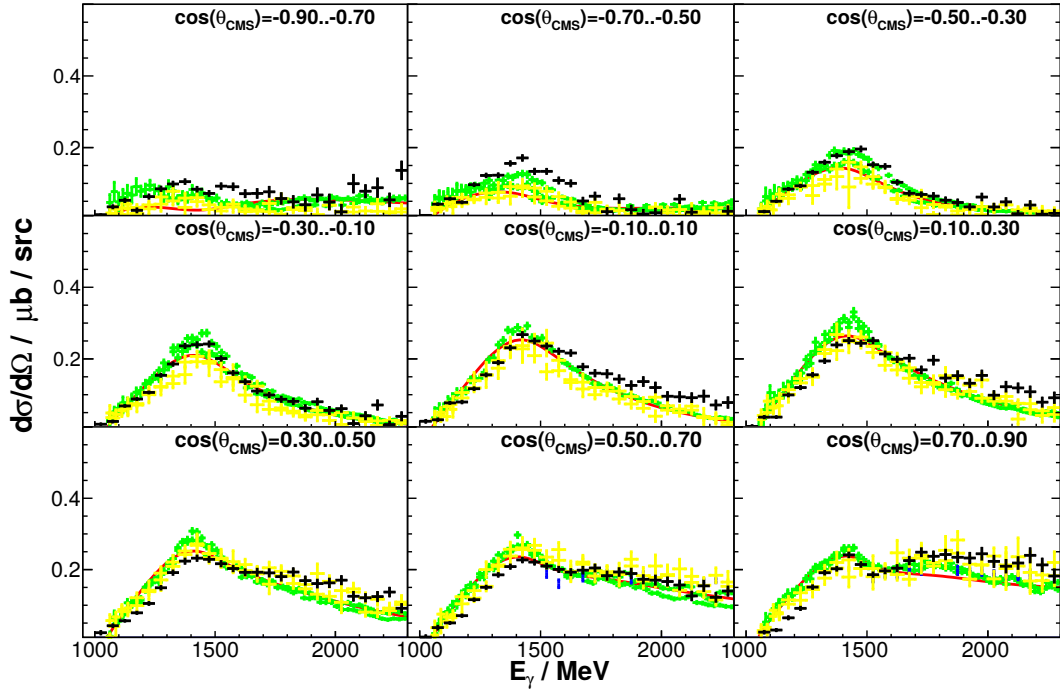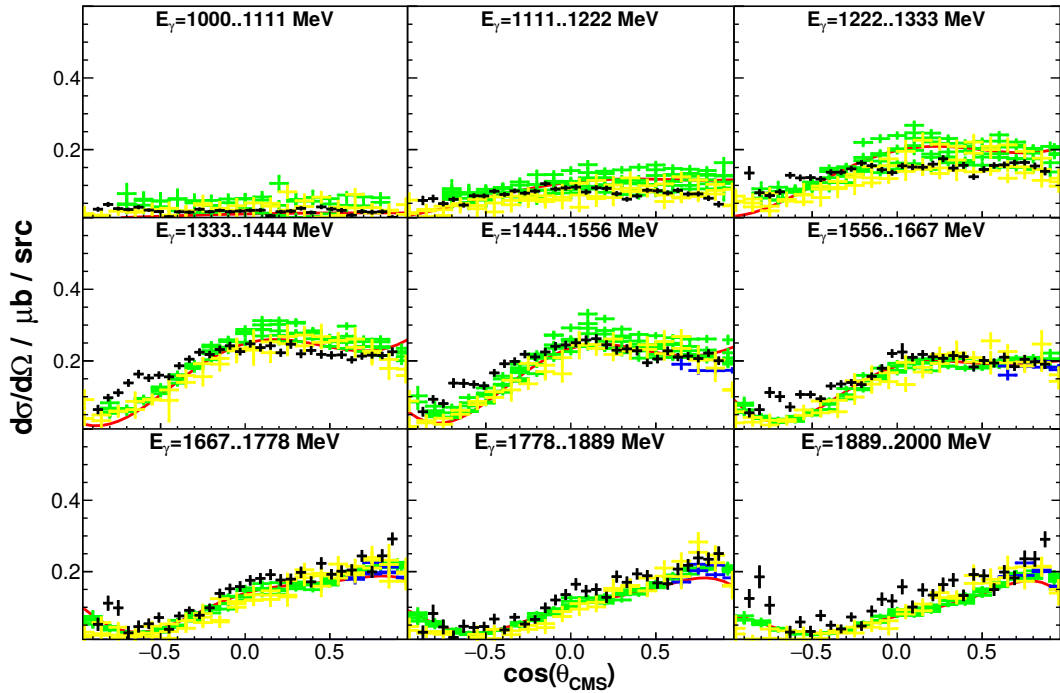
(a) Differential cross section for $\gamma p \rightarrow \eta p$ against initial photon energy E_γ.
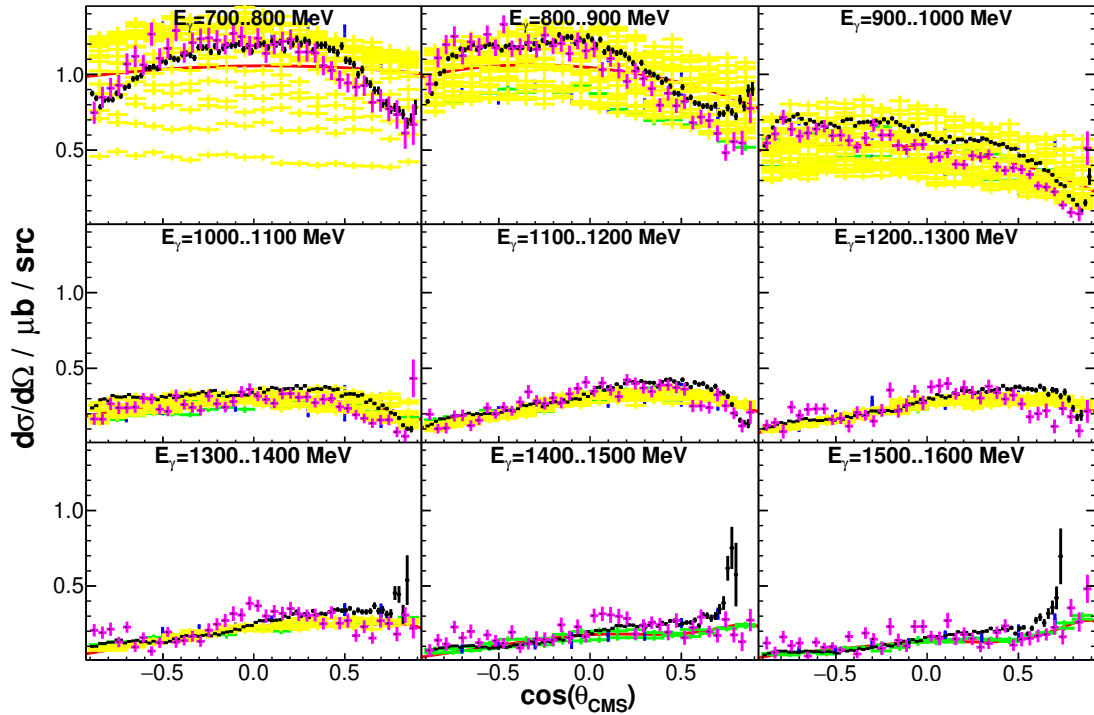
(b) Differential cross section for $\gamma p \rightarrow \eta p$ against cosine θ of the meson in the center of mass system.

Figure 5.16: Differential cross section for $\gamma p \rightarrow \eta p$ against initial photon energy E_γ (a) and against cosine θ of the meson in the center of mass system (b). The red line was taken from the Bonn-Gatchina Partial Wave Analysis Group [40]. Yellow data was measured at MAMI with the Crystal Ball experiment [41], green data points are from the Crystal Barrel experiment [42] and blue points are from the CLAS experiment [43]. Black points mark the identification of $\eta \rightarrow \gamma\gamma$ decay and magenta points mark the $\eta \rightarrow \pi^-\pi^+\pi^0$ decay in this thesis. External experimental data can have multiple entries if the angle range is larger then the original experiment.

(a) Differential cross section for $\gamma p \to \omega p$ against initial photon energy, E_γ.

(b) Differential cross section for $\gamma p \to \omega p$ against cosine θ of the meson in the center of mass system.

Figure 5.17: Differential cross section for $\gamma p \to \omega p$ against initial photon energy, E_γ (a) and against cosine θ of the meson in the center of mass system (b). The red data points were taken by the Crystal Barrel experiment [44], while the green points are from the CLAS experiment [45]. The black data points were determined from the $\omega \to \pi^0 \pi^- \pi^+$ decay and the magenta points are from the $\omega \to \pi^0 \gamma$ decay in this thesis. External experimental data can have multiple entries if the angle range is larger then the original experiment.

statement can be made for the results, however in most cases the $\eta\pi^+\pi^-$ decay agrees with other experimental data. With careful background subtraction, these data will complement existing data.

5.2.5 $\gamma p \rightarrow K^+\Sigma^0$

The Σ^0 is identified by the $\gamma\Lambda \rightarrow \gamma\pi^- p$ decay with a branching ratio of 63.9 %. The event identification is described in section 5.1.3. The results from other experiments and the Bonn-Gatchina solution mostly agree with the determined cross section. Some angular and beam energy bins show sudden jumps or drops in the cross section. In section 5.2.2 similar effects were seen originating from not fully understood detector acceptances. In this case, the K^+ could also be effected by acceptance gaps in a similar way to protons. This effect can only be investigated after the proton acceptance anomaly from section 5.2.2 and 5.2.3 is identified and corrected.

5.3 Estimated systematic errors

No studies were performed on the systematic errors in this analysis, but known errors and their estimation on the results are made here. The target in the analyzed data was 60 mm long. As seen in figure 2.5 the length of the target depends on the curvature of the mylar windows. This also assumes that the photon beam is centered. On the assumption of a small movement of the beam and a different window curvature, the target length could deviate by 1 mm. This would mean a constant offset in the cross section by around 1.7 %. A photon flux error would show similar behavior. For the photon flux the figure 4.12 can be used to estimate the effect. The figure shows the photon flux with the P_γ determined from GIM and FluMo. Comparing both methods shows a discrepancy by around 3 %, which is probably due to the statistical limitation of the FluMo photon efficiency determination and indicates that the FluMo calibration time should be increased in future data tacking. An identification efficiency error is difficult to estimate. It would result in offsets in the cross section depending on the angle of the particles and is mostly responsible for the structures in the $\pi^0 p$ cross section in figure 5.15(b). For E_γ =1056 MeV to 1167 MeV the cross section differs from the Bonn-Gatchina fit by almost 25 % independent on the identification method. This can be associated with differences in the geometry between reality and simulation and was confirmed in $\gamma p \rightarrow \eta p$ and $\gamma p \rightarrow \omega p$ to originate from protons with $\theta_{lab} = 6°$ to $12°$. Outside this particle acceptance the results agree well to other experiments, which suggests a small systematic error from the overall detector geometry. The event identification of $\pi^0 p$ with and without trigger simulation can also be used to estimate the error on the trigger simulation. It is expected that with high E_γ the identification of a π^0 always passes the trigger. As such the variation between blue and green points at high beam energy can be used to estimate that the trigger has an systematic error of about 2 %. The variation between green and black points on the other hand shows the kinematic fit systematic error mostly in the order of 5 % to 10 %. The confidence level distribution in figure 5.3(c) between real and simulated data already shows that a cut on this confidence level will result in a higher ratio of signal loss in real data compared to simulation. At last the signal extraction via RooFit may introduce a systematic error if the simulated signal shape is not represented in the real data. The data analyzed here showed only small differences to the simulated spectrum and the statistic error of the fit out weights the systematic errors. Therefore an error value below 5 % can be assumed. Table 5.3 gives a summery of the afore mentioned systematic errors. The total systematic error would sum up to 5 % to 28 % depending on the reaction kinematics, which is visible in some cross sections like ηp and ωp. In the future some systematic errors will be reduced with further analysis and a quantitative systematical error determination will be performed then.

(a) Differential cross section for $\gamma p \rightarrow \eta' p$ against initial photon energy E_γ.

(b) Differential cross section for $\gamma p \rightarrow \eta' p$ against cosine θ of the meson in the center of mass system.

Figure 5.18: Differential cross section for $\gamma p \rightarrow \eta' p$ against initial photon energy E_γ (a) and against cosine θ of the meson in the center of mass system (b). The red data points were taken by the Crystal Barrel experiment [42] and the green data is from the CLAS experiment [46]. Black points mark the $\eta' \rightarrow \eta \pi^+ \pi^- \rightarrow \gamma\gamma\pi^+\pi^-$ decay, while the magenta points are from the $\eta' \rightarrow \gamma\gamma$ decay in this thesis. External experimental data can have multiple entries if the energy range is larger.

(a) Differential cross section for $\gamma p \rightarrow K^+\Sigma^0$ against initial photon energy E_γ.

(b) Differential cross section for $\gamma p \rightarrow K^+\Sigma^0$ against cosine θ of the meson in the center of mass system.

Figure 5.19: Differential cross section for $\gamma p \rightarrow K^+\Sigma^0$ against initial photon energy E_γ (a) and against cosine θ of the meson in the center of mass system (b). Red line was taken from the Bonn-Gatchina Partial Wave Analysis Group [40]. The green data points are from the CLAS experiment [47], blue data points are from the LEPS experiment [48] and the yellow data points are from the Saphir experiment [49]. Black points were obtained by identification of the $K^+\Sigma^0 \rightarrow K^+\gamma\pi^- p$ decay in this thesis. External experimental data can have multiple entries if the angle range is larger.

	systematic error / %
target size	1.7
photon flux number	3
detector geometry (for θ_{lab} =6° to 12° particles)	2 - 25
trigger simulation	2
kinematic fit	2 - 10
RooFit	<5
total error	5 - 28

Table 5.3: Estimated systematic errors in the cross section determination. The total error is summed in quadrature.

5.4 Summary of benchmark cross section determinations

In this chapter the photoproduction cross section of γp to $\pi^0 p$, ηp, ωp, $\eta' p$ and $K^0 \Sigma^+$ were determined to check the performance of the BGO-OD detector. In most cases and kinematic situations the BGO-OD experiment agrees to the results of other experiments. Specific θ angles and E_γ beam energies show some deviations.

If the photon flux determined in section 4.2 was not correct, the cross section would be always higher or lower than other experiments but would be angular independent. This seems not to be the case, thus one can conclude that the photon flux is correct within the statistical errors of the cross section. This also applies to the target area density. The effect should be independent of beam energy and meson angle.

The event extraction, via fitting simulated mass distributions, performs well and yields good results. This shows that the detector positions and resolutions agree to the simulation, as deviations would result in distorted mass distributions.

The determination of the identification efficiency used to correct the measured reaction number depends on an accurate geometry representation in the simulation. The determined cross sections show small deviations from other experimental data. The origin of this is most likely the detector geometry. Results from ωp and ηp show that in both cases the largest deviation originates from protons with θ angle 6° to 12°. This region is covered by two detectors, which seem to not be represented correctly in the simulation. These anomalies will be addressed and adjusted.

Photoproduction of $\Lambda(1405)$
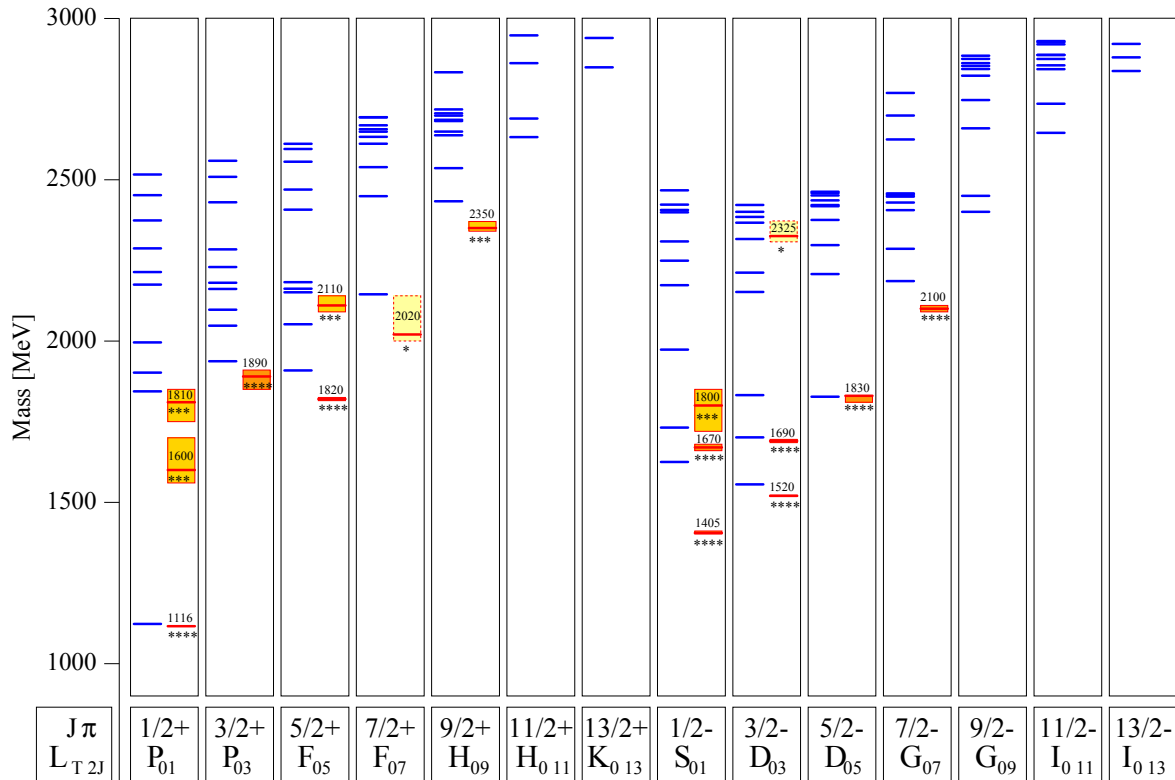
Figure 6.1: Blue line mark the calculated positive- and negative parity spectrum of Λ with *uds*-quarks. The resonances are ordered by total spin J and parity π. Next to the calculated line the experimentally found resonances in the Particle Data Group [3] are shown by a red line with a box around it for uncertainty[50].

It was outlined in the introduction that there are two types of nonexotic hadrons. Mesons with two and baryons with three valence quarks. For a better understanding of the degrees of freedom and intreactions of the constituents, scattering experiments were performed to identify baryon resonances and measure their widths and decay parameters. Constituent quark models, where dressed quarks interact via a mutually generated potential are used to describe baryon resonant spectra. In such
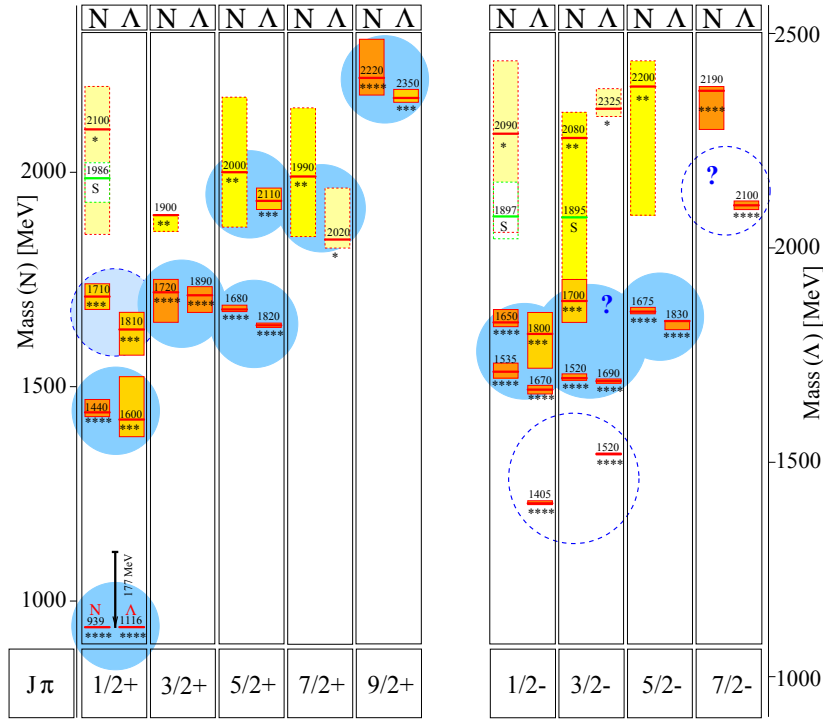
Figure 6.2: Comparison between experimentally found nucleon and Λ resonances. The resonances are ordered by their total spin *J* and parity *π*. The nucleon states are left, while the Λ states are right inside one bin. The nucleon and Λ spectrum have an offset of 177 MeV to have the ground states align to each other. [50]

models, quarks often do not couple to the continuum. The calculated states have thus no information of width or decay modes. Measured and predicted resonant Λ states are shown in figure 6.1. The Λ baryons consist of *uds*-quarks with isospin *I* = 0. A lot of predicted states have not been found experimentally. Most of these missing states are higher excitations. The width of the experimentally found states increase with energy, as such it is possible that the missing higher energy states have a large width which makes them difficult to identify. However not all experimentally found states fit the model predictions. This could mean that the quark model is not complete and the used approximations are not valid. Λ(1405) is one of these states. With total spin *J* = 1/2 and negative parity, the measured mass is far lower than the lowest predicted level with these quantum numbers. The lowest $J^P = 1/2^-$ nucleon state, *N*(1535), has a mass of 1535 MeV. The Λ(1405) has the same quantum numbers with the exception that one light quark is exchanged with a strange quark. The mass of the Λ(1405) is 130 MeV lighter, even though the mass of the strange quark is heavier. Comparing the nucleon and Λ spectrum in figure 6.2, most experimental found states have a mass partner shifted by 177 MeV to account for the heavier strange quark. Again the Λ(1405) seams to be an exception with no mass partner.

During the discovery of the Λ(1405) it was found that the invariant mass distribution was distorted, as seen in figure 6.3. At that time it was already speculated that Λ(1405) could be a molecular state between a nucleon and anti-kaon [58]. The bounding force for such a structure would be the residual strong force, comparable to the van der Waals force in electromagnetism. The Yukawa potential describes an interaction between nucleons where the proton changes to a neutron and vice versa via charged pion exchange. In such cases a *n* − *p* nucleon system would change to *p* − *n*. In case of the
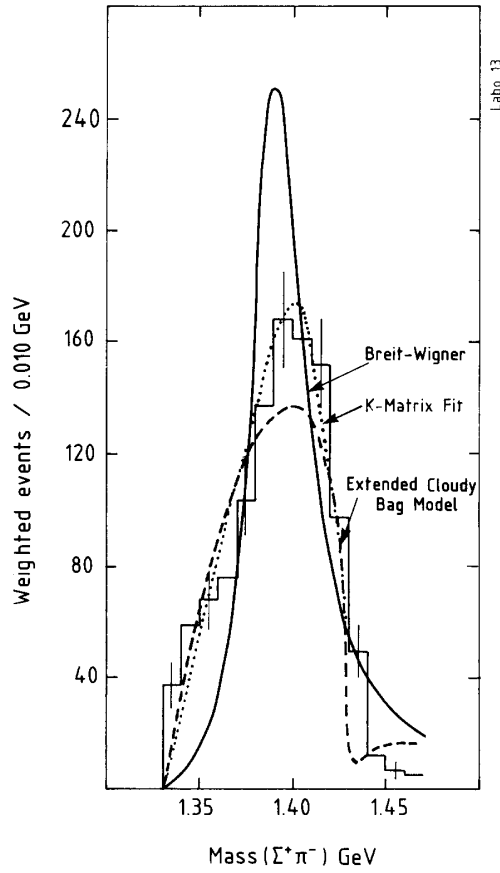
Figure 6.3: Invariant mass distribution of $\Sigma^+\pi^-$ system from the reaction $K^-p \to \Sigma^+\pi^-\pi^+\pi^-$ at 4.2 GeV/c. The curves represent models described in the paper.[51]
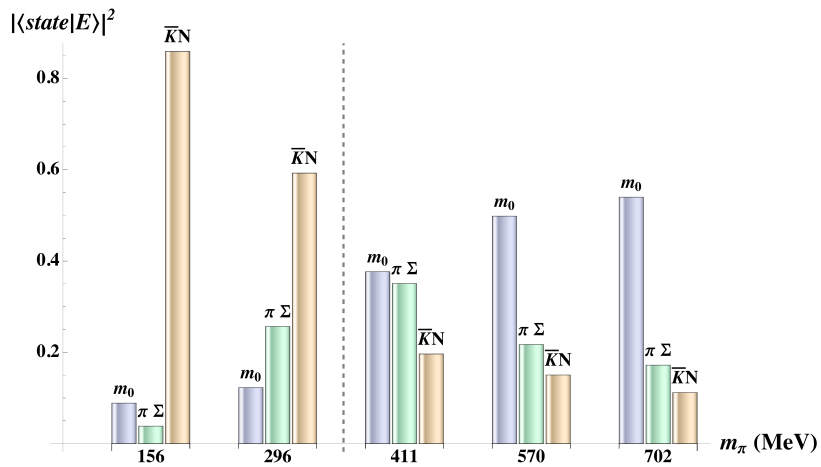
Figure 6.4: Lattice QCD calculations illustrating the composition of $\Lambda(1405)$ depending on the π^0 mass [7]. The compositions options are single particle state m_0, and the two particle states $\pi\Sigma$ and $\bar{K}N$.
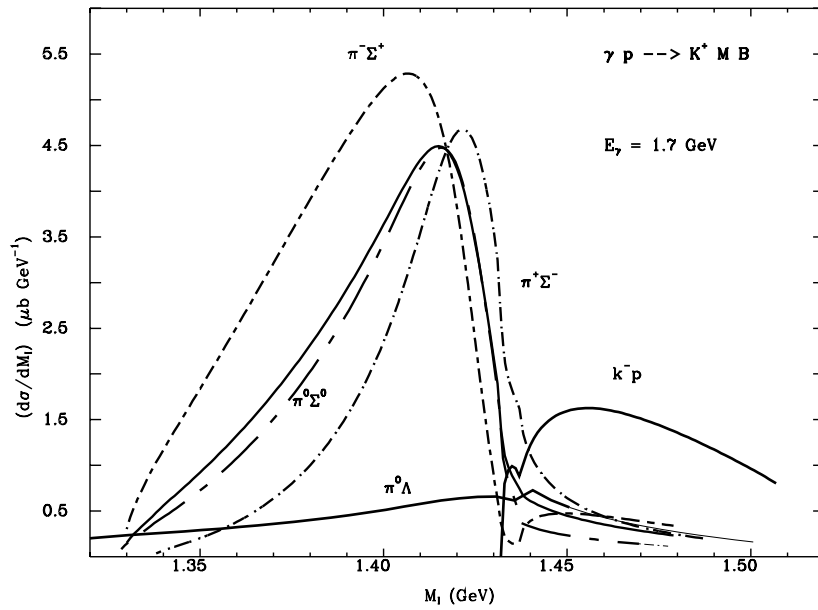
Figure 6.5: Mass distribution for the different channels. The solid lines mark $\pi^0\Lambda$, K^-p and $\Sigma\pi$ channels. The single decay modes of $\Lambda(1405)$ are shown by the dashed lines. [52]
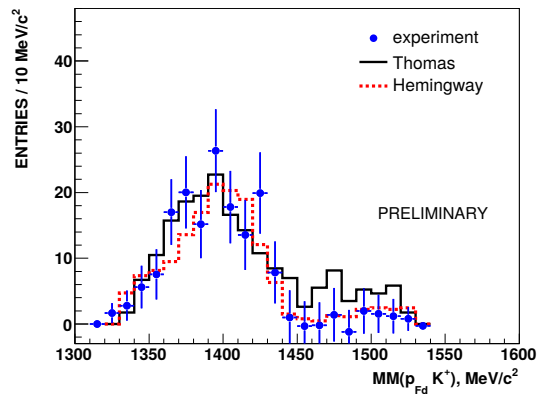
Figure 6.6: The background-subtracted line shape of the $\Lambda(1405)$ decaying into $\Sigma^0\pi^0$ (points) at the ANKE experiment.[53] The black and red line show the bubble chamber results of older experiments.

(a) $X \to \Sigma^+ \pi^-$

(b) $X \to \Sigma^- \pi^+$
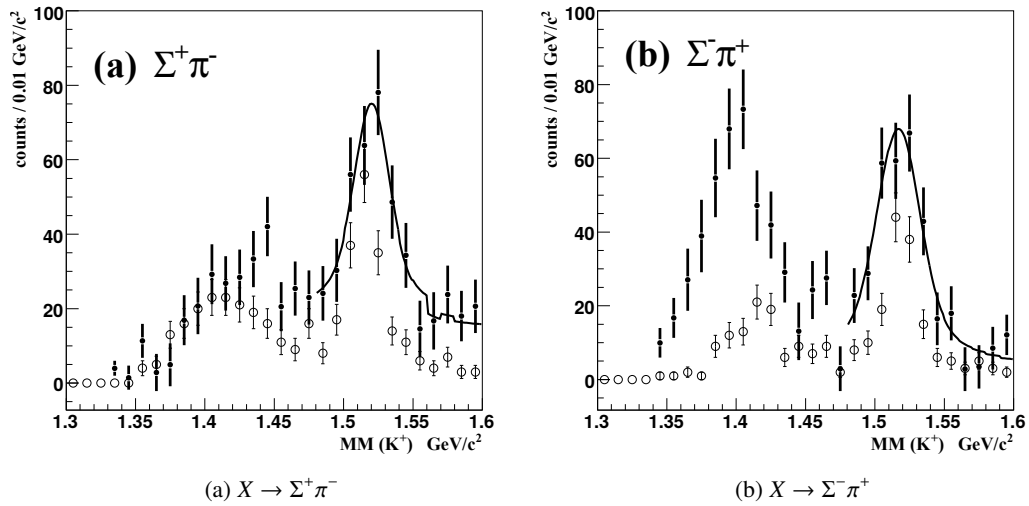
Figure 6.7: Missing mass of the $\gamma p \to K^+ X$ reaction measured by the LEPS experiment[54]. Open circles show the results from a previous analysis of the data, while closed circles are the new results of the LEPS experiment.
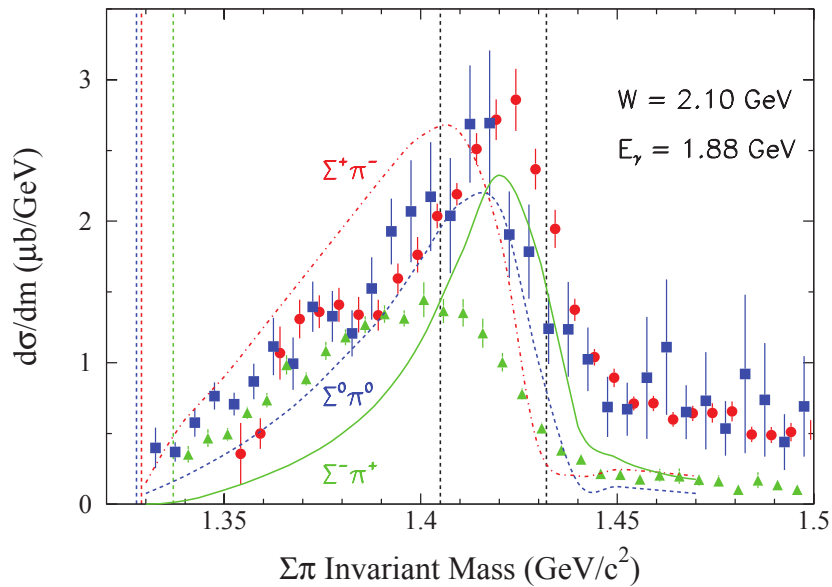
Figure 6.8: $\Sigma\pi$ mass distributions at $E_\gamma = 1.88$ GeV measured by the CLAS experiment [55][56][57] in comparison to the model of Nacher et al.[52] scaled by a factor of 2.0. The green line shows the $\pi^+\Sigma^-$, red line the $\pi^-\Sigma^+$ and blue line the $\pi^0\Sigma^0$ decay. The dashed lines represent the individual models for the decay modes.

Λ(1405) the $K^- - p$ molecule would change to a $\overline{K^0} - n$ molecule via the same pion exchange. Further support for the molecular structure of Λ(1405) is found with a lattice QCD calculation [7], seen in figure 6.4. The calculation depends on the used π mass. Going from heavy to the realistic π masses, the antikaon-nucleon molecule Fock state dominates the wave function for Λ(1405).

The distorted shape of the invariant mass distribution, called line shape, can be explained by an antikaon-nucleon molecule composition of Λ(1405). The antikaon and nucleon could be produced in the bound system below the free antikaon nucleon production threshold of 1432 MeV. Above this threshold the antikaon and nucleon can be produced free, reducing the cross section for the bound Λ(1405) system and consequently a sudden cut-off in the line shape. A calculation within a dynamical coupled-channel model which respects chiral symmetry of quantum chromodynamics (QCD) and the unitarity of the scattering amplitude shows that the structure of the Λ(1405) resonance is described as a superposition of two independent states [59][60][61][62]. A study using a chiral unitary model, where the resonance is generated dynamically from $K^- p$ interaction with other channels constructed from the octets of baryons and mesons, shows that the line shape would depend on the decay mode, as seen in figure 6.5.

Apart from bubble chamber experiments, the asymmetrical line shape was confirmed by the ANKE experiment [63], as seen in figure 6.6. First measurements with photoproduction of the different Λ(1405) decay modes was performed by the LEPS experiment[54], shown in figure 6.7. The CLAS experiment measured all decay modes, as seen in figure 6.8. Comparing both measurements shows a discrepancy. In the LEPS data the $\Sigma^+\pi^-$ final-state peaks in lower energies than the $\Sigma^-\pi^+$ decay. Closer inspection reveals that this is opposite for the CLAS data. Comparing both data sets to the line shape predictions in figure 6.5 the LEPS data shows better agreement.
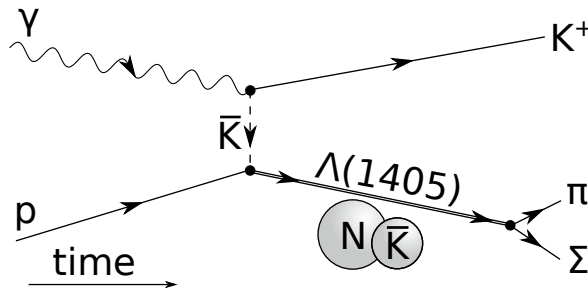
Figure 6.9: Possible photoproduction scheme of the Λ(1405) molecule. Time propagates from left to right.

The BGO-OD experiment is complementary to the CLAS experiment, allowing detection of extremely forward charged particles. Figure 6.9 shows the photoproduction of Λ(1405) in the assumption of a molecular state. If the K^+ from the $\gamma p \rightarrow K^+ \Lambda(1405)$ reaction is detected in the forward spectrometer, the transfered momentum to the Λ(1405) is small. On the assumption of an exotic $N\bar{K}$ molecule as the Λ(1405) structure, the cross section would favor kinematics where the momentum in the molecule is minimal. In this case the BGO-OD experiment is well suited to investigate Λ(1405). The main difficulty for all experiments in the investigation of Λ(1405) is the Σ(1385), which has similar mass and decay modes. The Λ(1405) hyperon exclusively decays to $\Sigma\pi$. The main decay modes of Σ(1385) are $\Lambda\pi$ with 87 % branching ratio and $\Sigma\pi$ with 11.7 %. The decay $\Sigma(1385)^0 \rightarrow \Sigma^0\pi^0$ is strictly prohibited by isospin symmetry.

In this chapter, the $\pi^0\Sigma^0$ decay is used to extract the line shape and differential cross section of Λ(1405). A list of hyperons which are seen in our analysis can be found in table 6.1. Identifying the K^+ and π^0 is sufficient to identify the reaction, as the missing mass to both particles can be used to identify

baryon	mass / MeV	decay modes	branching ratio / %
Λ	1115.7	$p\pi^-$	64
		$n\pi^0$	36
Σ^0	1192.6	$\Lambda\gamma$	100
Σ^+	1189.4	$p\pi^0$	52
		$n\pi^+$	48
Σ^-	1197.4	$n\pi^-$	100
$\Sigma(1385)^0$	1384	$\Lambda\pi^0$	87
		$\Sigma^+\pi^-$	6
		$\Sigma^-\pi^+$	6
$\Lambda(1405)$	1405	$\Sigma^0\pi^0$	33
		$\Sigma^+\pi^-$	33
		$\Sigma^-\pi^+$	33
$\Lambda(1520)$	1520	$\Sigma^0\pi^0$	14
		$\Sigma^+\pi^-$	14
		$\Sigma^-\pi^+$	14
		$N\bar{K}$	45

Table 6.1: Hyperons and their decay modes used in the analysis [3]. The branching ratios are rounded.

the Σ^0. This is only possible when the K^+ is detected in the forward spectrometer, as the particle identification can be performed using time of flight and momentum information. There are therefore two main analysis procedures. The analysis when kaons are not detected in the forward spectrometer is described in section 6.1.1, while the analysis with kaons in the forward spectrometer is identified in section 6.1.2. The line shape measurement is discussed in section 6.2 and the extracted cross section in section 6.3.

6.1 Event identification

The identification of the $\Lambda(1405) \to \pi^0\Sigma^0$ decay is described in this section. The Σ^0 is identified via the $\gamma\Lambda \to \gamma\pi^- p$ decay (64 % branching ratio) in section 6.1.1. In section 6.1.2 the Σ^0 is identified via the missing mass technique. In this case the K^+ is detected in the forward spectrometer, which allows particle identification.

6.1.1 $\gamma p \to K^+\Lambda(1405) \to K^+\pi^0\Sigma^0 \to K^+3\gamma\pi^- p$

The event identification is similar to the $K^+\Sigma^0$ identification in section 5.1.3. Adding a pion to the final-state results in the $K^+\pi^0\Sigma^0$ state, which is used to identify the $\Lambda(1405) \to \pi^0\Sigma^0$ decay. $\Sigma(1385)$ does not decay into this state, but due to cluster split-off or noise inside the BGO, the $\Sigma(1385)^0 \to \pi^0\Lambda$ and $\Sigma(1385)^0 \to \pi^-\Sigma^+$ decays lead to background contributions in the event sample. All the analysis steps which are similar to the $K^+\Sigma^0$ identification will be not discussed here again. The following analysis steps which were performed after the kinematic fit are specific to the $\Lambda(1405)$ analysis.
In figure 6.10 the theta distribution of the γ from the $\Sigma^0 \to \gamma\Lambda$ decay is shown for simulated signal and background channels. The background distribution shows a high probability at $\theta < 35°$ angles compared to signal. This difference can be used to suppress combinatorial background in the

identification. Photons with θ angle of lower then 35° are ignored in the analysis. The reduction in background can be seen in the invariant mass of $\gamma\Lambda$ in figure 6.11. The signal can be identified by the Σ^0 hyperon peak in the $\gamma\Lambda$ mass. After applying the restriction on the photon θ angle the signal to background ratio is improved. A part of signal is lost due to this cut, but the improved signal to background ratio allows for more accurate signal extraction later in the analysis.

For the signal extraction, not only the invariant mass of $\pi^0\Lambda\gamma$ is used, which should form the $\Lambda(1405)$, but also the $\Lambda\gamma$ mass for Σ^0 identification. The real data is shown in figure 6.12, where the $\Lambda\gamma$ mass is plotted against the $\pi^0\Lambda\gamma$ mass. On top of a high combinatorial background the peak for the $\Lambda(1405)$ can be seen at around $|\Lambda\gamma| = 1200\,$MeV and $|\pi^0\Lambda\gamma| = 1400\,$MeV. The $\Lambda(1520)$ also decays into the same final-state and a corresponding peak can also be seen. In figure 6.13 the invariant mass of $\Lambda\gamma$ is plotted against the $\pi^0\Lambda\gamma$ mass for simulated $\Lambda(1405)$, $\Lambda(1520)$ and $\Sigma(1385)$ hyperons. It shows the different mass distributions for the hyperons. While it is expected for the $\Lambda(1405)$ and $\Lambda(1520)$ to pass the selection cuts, the $\Sigma(1385)$ should be suppressed, as it does not decay in the same final-state. In this case the $\Sigma(1385) \to \Lambda\pi^0 \to p\pi^-\pi^0$ and $\Sigma(1385) \to \Sigma^+\pi^- \to p\pi^0\pi^-$ decay pass the selection cuts, as an additional signal in the BGO is identified

Figure 6.10: θ distribution for γ in the $\Sigma^0 \to \gamma\Lambda$ decay from the $K^+\Lambda(1405) \to K^+\pi^0\Sigma^0$ reaction. Black shows the distribution for free $\gamma p \to \pi^0\Lambda$ production, while red marks the $\Lambda(1405)$ simulation.

through backscattering, clustering errors or noise in the detector. Plotting the $\Lambda\gamma$ against $\pi^0\Lambda\gamma$ mass, the $\Lambda(1405)$ and $\Lambda(1520)$ can be easily distinguished from the $\Sigma(1385)$ distribution.

(a) No Cut

(b) Reject γ with $\theta < 35°$
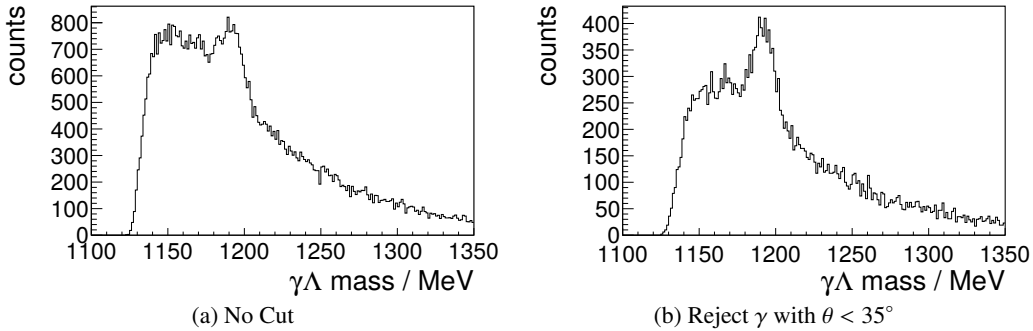
Figure 6.11: Invariant mass of $\gamma\Lambda$ in the $\gamma p \to K^+\Lambda(1405) \to K^+\pi^0\Sigma^0$ reaction before and after angle selection cut on the photons.

If the subtraction of $\Sigma(1385)$ is not handled carefully, the line shape of $\Lambda(1405)$ may be influenced. The $\Lambda\gamma\pi^0$ invariant mass with $\Lambda\gamma$ mass smaller then Σ^0 can be used to determine the $\Sigma(1385)$ contribution. To subtract the background contributions, the signal extraction is performed with a two dimensional fit via RooFit which uses the 2D plots in figures 6.13 to fit to the real data in figure 6.12.

The events surviving all selection cuts are used to extract the $\Lambda(1405)$ line shape in section 6.2 and differential cross section in section 6.3. The fit to extract the yield is described in the corresponding sections.
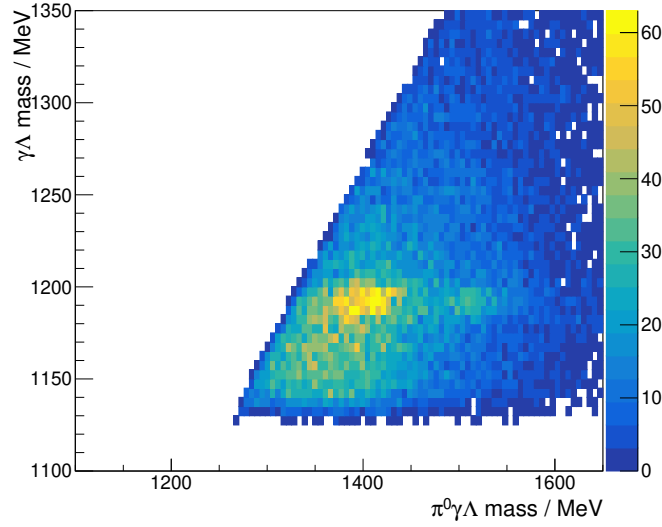
Figure 6.12: Invariant mass of $\pi^0\gamma\Lambda^0$ vs $\gamma\Lambda$ invariant mass in the $\gamma p \to K^+\Lambda(1405) \to K^+\pi^0\Sigma^0$ identification with real data. For this the running periods of 2015 and 2017 with hydrogen target were used.
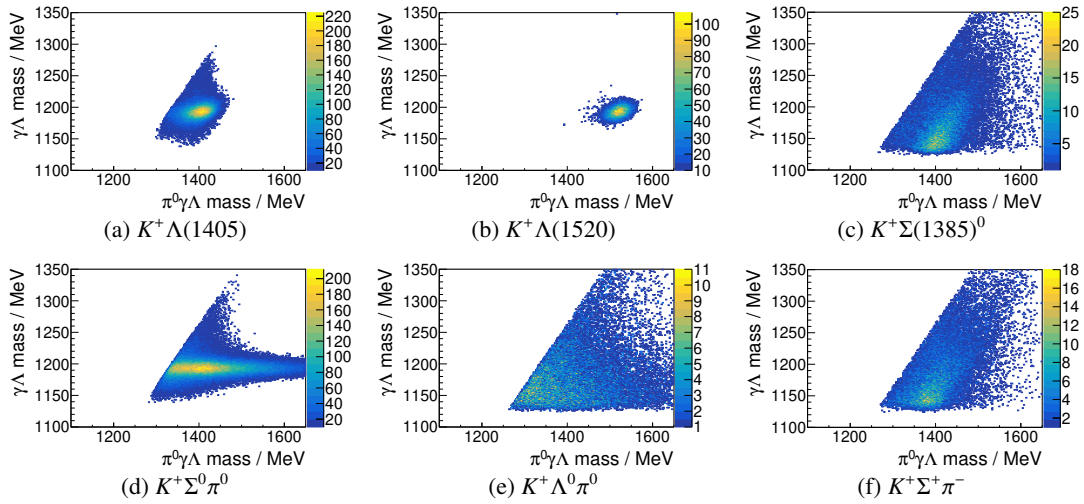
Figure 6.13: Simulated data showing invariant mass of $\pi^0\gamma\Lambda^0$ vs $\gamma\Lambda$ invariant mass in the $\gamma p \to K^+\Lambda(1405) \to K^+\pi^0\Sigma^0$ identification. Each plot shows only one simulated channel, described in the sub-caption of the figure.

6.1.2 $\gamma p \to K^+\Lambda(1405) \to K^+\pi^0 X$, with K^+ in forward spectrometer

In this analysis the K^+ is identified in the forward spectrometer, while a π^0 is identified in the BGO calorimeter. The Σ^0 is identified via the missing mass to the detected particles. Section 2.3.7 described the particle identification of the forward spectrometer in more detail. The π^0 is identified in the BGO calorimeter from its $\gamma\gamma$ decay. The missing mass to $K^+\pi^0$ is plotted against missing mass to K^+ in figure 6.14. The prominent peak for |missing mass to $K^+\pi^0$| =1115 MeV and around |missing mass to K^+| =1400 MeV originates from the $\Sigma(1385)$.

The shape of the mass distribution can be modeled using simulated data and fitted. The resulting
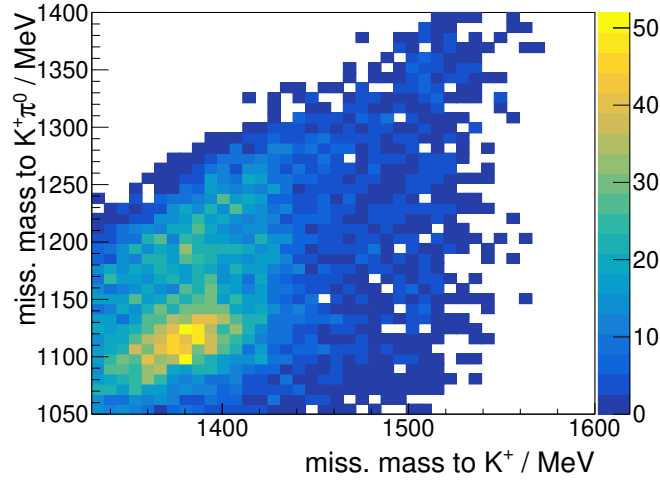
Figure 6.14: Missing mass to $K^+\pi^0$ against missing mass to K^+ with E_γ =1530 MeV to 1830 MeV and $\cos(\theta_{CMS})$ =0.8 to 1.
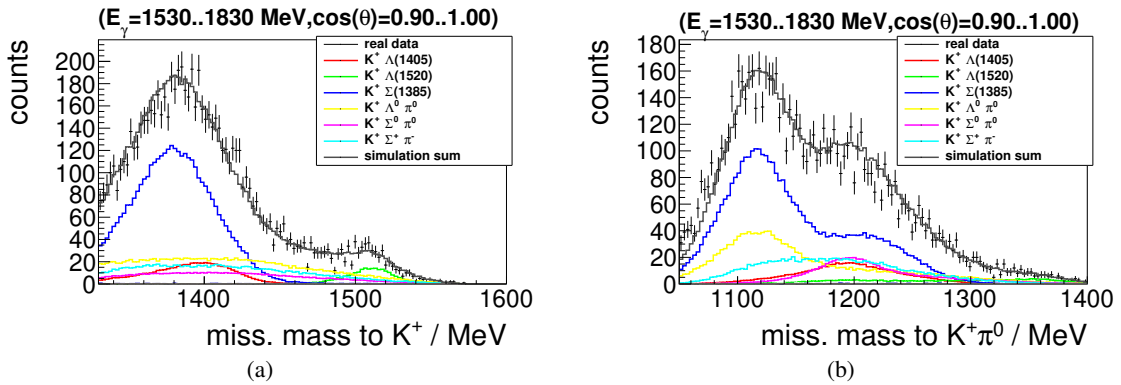
Figure 6.15: Missing mass to K^+ and missing mass to $K^+\pi^0$ in the $\gamma p \rightarrow K^+\Lambda(1405) \rightarrow K^+\pi^0\Sigma^0$ reaction signal extraction. Black points mark the real data, while the colored contributions are simulated.

two-dimensional fit to the data is shown in one-dimensional projections in figure 6.15. $K^+\Sigma^0\pi^0$, $K^+\Lambda\pi^0$, $K^+\Sigma^+\pi^-$, $K^+\Sigma(1385)$, $K^+\Lambda(1405)$ and $K^+\Lambda(1520)$ final-states were used to describe the data. Fit results show that the $\Sigma(1385)$ has the highest contribution to the data distribution. Free $\pi^0\Lambda$ production shows a similar distribution in the missing mass to $K^+\pi^0$, but no peak at 1400 MeV, unlike the $\Sigma(1385)$. The $\Lambda(1405)$ only contributes little to the overall distribution and explains why it could not be seen in figure 6.14. The line shape is extracted in section 6.2.2, and the differential cross section shown in section 6.3.

6.2 $\Lambda(1405)$ line shape extraction

After the analysis steps described in section 6.1, the line shape of $\Lambda(1405)$ is extracted. The extraction is different for the two reaction reconstructions. The reconstruction detecting all particles is explained in section 6.2.1, while the K^+ forward analysis in section 6.2.2. In section 6.2.3 the results are

compared to other experimental measurements.

6.2.1 $\gamma p \rightarrow K^+ \Lambda(1405) \rightarrow K^+ \pi^0 \Sigma^0 \rightarrow K^+ 3\gamma\pi^- p$

The line shape of the $\Lambda(1405)$ was extracted from events with the K^+ produced in the angular range $\cos(\theta_{CMS})$ =−1.0 to 0.8 and beam energy range E_γ =1500 MeV to 2300 MeV. The signal extraction for the line shape is handled differently to the differential cross section determination. The $K^+\Lambda(1405)$, $K^+\pi^0\Sigma^0$, $K^*\Sigma^0$ and $K^+\Lambda(1520)$ simulations were not used in the fit, to remove the possibility of influence on the line shape. The two-dimensional plot with all data, as seen in figure 6.16, is taken and the $\gamma\Lambda$ mass from 1166.5 MeV to 1217.0 MeV is excluded. This removes reactions with a Σ^0 in the final-state from the data set and only a background distribution remains. Now a two-dimensional fit is used to describe the background distribution. The $\gamma\Lambda$ projection can be seen in figure 6.17. The data in black shows a clear peak for the Σ^0 hyperon, while the colored lines show different simulated reactions. The mass between 1166.5 MeV to 1217.0 MeV was not used in the fit, as such no peak for the Σ^0 is seen in the summed simulated distribution. Figure 6.18(a) shows the $\gamma\Lambda\pi^0$ mass projection of the two dimensional fit. The background distribution in both projections is well described by the simulated data. The data with $\gamma\Lambda$ mass of 1166.5 MeV to 1217.0 MeV not used in the two-dimensional fit is shown in figure 6.18(b). The simulated distribution shows the extrapolated fit results from the two-dimensional fit. After subtracting the background the line shape can be seen in figure 6.19. The $\Lambda(1405)$, $\Lambda(1520)$ and the uncorrelated $\Sigma^0\pi^0$ production were not included in the fit, thus the remaining data should mainly consist of these reactions. The uncorrelated $\Sigma^0\pi^0$ production is indicated by the red points and was adjusted to describe the flat distribution below the peaks. The $\Lambda(1405)$ line shape shows two structures. A peak at around 1390 MeV and a cusp at 1425 MeV suggest a line shape more complex than observed in other experiments, which is discussed in more detail in section 6.2.3.
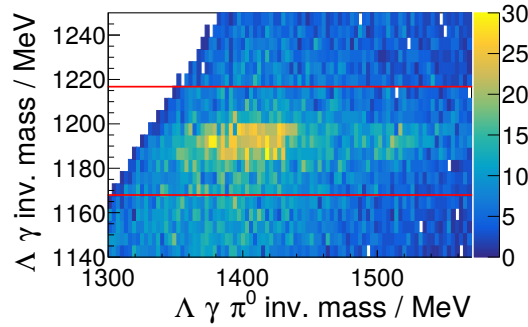
Figure 6.16: Invariant mass of $\pi^0\gamma\Lambda$ distribution in the $\gamma p \rightarrow K^+ \Lambda(1405) \rightarrow K^+\pi^0\Sigma^0 \rightarrow K^+\pi^0\gamma\Lambda$ reaction for E_γ =1500 MeV to 2300 MeV and $\cos(\theta_{CMS})$ =−1 to 0.8. Data between the red lines was excluded from the fit.

6.2.2 $\gamma p \rightarrow K^+ \Lambda(1405) \rightarrow K^+ \pi^0 X$, with the K^+ in the forward spectrometer

The line shape of $\Lambda(1405)$ with the K^+ in the forward spectrometer can not be extracted the same way as in section 6.2.1. The complete data is fitted, as already shown in figure 6.15. After that the line shape is extracted by subtracting all fitted simulated distributions from the real data with the exception of $\Lambda(1405)$ and $\Lambda(1520)$. The remaining data with missing mass to $K^+\pi^0$ in the range 1152 MeV to
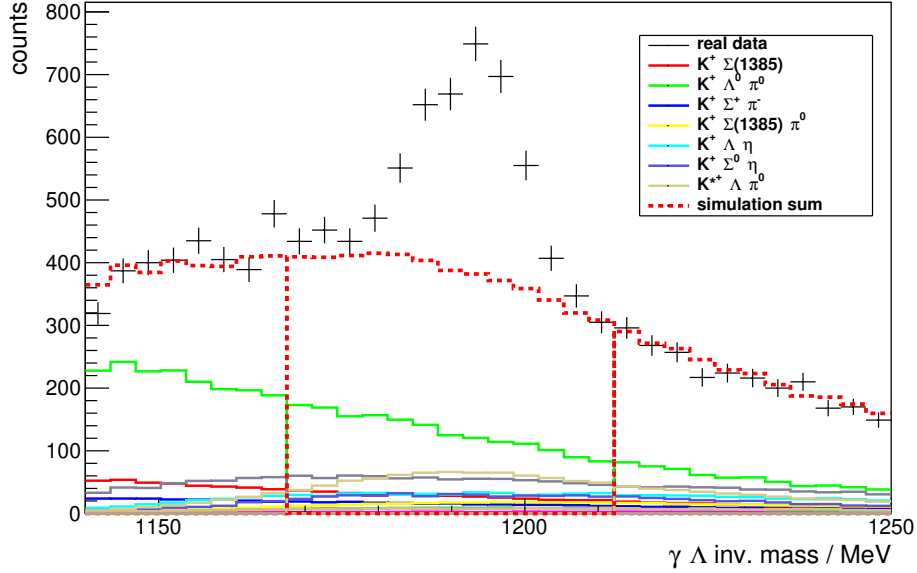
Figure 6.17: Invariant mass of $\gamma\Lambda$ distribution for E_γ =1500 MeV to 2300 MeV and $\cos(\theta_{CMS})$ =−1 to 0.8. The black points mark the real data, while the colored points mark different simulated channels. The mass 1166.5 MeV to 1217 MeV is excluded from the fit.

(a) 1166.5 MeV < $\gamma\Lambda$ mass > 1217.0 MeV

(b) 1166.5 MeV > $\gamma\Lambda$ mass < 1217.0 MeV
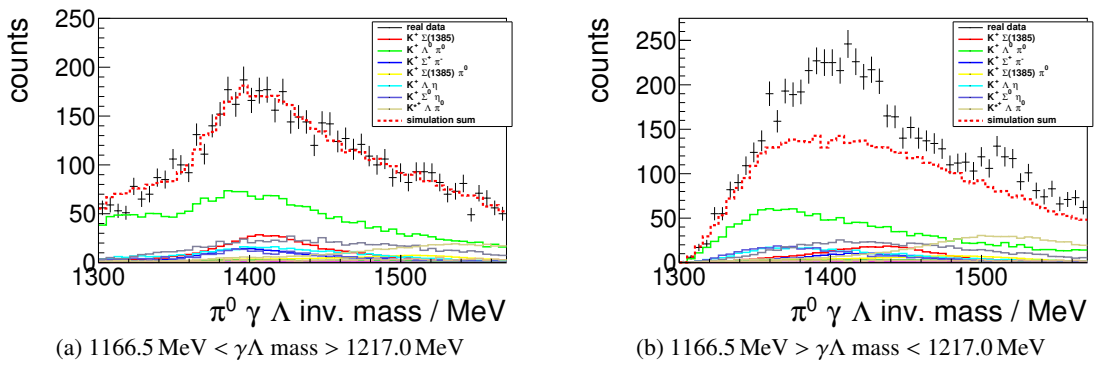
Figure 6.18: Invariant mass of $\pi^0\gamma\Lambda$ distribution for E_γ =1500 MeV to 2300 MeV and $\cos(\theta_{CMS})$ =−1 to 0.8. The black points mark the real data, while the colored points mark different simulated channels projected from the two dimensional RooFit on figure 6.16 .
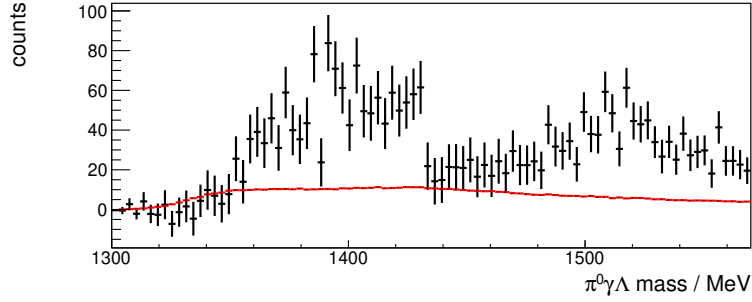
Figure 6.19: Invariant mass of $\pi^0\gamma\Lambda$ distribution for E_γ =1500 MeV to 2300 MeV. The black points mark the real data, while the red points mark the fitted simulated $\pi^0\Sigma^0$ uncorrelated production.

1239 MeV are selected to ensure the $\gamma p \rightarrow K^+\pi^0\Sigma^0$ reaction. This wide selection cut is necessary due the correlation between missing mass to $K^+\pi^0$ and missing mass to K^+, and ensures that the line shape will not be cut-off on any side artificially. In figure 6.20 the data in black before subtraction is shown together with the fitted background in red. After subtraction the $\Lambda(1405)$ line shape can be seen in figure 6.21, it is compared to other results in the following section 6.2.3.
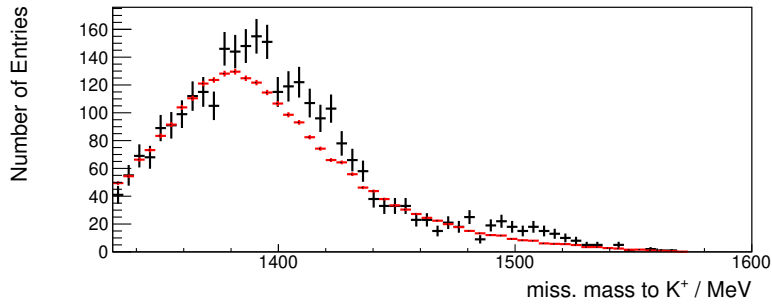
Figure 6.20: Missing mass to K^+ for missing mass to $K^+\pi^0$ in the range 1152 MeV to 1239 MeV for E_γ =1530 MeV to 1830 MeV and $\cos(\theta_{CMS})$ =0.8 to 1. The black points mark the real data, while the red points mark the sum of all possible fitted reactions with the exception of $K^+\Lambda(1405)$ and $K^+\Lambda(1520)$.

6.2.3 Line shape results

The $\Sigma^0\pi^0$ line shape determined in this section was achieved by two different methods. The first method used the completely detected final-state of the decay in section 6.1.1, while the second method used the K^+ particle identification in the forward spectrometer and the π^0 in the BGO calorimeter. In figure 6.22 both results are plotted in comparison. To reduce the point-to-point fluctuations, the data was rebinned and the scale of the distributions were adjusted for better comparison. Both results agree that at around 1430 MeV the line shape drops rapidly. This agrees with other experimental data, which may support the $\bar{K}N$ threshold effect in the production of $\Lambda(1405)$ as an dynamically generated state. In both analyses, the $\Lambda(1520)$ was not subtracted to ensure consistency, and was used as a quality check of the background subtraction.

The results are plotted with the results from the ANKE and CLAS experiments in figure 6.23. Here
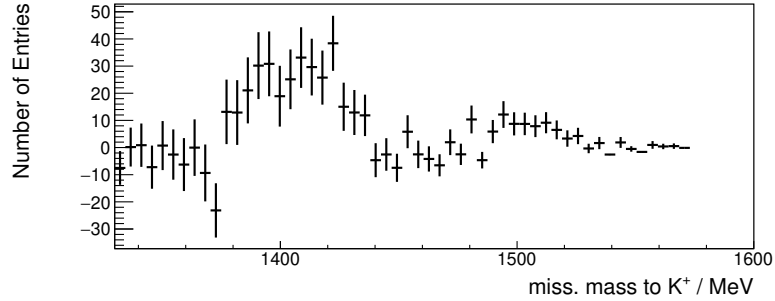
Figure 6.21: Missing mass to K^+ after subtraction of simulated reactions for missing mass to $K^+\pi^0$ in the range 1152 MeV to 1239 MeV for E_γ =1530 MeV to 1830 MeV and $\cos(\theta_{CMS})$ =0.8 to 1.
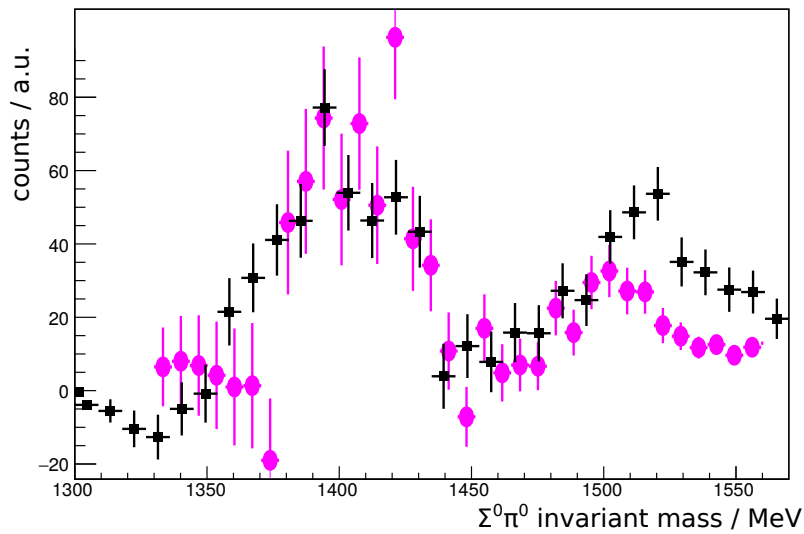
Figure 6.22: Line shape of the Λ(1405) in the $\Sigma^0\pi^0$ decay. Black points mark in this thesis determined line shape with the complete detection of the final-state particles, while the magenta points show the K^+ in the forward spectrometer and a π^0 only identification. The height of the distributions were adjusted for better comparison of the shape.

the different data sets were scaled to a similar integral. All data agree well within the statistical errors. Closer inspections reveals an astonishingly good agreement of the complete reaction identification of the present thesis with the ANKE experiment. Therefore, in in figure 6.24 only these two results are shown. With only these results it looks like the structure of $\Lambda(1405)$ is more complex then the predicted blue line. Both results show two peaks, one at around 1380 MeV to 1395 MeV and one at around 1420 MeV to 1430 MeV. These two peaks are close to the two states predicted by Hyodo and Jido [62], where the $\Lambda(1405)$ is formed by a singlet at 1390 MeV and an octet state at 1426 MeV. However the predicted width of the states and the mass resolution of this analysis should make it impossible to have a visible separation of the two states. In figure 6.25 the mass resolution of the line shape reconstruction is shown. Two particle with no mass width were simulated to determine the mass resolution. Both identification methods show a mass resolution of around 13 MeV. With this mass resolution the predicted two peaks should overlap in energy and not be separable in the line shape. Either the predicted line widths is actually too wide or the two visible peaks are just statistical fluctuations. As the CLAS data does not show any strong evidence for two peaks the latter option is the more logical conclusion until more data is acquired and the statistical error reduced.
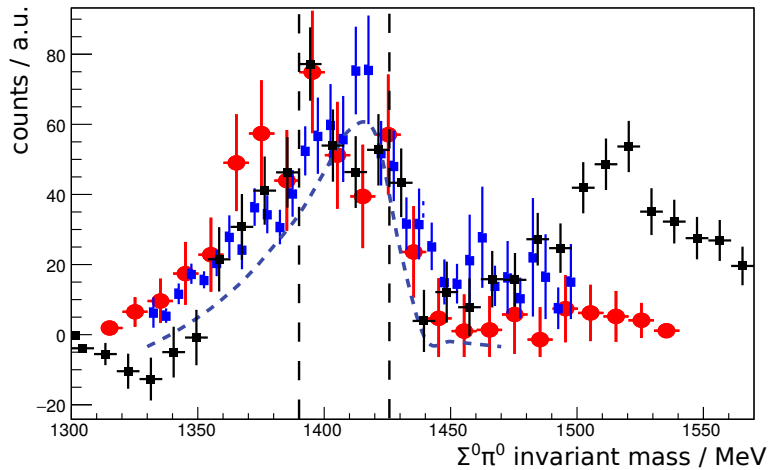
Figure 6.23: Line shape of the $\Lambda(1405)$ in the $\Sigma^0\pi^0$ decay. Black points mark in this thesis determined line shape with the complete detection of the final-state particles. The blue points are from the CLAS experiment of figure 6.8. The red points are the ANKE experiment results of figure 6.6. The blue dashed line marks the predicted line shape by Nacher at el.[64]. The height of the distributions were adjusted for better comparison of the shape.

6.3 Differential cross section

The yield of $\Lambda(1405)$ events is extracted from the data set for the differential cross section. The measured line shape in section 6.2 could be used in RooFit to describe the signal shape, however not performed during the cross section determination. Instead the simulation uses a Breit-Wigner distribution with 50 MeV width, modified by a cut off for masses higher than 1430 MeV. The resulting signal shape is similar to the line shapes measured by the CLAS collaboration in figure 6.8. First the cross section for the analysis with all kaon angles from section 6.1.1 is determined.

The extraction of the signal was done via a two-dimensional fit on the $\gamma\Lambda$ against $\pi^0\gamma\Lambda$ mass. The resulting contributions can be illustrated by projecting the two-dimensional plot into two one-
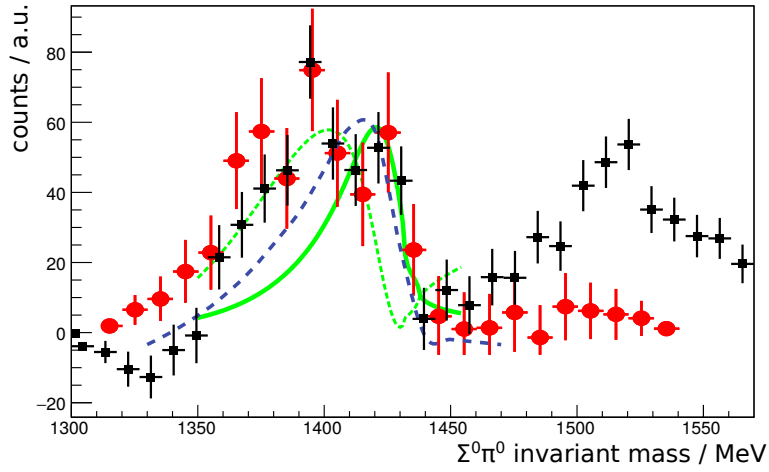
Figure 6.24: Line shape of the Λ(1405) in the $\Sigma^0\pi^0$ decay. Black points mark in this thesis determined line shape with the complete detection of the final-state particles. The red points are the ANKE experiment results of figure 6.6. The blue dashed line marks the predicted line shape by Nacher at el.[64]. The green dashed line shows the distribution for $\pi\Sigma \to \pi\Sigma$ and the solid line for the $N\bar{K} \to \pi\Sigma$ interaction of the predicted two states of Λ(1405) by Hyodo and Jido [62]. The height of the distributions were adjusted for better comparison of the shape.
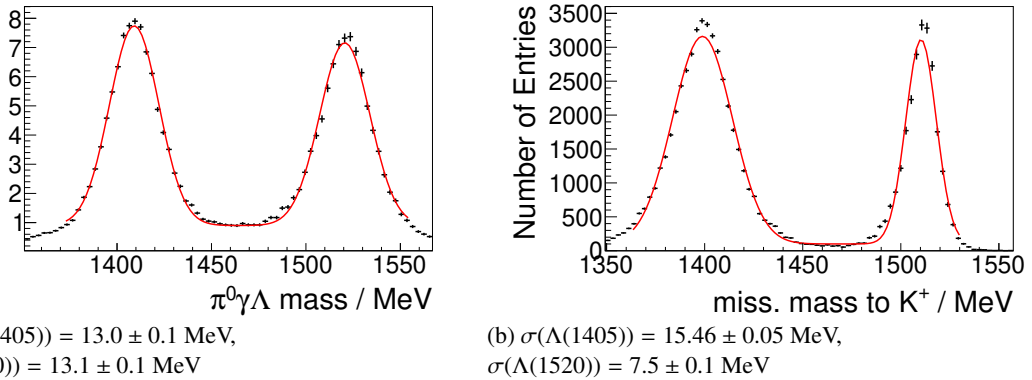
(a) $\sigma(\Lambda(1405)) = 13.0 \pm 0.1$ MeV, $\sigma(\Lambda(1520)) = 13.1 \pm 0.1$ MeV

(b) $\sigma(\Lambda(1405)) = 15.46 \pm 0.05$ MeV, $\sigma(\Lambda(1520)) = 7.5 \pm 0.1$ MeV

Figure 6.25: Mass resolution determination for the Λ(1405) line shape. A particle with the Λ(1405) and Λ(1520) mass was simulated, but with no natural line width. (a) shows the mass distribution for line shape extraction in section 6.2.1, while (b) shows section 6.2.2. The E_γ ranges from 1530 MeV to 1830 MeV.

dimensional plots. In figure 6.26 some example bins are shown, with the $\pi^0\gamma\Lambda$ projection on the left side and the $\gamma\Lambda$ on the right. The extracted $\Lambda(1405)$ signal was used to calculate a differential cross section, which can be seen in figure 6.27. The black points mark the extracted cross section, while the blue points show the results for the CLAS experiment. The magenta points are extracted from the analysis with the kaon in the forward spectrometer from section 6.1.2. The extraction is equivalent to the all angle kaon analysis. The two-dimensional plot for the fit used missing mass to $K^+\pi^0$ against missing mass to K^+ and an example fit result is seen in figures 6.15.

The cross section determined with the K^+ in the forward spectrometer can be seen as an extension of the previous CLAS data. This covers an acceptance not covered by the CLAS experiment. The result appears consistent with a smooth extrapolation of the CLAS data. The cross section for all kaon angles determined through the complete identification of the final-state shows a behavior different from the CLAS data. The results differ especially at the reaction production threshold where the CLAS data is a factor three higher.

As already mentioned in section 5.4, the measured benchmark cross sections still show anomalies due to the non perfect geometry description in the simulation. The improvement of the simulated geometry is mandatory before any statement on the discrepancy with CLAS can be made. However, the effect of the geometry observed in section 5 is significantly smaller than the deviations between this and the CLAS analysis. This hints that the discrepancy may be real and further careful studies are required to ensure this.

For a molecule type $\Lambda(1405)$ an important aspect is the momentum transfer dependence in the production process. This is studied in the following by plotting the production cross section as a function of momentum transfer t. Figure 6.9 shows the production of $\gamma p \rightarrow K^+\Lambda(1405)$ via the t-channel. The squared momentum transfer, t, is determined by:

$$t = (\gamma - K^+)^2 = (p - \Lambda(1405))^2, \tag{6.1}$$

here γ, K^+, p and $\Lambda(1405)$ denote the four momenta of the particles. The minimal momentum transfer, t_{min}, is the limit value for t at $\theta = 0$, and depends on E_γ. The momentum transfer difference, $|t - t_{min}|$, can be determined using $\cos(\theta_{CMS})$ and E_γ and the results are shown in figure 6.28. While the data points show an exponential distribution for high energies indicating a t-process production, the cross section drops for low t in the low energy range. This is most probably due the method of t determination. Here t was determined using $\cos(\theta_{CMS})$, E_γ and the assumptions that $\Lambda(1405)$ has no width and t is distributed homogeneous over the angle bin. This works for the most of the data set but apparently fails at the edges of the t acceptance.

In figure 6.29 the cross section is plotted against $-t$ for all BGO-OD results. The cross section drops with $-t > 0.23\,\text{GeV}^2$, corresponding to $\sqrt{|t|} = 480\,\text{MeV}$. One possible interpretation of this results is that if $\sqrt{|t|}$ is below the kaon mass, the kaon can only be produced in a bound system of nucleon-antikaon, increasing the $\gamma p \rightarrow K^+\Lambda(1405)$ cross section. Above the kaon mass the kaon can be produced free reducing the $\Lambda(1405)$ cross section. This interpretation only works with the assumption of a molecule structure of $\Lambda(1405)$. The CLAS result however shows a different picture as seen in figure 6.30 with no strong correlation. Future in-depth analysis will have to solve this discrepancy.

(a)

(b)

(c)

(d)

(e)

(f)

——	**real data**
——	**K$^+$ Λ(1405)**
——	**K$^+$ Λ(1520)**
——	**K$^+$ Σ(1385)**
——	**η π^0 p**
——	**K$^+$ Σ^0 π^0**
——	**K$^+$ Λ^0 π^0**
——	**K$^+$ Σ^+ π^-**
····	**simulation sum**

(g) Legend
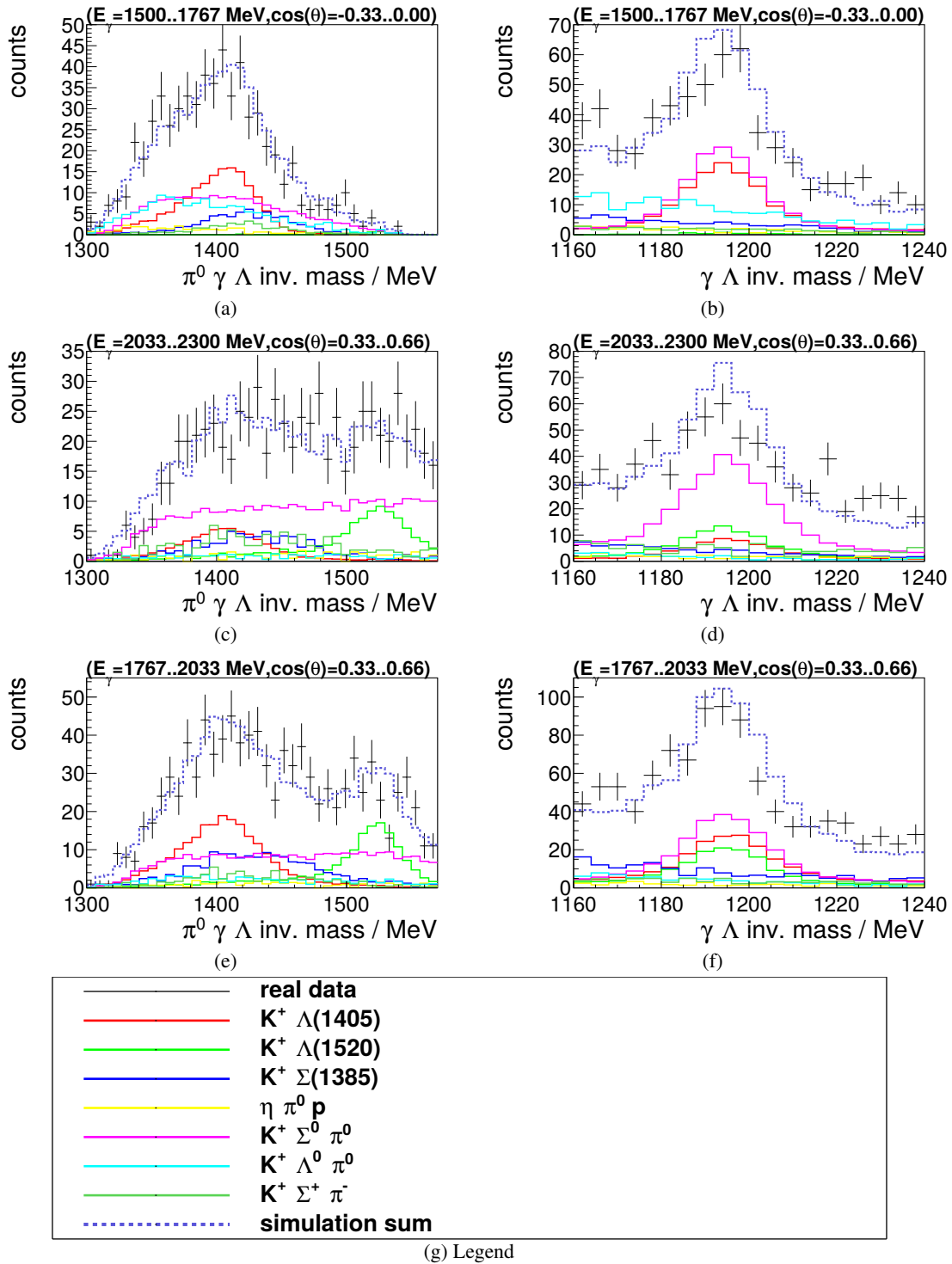
Figure 6.26: $\gamma p \rightarrow K^+ \pi^0 \Sigma^0$ reaction signal extraction for $\Lambda(1405)$. The plots show the projections of the two-dimensional data and fit results for different kaon angle, $\cos(\theta_{CMS})$, and beam energies, E_γ. The angle and energy of each bin can be found in the title of the plot. The different line colors are explained in the bottom legend.
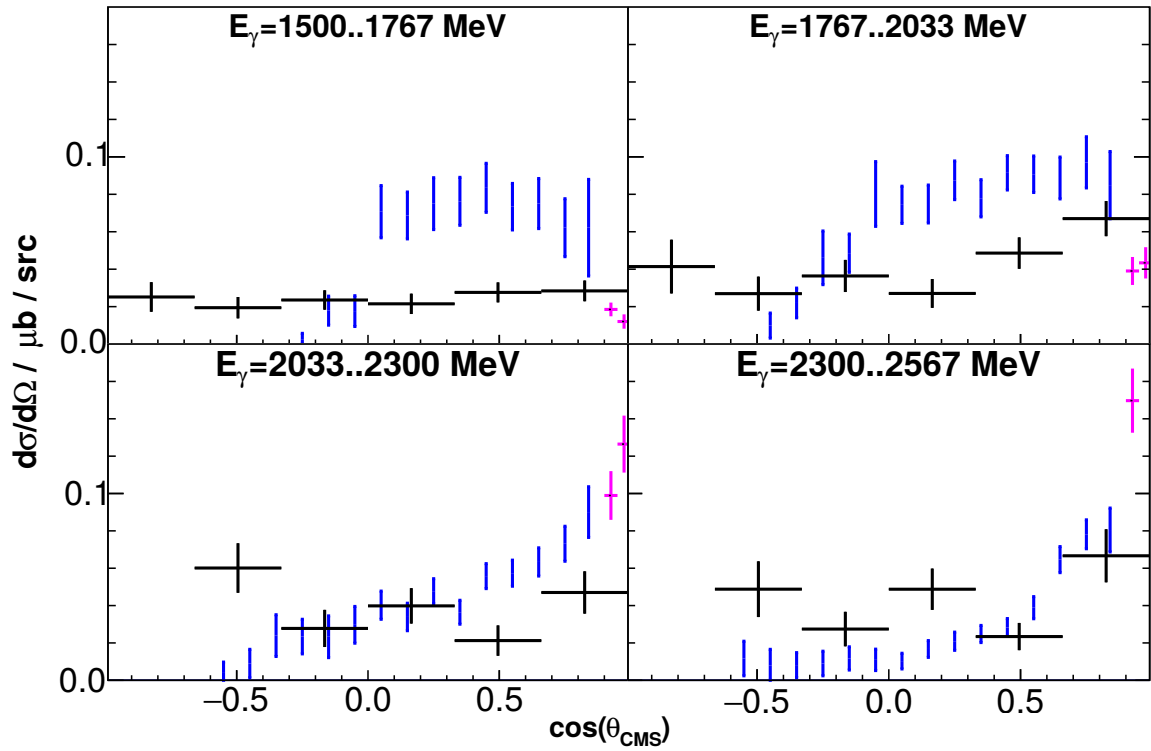
Figure 6.27: Differential cross section for $\gamma p \to K^+\Lambda(1405) \to K^+\pi^0\Sigma^0$ against $\cos(\theta)$ of the meson in the center of mass system. Black points mark the $K^+\Lambda(1405) \to K^+\pi^0\Sigma^0 \to K^+3\gamma\pi^- p$ decay where all particles are detected. Magenta points mark the cross section with only $K^+\pi^0$ detected from section 6.1.2. The blue data points are CLAS data [57] for $K^+\Lambda(1405) \to K^+\pi^0\Sigma^0$. Both cross sections were scaled up by factor 3 to take the branching ratio of the decay into account.

(a) E_γ =1500 MeV to 1767 MeV

(b) E_γ =1767 MeV to 2033 MeV

(c) E_γ =2033 MeV to 2300 MeV

(d) E_γ =2300 MeV to 2567 MeV
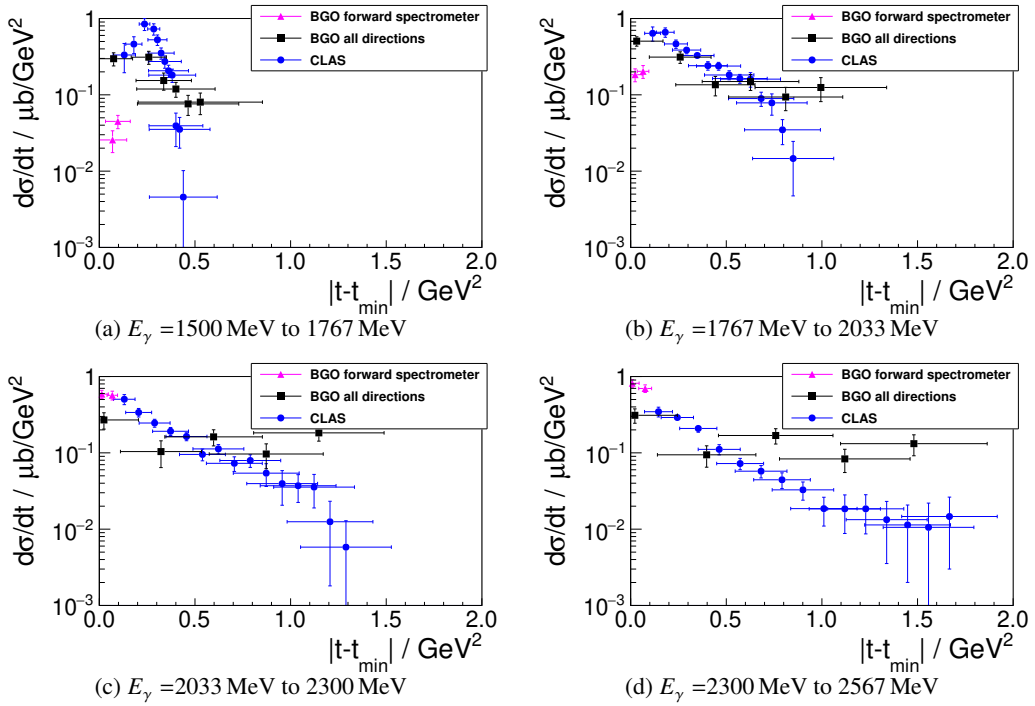
Figure 6.28: Differential cross section for $\gamma p \to K^+\Lambda(1405) \to K^+\pi^0\Sigma^0$ against squared transfer momentum t to the $\Lambda(1405)$. Black points mark the identification of the $K^+\Lambda(1405) \to K^+\pi^0\Sigma^0 \to K^+ 3\gamma\pi^- p$ decay where all particles are detected. Magenta points mark the cross section with only $K^+\pi^0$ detected from section 6.1.2. The blue data points were taken by the CLAS experiment [57] for $K^+\Lambda(1405) \to K^+\pi^0\Sigma^0$.
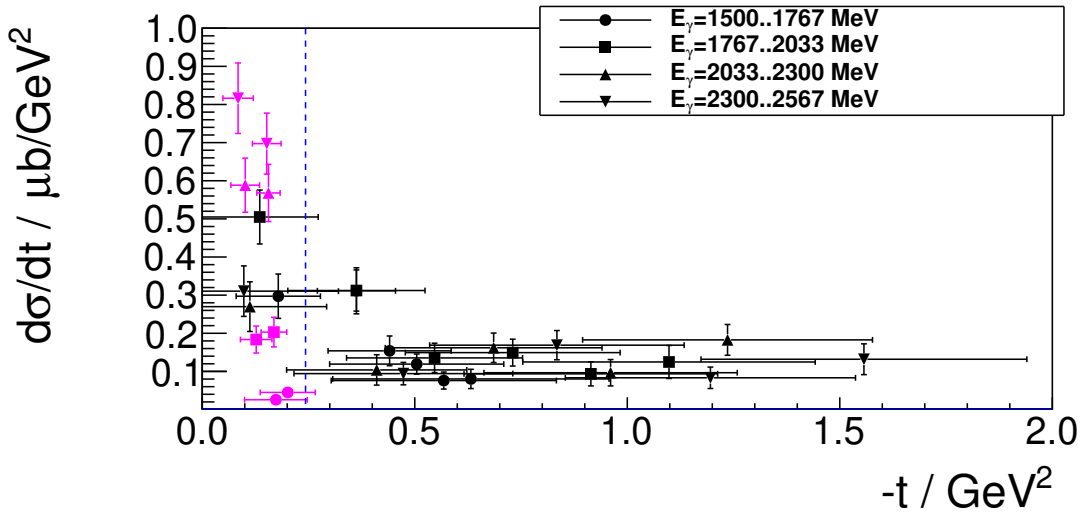
Figure 6.29: Differential cross section for $\gamma p \to K^+\Lambda(1405) \to K^+\pi^0\Sigma^0$ against transfer momentum $-t$ to the $\Lambda(1405)$. Black points mark the identification of the $K^+\Lambda(1405) \to K^+\pi^0\Sigma^0 \to K^+ 3\gamma\pi^- p$ decay where all particles are detected. Magenta points mark the cross section with only $K^+\pi^0$ detected from section 6.1.2. Both cross sections were scaled up by factor 3 to take the branching ratio of the decay into account. Squares,circles and triangles mark the different energy bins.
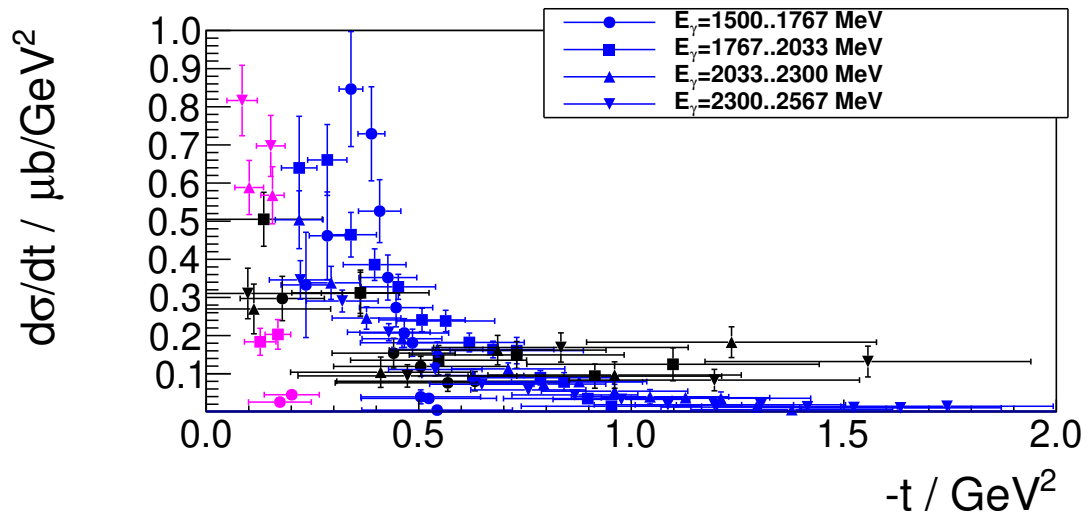
Figure 6.30: Differential cross section for $\gamma p \to K^+\Lambda(1405) \to K^+\pi^0\Sigma^0$ against transfer momentum $-t$ to the $\Lambda(1405)$. Description on the data is in figure 6.29. Additionally the blue data points were taken from the CLAS experiment [57].

Summary and Outlook

Most of the mass surrounding us originates from protons and neutrons, called nucleons. Nucleons consist of elementary particles known as quarks, which are bound by exchange bosons, called gluons. The valence quarks of the nucleon only make up a small fraction of the mass. The remaining mass is generated by the strong color field associated with gluon exchange, confining the quarks together in a color neutral state. Any attempt to separate the quarks leads to the creation of new color neutral hadrons composed of quarks. All composite quantum mechanical particles have excitation levels, for example the hydrogen atom. In the atom the higher excitations levels can be interpreted as an increase in distance between electrons and nucleus, corresponding to a change in potential energy. A similar concept was also applies to color interactions with an inter-quark confinement potential. Even between color neutral hadrons, a residual of the strong color force may still cause binding, similar to the electromagnetic van der Waals interaction which binds uncharged atoms to form molecules. It is the residual color force which binds the nucleons together to a nucleus through a baryon-baryon interaction. Theoretically, it could also bind meson-meson or meson-baryon states. A candidate for such a meson-baryon state is the $\Lambda(1405)$ hadron investigated in this thesis. This is poorly described by the three valence quark model and is speculated to be a meson-baryon or pentaquark state. The $\Lambda(1405)$, $J^P = 1/2^-$, with (uds) valence quarks is lighter than its counter partner $N(1535)$, $J^P = 1/2^-$, consisting of up and down quarks, even thought it has the heavier valence quarks. Furthermore, the invariant mass distribution of the $\Lambda(1405)$, called the line shape, is distorted [51]. These inconsistencies support descriptions that the $\Lambda(1405)$ has a more complex structure. A possible pentaquark or a meson-baryon molecule configuration is supported by recent Lattice QCD results [58].

Meson photoproduction is a well established tool to investigate baryon excitations. The $\Lambda(1405)$ is formed in associated strangeness production via the reaction $\gamma p \rightarrow K^+\Lambda(1405)$. If the $\Lambda(1405)$ indeed has the structure of a relatively loosely bound meson-baryon molecule, the ability to incorporate momentum in the production process will be rather limited. Consequently, the K^+ will be produced in forward directions. The BGO-OD experiment at the ELSA accelerator in Bonn is ideal to investigate extreme K^+ forward angles. Using an energy tagged photon beam, it combines a central calorimeter and a forward spectrometer.

This thesis presented differential cross sections for $\gamma p \rightarrow K^+\Lambda(1405)$ and $\Lambda(1405)$ line shape measurements. These measurements require an understanding of the detector geometry and response and an absolute flux normalization, both of which were improved as part of the thesis work.

The determination of the detection probability for a reaction requires an accurate representation of the experimental setup in the Monte Carlo simulation of the experiment. In this thesis the simulation of the

data acquisition triggering system was shown. Consistency checks measuring the $\gamma p \to \pi^0 p$ reaction showed only small deviations in the cross section compared to other experiments, demonstrating that the current hardware trigger system is well understood.

For most reactions of interest, the signal to background ratio can be determined via fitting of expected signal and background mass distributions. The mass resolution can be improved using a kinematic fit, which was implemented in the analysis framework, ExPlORA , of the BGO-OD experiment during the course of this thesis. To check the current performance of the cross section determination using the implemented kinematic fitting, the reactions γp to $\pi^0 p$, ηp, ωp, $\eta' p$ and $K^+ \Sigma^0$ were identified. The results agree well with previous experiments. Some small deviations at specific particle angles or momenta show that there is still slight corrections required in the simulated geometry. This will be addressed beyond the frame of this thesis.

The main goal of the thesis was the investigation of the $\gamma p \to K^+ \Lambda(1405)$ reaction. First results were achieved with the BGO-OD experiment, and the line shape and differential cross section using the $\Sigma^0 \pi^0$ decay was measured. The unique combination of a forward spectrometer and central calorimeter allows access to more forward angles and low momentum exchange regions not accessible in other experiments. The statistical accuracy obtained is at least on par with the previously most accurate CLAS experiment. Within statistics the observed line shape agrees well with the earlier experiments. The analysis of this thesis seems to indicate a double peak structure in the $\Lambda(1405)$ line shape. This would be in agreement with an other recent result at ANKE, but in contrast to the single peak measured by CLAS. It is important to increase statistical accuracy in the future to resolve this issue. Further investigations of the experiment setup in the simulation will eliminate the small deviations in the benchmark cross sections and extend the current $\Lambda(1405)$ cross section measured by CLAS to more forward angles. Due to the production mechanism of the $\Lambda(1405)$, it is important to measure the cross section dependence on the transfer momentum. First studies on this dependency were made in this thesis and will continue in the future.

Acknowledgements

Bibliography

[1]   *University of Zurich*, Physik Institut, URL: https:
      //www.physik.uzh.ch/en/researcharea/lhcb/outreach/StandardModel.html
      (cit. on p. 2).

[2]   M. Gell-Mann, *Symmetries of Baryons and Mesons*,
      doi: https://doi.org/10.1103/PhysRev.125.1067,
      Physical Review, volume 125, number 3, 1962, 1962 (cit. on p. 2).

[3]   M. Tanabashi et al., *The Review of Particle Physics*, Phys. Rev. D 98, 030001,
      Particle Data Group, 2018 (cit. on pp. 3, 4, 20, 36, 58, 79, 85).

[4]   A. Thiel et al.,
      Double-polarization observable G in neutral-pion photoproduction off the proton,
      CBELSA/TAPS Eur.Phys.J. A53 (2017), 2017 (cit. on p. 5).

[5]   S.-K. Choi et al.,
      Observation of a narrow charmonium-like state in exclusive $B^+ \rightarrow K^+\pi^+\pi^- J/\psi$ decays,
      Belle collaboration, doi: 10.1103/PhysRevLett.91.262001, Phys.Rev.Lett.91:262001, 2003
      (cit. on p. 6).

[6]   R. Aaij et al.,
      Observation of $J\psi p$ resonances consistent with pentaquark states in $\Lambda_b^0 \rightarrow J\psi K^- p$ decays,
      LHCb collaboration, doi: 10.1103/PhysRevLett.115.072001,
      Phys. Rev. Lett. 115, 072001, 2015 (cit. on p. 6).

[7]   Jonathan M. M. Hall et al.,
      Lattice QCD Evidence that the Λ(1405) Resonance is an Antikaon-Nucleon Molecule,
      arXiv:1411.3402v2 [hep-lat], Phys. Rev. Lett. 114, 132002 (2015), 2015 (cit. on pp. 6, 81, 84).

[8]   *Electron Stretcher Accelerator (ELSA) Homepage*,
      URL: http://www-elsa.physik.uni-bonn.de/index_en.html (cit. on pp. 7, 8).

[9]   *Crystal Barrel Experiment Homepage*, URL: www.cb.uni-bonn.de (cit. on p. 7).

[10] W. Hillert, *The Bonn Electron Stretcher Accelerator ELSA: Past and future*,
      doi: 10.1007/3-540-36754-3_15,
      European Physical Journal A - EUR PHYS J A, vol. 28, page 139-148, 2006 (cit. on p. 7).

[11] J. Hannappel, *Private communication*, BGO-OD Experiment (cit. on p. 8).

[12] A. Bella, *Linearly polarised photon beams at the BGO-ODexperiment at ELSA*, PhD thesis,
      2016 (cit. on pp. 9, 10).

[13] F. Messi, *The tagging system of the BGO-OD experiment*, doctoral thesis, Juli 2015
      (cit. on p. 10).

[14] B.-E. Reitz, *Construction of an additional hodoscope for the BGO-OD experiment consisting of scintillator fibres (ARGUS) together with simple π^0 analysis*, Master thesis, 2015 (cit. on p. 10).

[15] S. Alef, *Development of a scintillating fibre hodoscope (ARGUS) for the tagging system of the BGO-OD experiment*, Master thesis, 2015 (cit. on p. 10).

[16] H. Olsen and L. Maximon, *Photon and Electron Polarisation in High-Energy Bremsstrahlung and Pair Production with Screening*, Physical Review 114 887-904, 1959 (cit. on p. 11).

[17] T. Zimmermann, *Møller polarimetry for the BGO-OD experiment and cross section measurement of the reaction $\gamma p \rightarrow K^+\Lambda$ at the extreme forward angles*, PhD thesis, BGO-OD Experiment, 2017 (cit. on p. 11).

[18] B. Leibrock, *Erstinbetriebnahme der Vieldrahtproportionalkammer des BGO-OD-Experiments*, Bachelor thesis, September 2014 (cit. on p. 12).

[19] P. Bauer, *Track and vertex reconstruction in the BGO-OD experiment using the central MWPC*, Master thesis, BGO experiment, 2017 (cit. on p. 12).

[20] D. Spuelbeck, *Bachelor thesis*, 2018 (cit. on p. 12).

[21] F.Ghioa and B.Girolamia et al., *The GRAAL high resolution BGO calorimeter and its energy calibration and monitoring system*, doi: 10.1016/S0168-9002(97)01124-8, Nuclear Instruments and Methods in Physics Research A, Volume 404, Issue 1, Pages 71-86, February 1998 (cit. on p. 12).

[22] G. Scheluchin, *Meson photoproduction on the proton using the BGO-OD detector complemented by a new Scintillating Ring (SciRi)*, Master Thesis, University of Bonn, 2015 (cit. on pp. 14, 26, 58).

[23] M. Becker, *Charakterisierung eines MRPC-Prototypdetektors für das BGO-OD Experiment*, Bachelor thesis, September 2014 (cit. on p. 14).

[24] S. Böse, *Aufbau und Test eines neuen Szintillationsfaser-Detektors für das neue Vorwärtsspektrometer an ELSA*, doctoral thesis, 2015 (cit. on p. 14).

[25] T. Frese, *Insitu field measurement of the Open Dipole magnet at the BGO-OD experiment*, Master thesis, December 2012 (cit. on p. 14).

[26] T. Schwan, *Test und Inbetriebnahme der Driftkammern für das BGO-OD-Spektrometer*, Diplomarbeit, April 2010 (cit. on pp. 14, 15).

[27] P. Meiß, *The Time Of Flight Spectrometer of the BGO-OD Experiment*, Diplomarbeit, September 2013 (cit. on pp. 14, 15).

[28] T. Zimmermann, *Photon Flux Monitor for the BGO-OD experiment*, Diplomarbeit, BGO-OD Experiment, 2012 (cit. on p. 15).

[29] K. Kohl, *Absolute Photon Flux Measurement at the BGO-OD-Experiment*, Master thesis, September 2016 (cit. on pp. 15, 43).

[30] O. Freyermuth, *Studies of ω Photoproduction off Proton at the BGO-OD Experiment*, PhD thesis, 2017 (cit. on pp. 16, 33).

[31] S. Agostinelli et al., *Geant4—a simulation toolkit*, Nuclear Instruments and Methods in Physics Research A, Volume 506, Issue 3, 1 July 2003 (cit. on pp. 16, 47).

[32] K. Kohl, *ongoing PhD thesis*, PhD thesis, 2020 (cit. on p. 21).

[33] *RooFit Homepage*, URL: https://root.cern.ch/roofit-0 (cit. on pp. 25, 34, 59).

[34] *Applied Fitting Theory VI,Formulas for Kinematic Fitting*, Paul Avery,CBX 98–37, 1998, URL: http://www.phys.ufl.edu/~avery/fitting/kinematic.pdf (cit. on pp. 26, 28).

[35] *Applied Fitting Theory I,General Least Squares Theory*, Paul Avery,CBX 91-72, 1991, URL: http://www.phys.ufl.edu/~avery/fitting/fitting1.pdf (cit. on p. 27).

[36] J. D. Bjorken and S. D. Drell, *Relativistic Quantum Mechanics*, 1964 (cit. on p. 35).

[37] W. R. Leo, *Techniques for nuclear and particle physics experiments: a how-to approach*, Springer, 1994 (cit. on pp. 35, 44).

[38] U.S. Department of Commerce, *National Insitute of Standards and Technology*, URL: https://www.nist.gov (cit. on p. 36).

[39] D. Hammann, *The data acquisition for the BGO-OD experiment*, PhD thesis, 2016 (cit. on p. 54).

[40] *Bonn-Gatchina Partial Wave Analysis*, https://pwa.hiskp.uni-bonn.de/, 2018 (cit. on pp. 69, 70, 72, 76).

[41] E.F. McNicoll et al., *Study of the $\gamma p- > \eta p$ reaction with the Crystal Ball detector at the Mainz Microtron(MAMI-C)*, Crystal Ball Collaboration at MAMI, doi: 10.1103/PhysRevC.82.035208, 2010 (cit. on p. 72).

[42] V. Crede et al., *Photoproduction of eta and eta-prime mesons off protons*, The CBELSA/TAPS Collaboration, doi: 10.1103/PhysRevC.80.055202, 2009 (cit. on pp. 72, 75).

[43] M. Dugger et al., *Eta photoproduction on the proton for photon energies from 0.75-GeV to 1.95-GeV*, CLAS Collaboration, doi: 10.1103/PhysRevLett.89.222002, 2002 (cit. on p. 72).

[44] F. Dietz, V. Metag and et al., *Photoproduction of ω mesons off protons and neutrons*, The CBELSA/TAPS Collaboration, doi: 10.1140/epja/i2015-15006-3, 2015 (cit. on p. 73).

[45] M. Williams et al., *Differential cross sections and spin density matrix elements for the reaction $\gamma p \to p\omega$*, CLAS Collaboration, doi: 10.1103/PhysRevC.80.065208, 2009 (cit. on p. 73).

[46] M. Dugger et al., *Eta-prime photoproduction on the proton for photon energies from 1.527-GeV to 2.227-GeV*, CLAS Collaboration, doi: 10.1103/PhysRevLett.96.062001, 2006 (cit. on p. 75).

[47] B. Dey et al., *Differential cross sections and recoil polarizations for the reaction $\gamma p- > K^+\Sigma^0$*, CLAS Collaboration, doi: 10.1103/PhysRevC.82.025202, 2010 (cit. on p. 76).

[48] H. Kohri et al., *Differential cross section and photon beam asymmetry for the polarized-$\gamma n \to K^+\Sigma^-$ reaction at E_γ = 1.5GeV-2.4GeV*, LEPS Collaboration, doi: 10.1103/PhysRevLett.97.082003, 2006 (cit. on p. 76).

[49] K.-H. Glander et al., *Measurement of $\gamma p \to K^+\Lambda$ and $\gamma p \to K^+\Sigma^0$ at photon energies up to 2.6-GeV*, SAPHIR experiment at ELSA, doi: 10.1140/epja/i2003-10119-x, 2004 (cit. on p. 76).

[50] U. Loering, B. Metsch and H. R. Petry, *The light baryon spectrum in a relativistic quark model with instanton-induced quark forces. The strange baryon spectrum.* doi: 10.1007/s100500170106, Eur.Phys.J. A10 (2001) 447-486, 2001 (cit. on pp. 79, 80).

[51] R. J. Hemingway, *Production of Λ(1405) in K⁻p reaction at 4.2 GeV/c*, North-Holland Publishing Company, Nucl. Phys. B 253, 742 (1985), 1985 (cit. on pp. 81, 101).

[52] J. C. Nacher et al., *Photoproduction of the Lambda(1405) on the proton and nuclei*, doi: 10.1016/S0370-2693(99)00380-9, Phys. Lett. B 455, 55 (1999), 1999 (cit. on pp. 82, 83).

[53] I. Zychor, *Studies of the Λ(1405) in Proton-Proton Collisions with ANKE at COSY-Jülich*, ECONFC070910:310,2007, MENU 2007, IKP, Forschungzentrum Jülich, Germany, 2007 (cit. on p. 82).

[54] M. Niiyama, H. Fujimura and et al., *Photoproduction of Λ(1405) and Σ⁰(1385) on the proton at E_γ = 1.5-2.4 GeV*, doi: 10.1103/PhysRevC.78.035202, 2008 (cit. on pp. 83, 84).

[55] K. Moriya, R. A. Schumacher and et al., *Measurement of the Σπ photoproduction line shapes near the Λ(1405)*, Physical Review C 87, 035206, 2013 (cit. on p. 83).

[56] K. Moriya and R. Schumacher, *Properties of the Λ(1405) Measured at CLAS*, arXiv:0911.2705v1 [nucl-ex], Nucl.Phys.A835:325-328,2010, 2009 (cit. on p. 83).

[57] K. Moriya et al., *Differential Photoproduction Cross Sections of the Σ⁰(1385), Λ(1405), and Λ(1520)*, arXiv:1305.677v2 [nucl-ex], Phys. Rev. C 88, 045201, 2013 (cit. on pp. 83, 97–99).

[58] Y. Nogami, *Possible existence of overlineKNN bound states*, doi: 10.1016/0031-9163(63)90336-6, Phys. Lett. 7 (1963) 288–289, 1963 (cit. on pp. 80, 101).

[59] R. H. Dalitz and S. F. Tuan T, *The Energy Dependence of Low Energy K⁻-Proton Processes**, Annals of Physics: 8, loo-118 (1959), 1959 (cit. on p. 84).

[60] E. Oset, J. A. Oller and U.-G. Meißner, *Chiral dynamics and the reactions pp → dK⁺K̄⁰ and pp → dπ⁺η*, arXiv:nucl-th/0109050, Eur.Phys.J. A12 (2001) 435-446, 2001 (cit. on p. 84).

[61] M. Mai and U.-G. Meißner, *Constraints on the chiral unitary K̄N amplitude from πΣK⁺ photoproduction data*, doi: 10.1140/epja/i2015-15030-3, arXiv:1411.7884 [hep-ph], 2015 (cit. on p. 84).

[62] T. Hyodo and D. Jido, *The nature of the Λ(1405) resonance in chiral dynamics*, doi: 10.1016/j.ppnp.2011.07.002, Prog.Part.Nucl.Phys.67::55-98, 2011 (cit. on pp. 84, 93, 94).

[63] I. Zychor and et al., *Lineshape of the Λ(1405) Hyperon Measured Through its Σ⁰π⁰ Decay*, doi:10.1016/j.physletb.2008.01.002, Phys.Lett.B660:167-171, 2008 (cit. on p. 84).

[64] D. W. Thomas et al., *Strange Particle Production from π⁻p interactions at 1.69 GeV/c*, North-Holland Publishing Company, Nucl. Phys. B 56, 15 (1973), 1973 (cit. on pp. 93, 94).

List of Figures

List of Tables